UC San Diego

UC San Diego Electronic Theses and Dissertations

Title

Computational and Physical Quality Assurance Tools for Radiotherapy

Permalink

https://escholarship.org/uc/item/65n785ck

Author

Graves, Yan Jiang

Publication Date

2013

Peer reviewed|Thesis/dissertation

eScholarship.org Powered by the California Digital Library
University of California

UNIVERSITY OF CALIFORNIA, SAN DIEGO

Computational and Physical Quality Assurance Tools for Radiotherapy

A dissertation submitted in partial satisfaction of the requirements for the
degree of Doctor of Philosophy

in

Physics (Biophysics)

by

Yan Jiang Graves

Committee in charge:

Professor Ken Intriligator, Chair
Professor Steve B. Jiang, Co-Chair
Professor Laura Cerviño
Professor Juan C. del Álamo
Professor Hans P. Paar
Professor Clifford M. Surko

2013

©2013

Yan Jiang Graves

All rights reserved.

The Dissertation of Yan Jiang Graves is approved, and it is acceptable in quality and form for publication on microfilm and electronically:

Co-Chair

Chair

University of California, San Diego

2013

To

my parents

TABLE OF CONTENTS

Signature Page....iii

Dedication....iv

Table of Contents....v

List of Figures....ix

List of Tables....xiii

List of Abbreviations....xiv

Acknowledgements....xvii

Vita....xix

Abstract....xxi

1. Introduction....1

    1.1. Overview of Radiation Therapy....1

        1.1.1. Radiobiology....2

        1.1. 2. Typical Treatment Forms....3

    1.2. Linear Accelerator....5

    1.3. Radiation Treatment Process....8

        1.3.1. Treatment Simulation....10

        1.3.2. Treatment Planning....10

        1.3.3. Treatment Delivery....12

    1.4. Adaptive Radiotherapy....13

    1.5. Quality Assurance....16

1.5.1. Plan Quality Assurance..16

1.5.2. Adaptive Radiotherapy Quality Assurance..................................19

2. Computational Quality Assurance Tool...22

2.1. Overview...22

2.2. Monte Carlo Simulation for Dose Calculation.....................................24

2.2.1. Basics of Monte Carlo Method for Dose Calculation.....................24

2.2.2. GPU Based Monte Carlo Code..26

2.3. Monte Carlo Dose Uncertainty on Gamma-index Evaluation...............29

2.3.1. Overview of Gamma-index Evaluation...29

2.3.1.1. GPU Based Gamma-index Evaluation...................................31

2.3.2. Motivation...32

2.3.3. Theoretical Molding..34

2.3.3.1. MC Statistical Fluctuations in Reference Dose.......................34

2.3.3.2. MC Statistical Fluctuations in Evaluation Dose.......................37

2.3.4. Numerical Experiments...41

2.3.5. Experiment Results...44

2.3.5.1. MC Reference Dose vs Non-MC Evaluation Doses................44

2.3.5.2. Non-MC Reference Dose vs MC Evaluation Doses................47

2.3.5.3. MC Reference Dose vs MC Evaluation Dose.........................50

2.3.6. Discussion and Conclusion..52

2.4. Denoising for Monte Carlo Based Dose..55

2.4.1. Overview of Monte Carlo Based Dose Denoising.........................55

2.4.2. Denoising Algorithm..56
2.4.3. Numerical Experiments...60
2.4.4. Experiment Results..61
2.5. Monte Carlo Source Modeling..65
2.5.1. Dosimetric Properties of Photon Beams...65
2.5.2. Overview of Monte Carlo Source Modeling....................................69
2.5.3. Our Source Model and Commissioning Method.............................71
2.5.4. Implementation Details..72
2.5.5. Commissioning Results...78
2.5.6. Patient Case Validation..84
2.6. Fluence Map Generation..86
2.6.1. MLC Transmission Property...87
2.6.2. Fluence Map From DICOM Files..91
2.6.3. Fluence Map From Log Files...94
2.7. Web Application for Quality Assurance Tool..96
2.7.1. Quality Assurance Tool Workflow...96
2.7.2. Web Application...97
2.7.3. Patient Quality Assurance Results...100
2.8. Summary...103
3. Physical Quality Assurance Phantom..107
3.1. Overview...107
3.2. Design and Fabrication...108

3.2.1. Phantom Design..108

3.2.2. Material Selection and Fabrication...112

3.3. Phantom Properties 114

3.4. Radiation Diode...116

3.4.1. Angle Dependence Property..116

3.4.2. Dosimetry Calibration...120

3.5. Deformable Image Registration Algorithm Accuracy Test.................121

3.5.1. Overview of Demons Algorithm 123

3.5.2. Algorithm Performance...123

3.6. Adaptive Radiotherapy Dosimetry Verification..................................127

3.6.1. Experiment Results...128

3.7. Discussion and Conclusions...131

4. Conclusions...134

Reference..137

Appendex..151

LIST OF FIGURES

Figure 1.1: The therapeutic ratio from the tumor control probability and the normal tissue complication probability curves..3

Figure 1.2: Examples of a prostate plan with different technologies. (A) 3D conformal radiation therapy. (B) IMRT with 5 fields. (Adopted from Zelefsky *et al.* (2000))..5

Figure 1.3: A Varian version of a linear accelerator with cone beam computed tomography mounted. (Image courtesy of Varian Medical System Inc.).......7

Figure 1.4: Schematic representation of LINAC head components. (Adopted from Verhaegen and Seuntjens (2003))..7

Figure 1.5: Multileaf collimator. (Image courtesy of Varian Medical System Inc.)..8

Figure 1.6: Radiation therapy process..9

Figure 1.7: A typical DHV plot..12

Figure 1.8: An example of a head and neck cancer patient experiencing tumor shrinkage. (A) CT scan before treatment. (B) Re-CT scan in the fourth week of the treatment course. Blue contours indicate the tumor area.................14

Figure 1.9: Examples of commercially available 3D dosimetric phantoms. *(*Image courtesy of ScandiDos AB and Sun Nuclear)................................19

Figure 1.10: UC San Francisco deformable phantoms. (A) A HN phantom. (B) A pelvic phantom..21

Figure 2.1: A typical hardware structure of a GPU card. *(*Image courtesy of NVIDIA)..28

Figure 2.2: (A) Graphical interpretation of the γ-index in 1D. (B) An example demonstrating how the γ-index value changes due to MC statistical fluctuations in the evaluation dose. (C) An example demonstrating how the γ-index value changes due to MC statistical fluctuations in the reference dose..34

Figure 2.3: (A) and (B) Illustrations of two different contexts where noise is present in the reference dose..37

Figure 2.4: (A) and (B) Illustrations of two different contexts where noise is present in the evaluation dose. (C) Split of the integration domain for Equation 2.11..41

Figure 2.5: Average γ-index and gamma passing rate as functions of σ level in the reference dose for MC reference doses vs non-MC evaluation dose. (A) and (C) Prostate case. (B) and (D) HN case...46

Figure 2.6: Average γ-index and gamma passing rate as functions of σ level in the evaluation dose for non-MC reference dose vs MC evaluation doses. (A) and (C) Prostate case. (B) and (D) HN case...49

Figure 2.7: Average γ-index as functions of σ level in evaluation dose for non-MC reference dose vs MC evaluation doses. (A) Prostate case. (B) HN case..49

Figure 2.8: The color maps of gamma passing rate within $\text{VOI}_{50\%}$ as functions of σ level in the reference and evaluation doses for MC reference dose vs MC evaluation dose with 3% -3mm criterion. (A) Prostate case. (B) HN case..51

Figure 2.9: Flow chart of our GPU based denoising algorithm. Grey boxes denote CUDA kernels and white boxes denotes C code on CPU..............59

Figure 2.10: Iso-dose lines for prostate (A-C) and HN (D-F) cases in central transversal slice. (A) and (D) Ground truth dose distributions. (B) and (E) Smoothed dose distributions and (C) and (F) Dose distributions with 2% σ level..63

Figure 2.11: Dose profiles. (A) HN case and (B) Prostate case......................64

Figure 2.12: A typical PDD curve for a 6MV photon beam..............................68

Figure 2.13: Dose deposition profiles at difference depths for a typical 6MV photon beam..68

Figure 2.14: Beam output factor curve for a typical 6MV photon beam...........69

Figure 2.15: Workflow of commissioning procedure to obtain energy spectrum and beam fluence...74

Figure 2.16: MATLAB GUI for our source commissioning..............................79

Figure 2.17: Reference field size PDD curves for different energy bins.........80

Figure 2.18: Commissioned energy spectrum for a 6MV beam......................80

Figure 2.19: (A) Commissioned PDD vs measured PDD. (B) Difference plot...81

Figure 2.20: (A) 2D commissioned beam fluence. (B) Line profile along the center..82

Figure 2.21: (A) Dose profiles at 5cm,10cm and 20cm depths. (B) Difference of profiles at 10cm depth...83

Figure 2.22: The source model output factor before correction is compared with the measured beam output factor data..84

Figure 2.23: Diagram showing the relation between the light field edge and leaf-tip projection. C is the machine isocenter. The points A,B,C,D and E at the SAD distance are the projection of the points a,b,c,d and e at the leaf end distance, respectively. (Adopted from Boyer and Li (1997)).................88

Figure 2.24: Diagram of X-ray passing through MLC rounded end leaf (adopted from Boyer and Li (1997))..90

Figure 2.25: An example of radiation transmission ratio with the distance to light field edge when light field edge is at the middle of beam field (adopted from Boyer and Li (1997))..91

Figure 2.26: Fluence map examples. (A) and (B) Considering MLC rounded end leaf transmission. (C) and (D) Without considering MLC rounded end leaf transmission. (E) and (F) The fluence intensity differences. The two columns are for two beams in a IMRT plan..93

Figure 2.27: Fluence map examples. (A) and (B) from Dicom. (C) and (D) from Trajectory Log File. (E) and (F) The fluence intensity differences. The two columns are for two beams in an IMRT plan...95

Figure 2.28: Workflow for the computational QA tool......................................98

Figure 2.29: Screen captures of the web application of the QA computational tool. (A) Data uploading. (B) Parameter setting. (C) Result Review............99

Figure 2.30: Dose distributions for a IMRT prostate case (A) Secondary dose (SD) (B) Delivered dose (DD) (C) Plan dose (PD). γ-index map for (D) SD vs. PD (E) SD vs. DD (F) DD vs. PD..101

Figure 2.31: Dose distributions for a VMAT HN case (A) Secondary dose (SD) (B) Delivered dose (DD) (C) Plan dose (PD). γ-index map for (D) SD vs. PD (E) SD vs. DD (F) DD vs. PD..102

Figure 3.1: (A) CT image of a representative HN patient with PTV and parotids contours. (B) Construction diagram with marked diode holder locations and rails. The dimensions are in cm. (C) CT slice at the middle of the constructed phantom...111

Figure 3.2: Design diagram of the diode holders on rail...............................112

Figure 3.3: CT scanning for different dense tissue material samples............114

Figure 3.4: Prototype of the deformable HN phantom.................................115

Figure 3.5: SRS diode. Dimensions are in mm..116

Figure 3.6: (A) Diagram of the buildup cap. Measurements are in mm. (B) Orientation of beam angles with respect to the diode...............................118

Figure 3.7: Isocentric setup to obtain the diode symmetry property.............118

Figure 3.8: Graph of diode response at different angles against response at zero degree gantry angle...119

Figure 3.9: Example of the optical image of the markers in dark...................122

Figure 3.10: Images of demons algorithm. (A) Reference image. (B) Moving image. (C) Deformed image. (D) Difference image between the reference and moving images. (E) Difference image between the reference and deformed images. (F) Generated deformation vector filed overlaid on the reference image...125

Figure 3.11: (A) Initial marker positions. (B) Final marker positions. (C) Initial and final marker position with the measured deformations overlaid on the reference CT image. (D) Generated deformation vector filed overlaid on the reference CT image...126

Figure 3.12: PTV and organ contours. (A) On the large tumor geometry and (B) On the small tumor geometry...128

Figure 3.13: DVH plots of initial optimal plan on new small tumor geometry (solid lines) and re-plan on new tumor geometry (dash lines)..................131

LIST OF TABLES

Table 2.1: Percentages of Type-I and Type-II voxels within $VOI_{50\%}$ and $VOI_{10\%}$ for MC reference doses of 2% σ level vs the non-MC evaluation dose with 3%-3mm and 2%-2mm criteria..46

Table 2.2: Percentages of Type-I and Type-II voxels within $VOI_{50\%}$ and $VOI_{10\%}$ for the non-MC reference dose vs MC evaluation doses of 2% σ level with 3%-3mm and 2%-2mm criteria..48

Table 2.3: Percentages of Type-I and Type-II voxels within VOI50% for the MC reference dose of 2% σ level vs the MC evaluation dose of 2% σ level with 3%-3mm criterion..51

Table 2.4: Maximum dose difference and RMSD for smoothed dose distributions and doses with 2% σ level compared with ground truth dose distributions...62

Table 2.5: Computational time for simulating ground truth and dose with 2% σ level using gDPM and denoising...62

Table 2.6: γ-index test results for MC dose distributions using the proposed source model and using PSL model..86

Table 2.7: γ-index result for three pairs of dose comparisons......................103

Table 2.8: Computation time in seconds for MC simulations and γ-index comparison..103

Table 3.1: Average HUs for phantom and patients' anatomic components...106

Table 3.2: Mean and standard deviation of the average error for DIR calculated deformation vectors compared with the measured deformation vectors...126

Table 3.3: Plan calculations and diode measurements (and the absolute difference) in percentage of the prescription dose before and after deformation with the original plan and the re-plan irradiated....................130

Table 3.4: The plan calculation and diode measurements (and the absolute difference) in percentage of prescription dose for accumulative dose from delivery I and delivery III..130

LIST OF ABBREVIATIONS

1D	One-dimensional
2%-2mm	2% for Dose Difference Criterion and 2mm for DTA Criterion
2D	Two-dimensional
3%-3mm	3% for Dose Difference Criterion and 3mm for DTA Criterion
3D	Three-dimensional
AAA	Analytical Anisotropic Algorithm
AP	Anterior-posterior
ART	Adaptive Radiotherapy
CBCT	Cone Beam Computed Tomography
CT	Computed Tomography
CUDA	Compute Unified Device Architecture
DD	Delivered Dose
DICOM	Digital Imaging and Communications in Medicine
DIR	Deformable Image Registration
d_{max}	Depth of Maximum Dose
D_{max}	Maximum Dose
DPM	Dose Planning Method
DTA	Distance-to-agreement
DVF	Deformation Vector Field

DVH	Dose Volume Histogram
GPU	Graphics Processing Unit
GUI	Graphical User Interface
HN	Head and Neck
HU	Hounsfield Unit
HVT	Half-value Thickness
IMRT	Intensity Modulated Radiation Therapy
LINAC	Linear Accelerator
LR	Left-right
MADD	Maximum Allowed Dose Difference
MeV	Megaelectron Voltage
MLC	Multileaf Collimator
NTCP	Normal Tissue Complication Probability
OAR	Organ at Risk
PD	Plan Dose
PDD	Percentage Depth Dose
PSL	Phase-space-let
PTV	Planning Target Volume
QA	Quality Assurance
RMSD	Root-mean-square Difference
ROI	Region of Interest
SAD	Source to Axis Distance

SCD	Source to Collimator Distance
SD	Secondary Dose
SI	Superior-inferior
SRS	Stereotactic Radiosurgery
SSD	Source to Surface Distance
STP	Standard Pressure and Temperature
TCP	Tumor Control Probability
TPS	Treatment Planning System
VMAT	Volumetric Modulated Arc Therapy
VOI	Volume of Interest

ACKNOWLEDGEMENTS

First of all, I would like to express my deep gratitude to my supervisor, Dr. Steve Jiang. He introduced me to the field of Medical Physics and guided me through almost five years of learning and research. Whenever I have questions on projects or even doubts on my future, he is always there helping me and supporting me.

Secondly, I would like to thank my committee member Dr. Laura Cerviño, whose comments and suggestions are always helpful for my research. She supervised me on the deformable phantom project which will be presented in this dissertation. Another CART member Dr. Xun Jia plays an important role in my graduate study. Without his guidance and constant help, this dissertation would not have been possible. In addition, a thank you to Michael Folkerts who helped me to set up the TARGET web application.

I would also like to express my appreciation to University of California, San Diego Physics Department for allowing me to pursue my interests in Medical Physics, to Dr. Ken Intriligator for serving as the chair of my committee, and to Dr. Hans P. Paar, Dr. Clifford M. Surko, and Dr. Juan C. del Álamo for serving on my committee.

Chapters 2 contains material published in Physics in Medicine and Biology 2013. Graves, Yan J.; Jia, X.; Jiang, Steve B., IOP Publishing. The

dissertation author was the primary investigator and author of this paper. Chapters 2 also contains material being prepared for submission to Physics in Medicine and Biology. Graves, Yan J.; Folkerts, M.; Kim, G.; Teke, T.; Popescu, I. A.; Cerviño, L.; Jia, X. and Jiang, Steve B. 2013. The dissertation author was the primary investigator and author of this manuscript.

Chapter 3 contains material being prepared for submission to Physics in Medicine and Biology. Graves, Yan J.; Smith, A.; Rice, R.; Mell, L.; Jia, X.; Jiang, Steve B.; Cerviño, L. 2013. The dissertation author was the primary investigator and author of this manuscript.

VITA

Education

2013	Ph.D., Physics (Biophysics) University of California, San Diego
2009	M.S., Physics University of California, San Diego
2007	B.S., Physics and Mathematics Hong Kong University of Science and Technology

Journal Papers

Graves Y, Jia X and Jiang S, "Effect of Statistical Fluctuation in Monte Carlo Based Photon Beam Dose Calculation on Gamma Index Evaluation". *Phys. Med. Biol.,* 58(6): 1839-1853, 2013.

Townson R, Jia X, Tian Z, Graves Y, Zavgorodni S and Jiang S, "GPU-based Monte Carlo radiotherapy dose calculation using phase-space sources". *Phys. Med. Biol.,* 58(12): 4341-4356, 2013.

Li N, Zarepisheh M, Uribe-Sanchez A, Moore K, Tian Z, Zhen X, Graves Y, Gautier Q, Mell L, Zhou L, Jia X and Jiang S, " Automatic treatment plan re-optimization for adaptive radiotherapy guided with the initial plan DVHs". *Phys. Med. Biol.,* 58(24): 8725-38, 2013.

Montanari D, Scolari E, Silvestri C, Graves Y, Yan H, Cerviño L, Rice R, Jiang S and Jia X, " Comprehensive Evaluations of Cone-beam CT dose in Image-guided Radiation Therapy via GPU-based Monte Carlo simulations". *Phys. Med. Biol., submitted.*

Tian Z, Graves Y, Jia X and Jiang S, " Automatic Commissioning of a GPU-based Monte Carlo Radiation Dose Calculation Code for Photon Radiotherapy". *Phys. Med. Biol., submitted*.

Dong B, Graves Y, Jia X and Jiang S, "Optimal Surface Marker Locations for Tumor Motion Estimation in Lung Cancer Radiotherapy". *Phys. Med. Biol.* 57(24): 8201-8215, 2012.

Jia X, Gu X, Graves Y, Folkerts M and Jiang S, "GPU-Based Fast Monte Carlo Simulation for Radiotherapy Dose Calculation", *Phys. Med. Biol.* 56(22): 7017-7031, 2011.

Cerviño L, Jiang Y, Sandhu A and Jiang S, "Tumor Motion Prediction with Diaphragm as a Surrogate: a Feasibility Study". *Phys. Med. Biol.* 55(9): N221–N229, 2010.

ABSTRACT OF THE DISSERTATION

Computational and Physical Quality Assurance Tools for Radiotherapy

by

Yan Jiang Graves

Doctor of Philosophy in Physics (Biophysics)

University of California, San Diego, 2013

Professor Ken Intriligator, Chair
Professor Steve B. Jiang, Co-Chair

Radiation therapy aims at delivering a prescribed amount of radiation dose to cancerous targets while sparing dose to normal organs. Treatment planning and delivery in modern radiotherapy are highly complex. To ensure the accuracy of the delivered dose to a patient, a quality assurance (QA) procedure is needed before the actual treatment delivery. This dissertation aims at developing computational and physical tools to facilitate the QA process.

In Chapter 2, we have developed a fast and accurate computational QA tool using a graphics processing unit based Monte Carlo (MC) dose engine. This QA tool aims at identifying any errors in the treatment planning stage and machine delivery process by comparing three dose distributions: planned dose computed by a treatment planning system, planned dose and delivered dose reconstructed using the MC method. Within this tool, several modules have been built. (1) A denoising algorithm to smooth the MC calculated dose. We have also investigated the effects of statistical uncertainty in MC simulations on a commonly used dose comparison metric. (2) A linear accelerator source model with a semi-automatic commissioning process. (3) A fluence generation module. With all these modules, a web application for this QA tool with a user friendly interface has been developed to provide users with easy access to our tool, facilitating its clinical utilizations.

Even after an initial treatment plan fulfills the QA requirements, a patient may experience inter-fractional anatomy variations, which compromise the initial plan optimality. To resolve this issue, adaptive radiotherapy (ART) has been proposed, where treatment plan is redesigned based on most recent patient anatomy. In Chapter 3, we have constructed a physical deformable head and neck (HN) phantom with in-vivo dosimetry capability. This phantom resembles HN patient geometry and simulates tumor shrinkage with a high level of realism. The ground truth deformation field can be measured from built-in surface markers, which is then used to verify the accuracy of an

important ART step of deformable image registration. Our experiments also demonstrate the feasibility of using this phantom as an end-to-end ART QA phantom with an emphasis on testing the dose deliver accuracy.

1. Introduction

1.1 Overview of Radiation Therapy

Cancer is a term used for diseases caused by an overgrowth of abnormal cells. These cells are able to divide and grow rapidly to make new cancer cells, leading to the formation of malignant tumors and invasion into healthy tissue. Cancer is the second most common cause for death in the US after heart disease. More than 550 thousand Americans died of cancer in 2012 with over 1.5 million newly diagnosed cancer cases. Radiation therapy is one of the three modalities of cancer treatment, along with chemotherapy and surgery. A patient may receive radiation therapy before, during or after the surgery. When surgery is not an option due to risks of complication, radiation therapy is usually used alone to eliminate a tumor or in combination with chemotherapy. Nowadays, about two thirds of all cancer patients receive radiation therapy during the course of their treatments.

1.1.1 Radiobiology

Radiation therapy kills cancer cells by damaging their DNA through *direct* and *indirect* action. In direct action, the radiation excites or ionizes molecules in the DNA structures directly, while in indirect action, the radiation interacts with neighboring molecules (mainly water molecules) creating free radicals within the cells that can in turn damage the DNA. Biological damage to DNA usually refers to single or double strand breaks of the helical structure, and approximately 2/3 of these damages are due to indirect action. While a single strand break is often repairable by a number of mechanisms, most double strand breaks are lethal. Cancer cells eventually stop multiplying or die if the damage caused by radiation is not repaired.

Although normal cells are more likely to repair DNA damages than cancer cells, radiation still damages normal cells, potentially leading to severe complications. Figure 1.1 illustrates dose-response curves describing the observed effects of radiation exposure in relation to the radiation dose. A tumor control probability (TCP) curve represents the probability of tumor control (fraction of cancer cells killed) as a function of dose while a normal tissue complication probability (NTCP) represents the probability of a particular normal tissue complication from the dose. To achieve good treatment quality, a radiation dose is chosen such that it maximizes the TCP while minimizing the NTCP. The therapeutic ratio for a given dose level is defined as the ratio of TCP and NTCP.

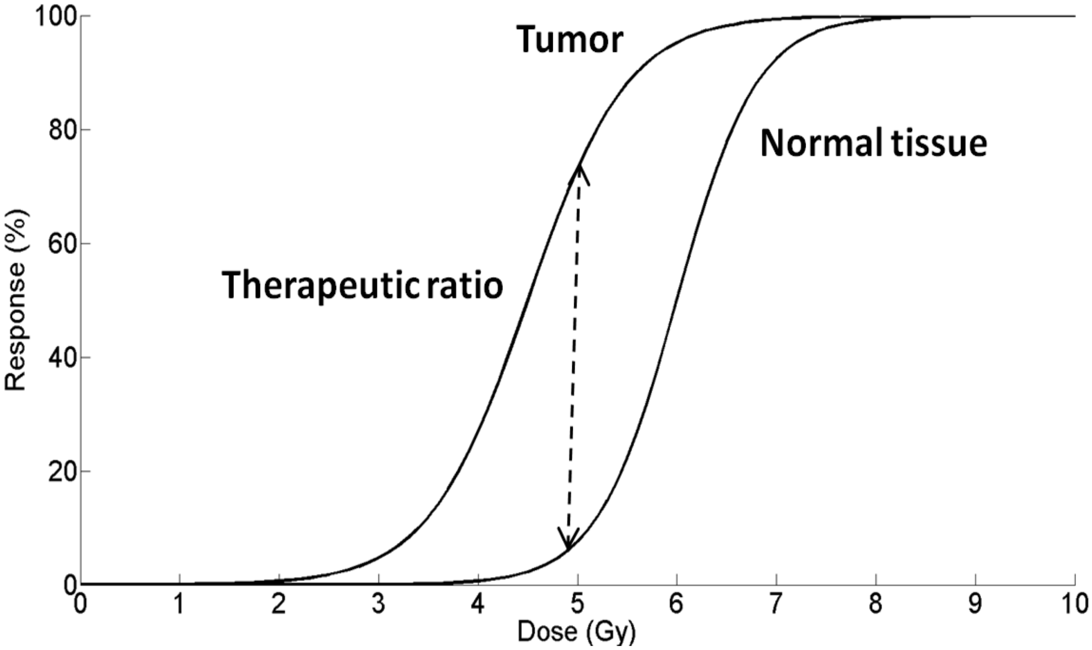

Figure 1.1: The therapeutic ratio from the tumor control probability and the normal tissue complication probability curves.

1.1.2 Typical Treatment Forms

External beam radiation therapy directs the X-ray beam to the tumor from outside patient. It is the most common type of radiation therapy and the subject of this dissertation. The radiation beam is usually generated by a machine call a linear accelerator (LINAC). The details of a LINAC with its beam modulators will be discussed in the following section.

The goal of radiation therapy is to deliver sufficient dose to the cancer cells while minimizing the dose to normal healthy tissues (Hall and Giaccia, 2006). To achieve this goal, many planning and delivery techniques have been developed, especially after the invention of computed tomography (CT) technology. A series of CT slices represent the 3D shape of the tumor and its relationship to surrounding organs. With this information, 3D conformal radiation therapy is possible. This method shapes the radiation beams from multiple angles to the shape of the tumor with the use of multileaf collimators (MLC) or custom fabricated heavy metal blocks. Due to the shielding of radiation beams, the dose to the normal tissue is reduced.

From the 1990's onward, modern radiation technology has evolved dramatically due to the advancement of computer power and related algorithms. One particular advancement is intensity modulated radiation therapy (IMRT) that delivers the radiation from a few fixed beam angles with variable intensities inside each beam. This method is able to increase the dose to the tumor target while reducing the dose to surrounding tissue. Figure 1.2 displays examples of prostate treatment plan with 3D conformal radiation therapy and IMRT techniques. Later, a rotational form of IMRT, volumetric modulated arc therapy (VMAT), was invented (Otto, 2008). This technique delivers radiation dose while continuously rotating the beam angle, which greatly reduces the clinical treatment time while maintaining the plan quality technology (Bedford, 2009; Bedford *et al.*, 2008; Popescu *et al.*, 2009). More details of modern treatment planning and technologies will be presented later.

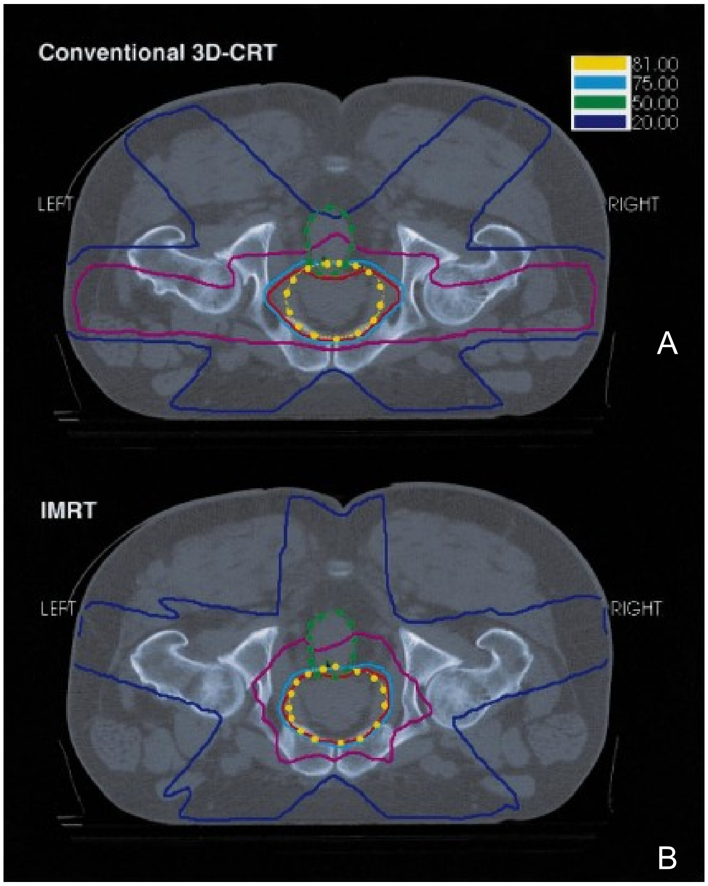

Figure 1.2: Examples of a prostate plan with different technologies. (A) 3D conformal radiation therapy. (B) IMRT with 5 fields. (Adopted from Zelefsky *et al.* (2000))

1.2 Linear Accelerator

A LINAC is usually mounted isocentrically on a gantry, so that the radiation source can rotate 360° about a horizontal axis. The intersection of the beam axis and the axis of the gantry rotation is known as the *isocenter*. A typical LINAC machine is shown in Figure 1.3.

A LINAC produces a photon beam by accelerating a high energy electron beam to strike a target. Photons are mainly produced by bremsstrahlung while the characteristic X-ray emission is negligible for electron energy in the megavoltage range. The bremsstrahlung X-rays have a spectrum of energies with the maximum energy equal to the peak incident electron energy.

The intensity of the photon beam exiting the target is peaked in the forward direction and the beam passes through a system of collimators and beam modulators, shown in Figure 1.4. The primary collimators shape the beam to a large fixed area and a flattening filter is designed to attenuate the forward peaked beam more in the middle area than the peripheral region in order to make the beam intensity uniform across the field at a certain depth in water (e.g. 10cm). Then the flattened beam passes through the dual flat ion chambers which monitor the radiation output and beam flatness. The above mentioned components in the LINAC head are fixed and patient-independent.

After passing through the ion chambers, the beam is further collimated by two pairs of moving jaws into a rectangular field . The maximum field size is typically $40x40cm^2$. The MLC consists of multiple pairs of tungsten leafs, ranging from 40 to 60 pairs, shown in Figure 1.5. Each leaf is individually controlled by a motor and can move independently in and out in order to block to the beam. The MLC can shape the radiation beam to the shape of tumor and it also allows for the complex intensity modulation.

Figure 1.3: A Varian version of a linear accelerator with cone beam computed tomography mounted. (Image courtesy of Varian Medical System Inc.)

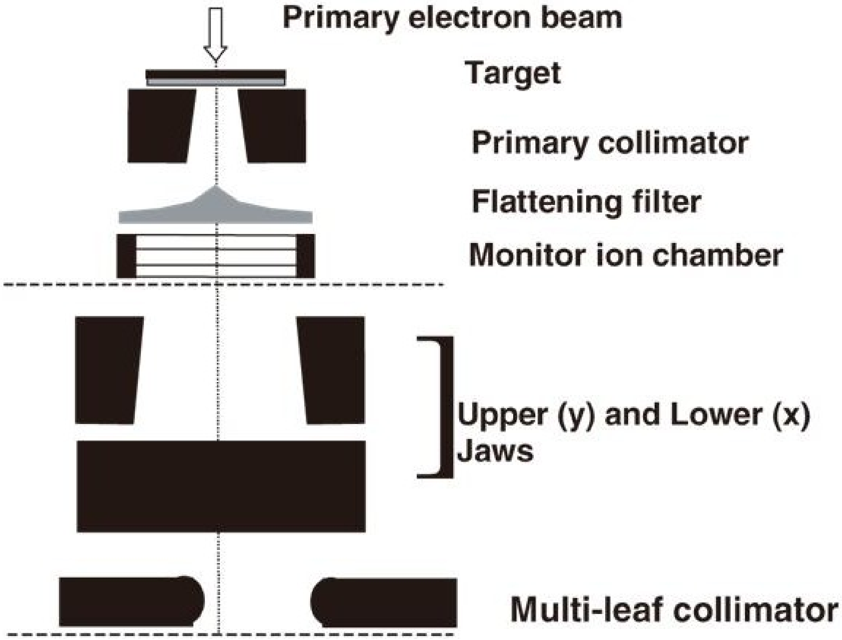

Figure 1.4: Schematic representation of LINAC head components. (Adopted from Verhaegen and Seuntjens (2003))

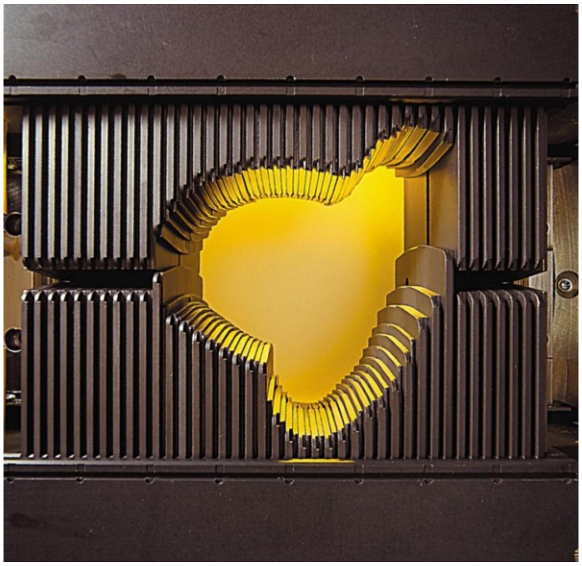

Figure 1.5: Multileaf collimator. (Image courtesy of Varian Medical System Inc.)

1.3 Radiation Treatment Process

Planning and delivery of external beam radiation therapy is a complex process and a brief overview of the process is explained here. The first step is treatment simulation, where a CT scan of a cancer patient is often performed and used to build a virtual patient model in a treatment planning system (TPS). A optimization algorithm in TPS generates a treatment plan that delivers a highly conformal dose to the target while keeping the dose level to important normal organs below tolerances. Due to the complexity of modern treatment planning and delivery techniques, a patient-specific plan quality assurance (QA) process must be performed to ensure the accuracy and deliverability of the plan. Once the treatment plan passes the QA tests, it is ready for delivery. In most cases, the patient will have to receive radiation dose through multiple treatment fractions where each time a fraction of the total planned dose is given. This allows normal cells to repair and increases the likelihood that cancer cells are exposed to radiation in the radio-sensitive phase of the cell cycle (Connell and Hellman, 2009). In each treatment fraction, the patient must be first positioned carefully under the treatment machine to match the virtual patient model as closely as possible and the treatment plan will be then delivered. The treatment fractions usually last over a course of several weeks. The whole radiation therapy process diagram is shown in Figure 1.6.

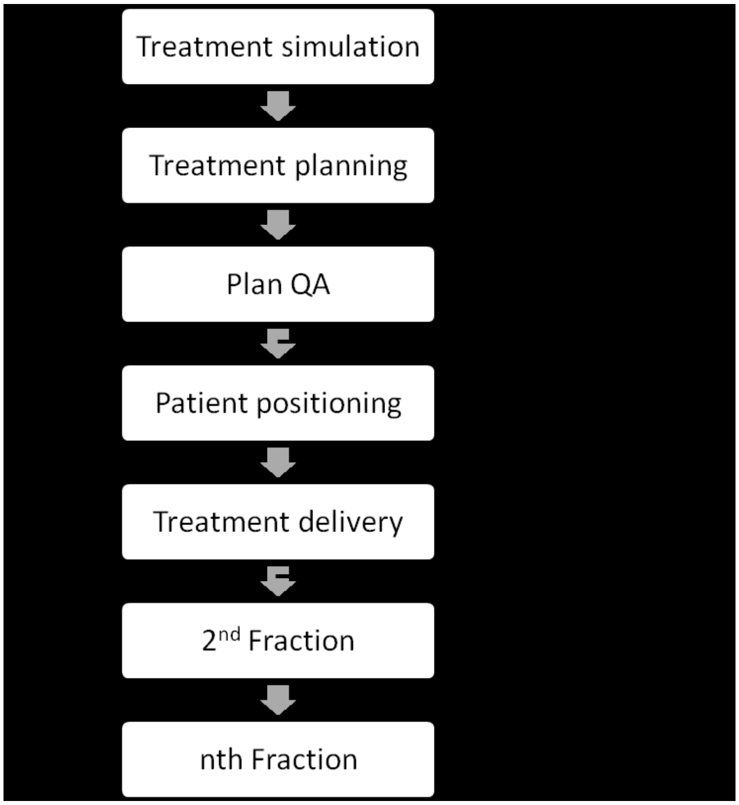

Figure 1.6: Radiation therapy process.

1.3.1 Treatment Simulation

The treatment simulation is primarily based on a CT scan. In a CT scan. a 3D volume of a patient's anatomy is reconstructed using advanced numerical algorithms. The resulting volumetric image is a discretized description of the patient body using a 3D data array. Each entry of the array, called a voxel, measures the linear attenuation of the X-ray locally at the voxel (Kak *et al.*, 1988). A voxel in a CT scan is expressed in terms of relative radiodensity in the Hounsfield Unit (HU) scale. For a voxel with a linear attenuation coefficient μ_X, HU is defined as:

$$HU = 1000 \times \frac{\mu_X - \mu_{water}}{\mu_{water} - \mu_{air}}, \tag{1.1}$$

where μ_{water} and μ_{air} are the linear attenuation coefficients of water and air, respectively. In this HU scale, the radiodensity of distilled water at standard pressure and temperature (STP) is defined as zero HU and the radiodensity of air at STP is defined as -1000 HU.

The acquired CT scan is imported into a TPS to form a virtual patient which is used in the next step, treatment planning.

1.3.2 Treatment Planning

The treatment planning process consists of tumor and organs contouring, plan optimization, and final dose calculation. On the virtual patient, tumor target (or planning target volume (PTV)) and surrounding critical organs at risk (OAR) are first delineated by a physician. Then the anatomic properties (i.e. size and shape) and relationship are used in subsequent plan optimization step.

Current TPS approaches plan generation as an optimization procedure. As such, one first defines a set of dose constraints on various OARs and PTV. Then a powerful optimization algorithm finds the treatment beam parameters (e.g. the number of beams, beam angles, *etc.*) to best match all the input criteria. Modern treatment techniques such as IMRT delivers radiation from a set of fixed beam angles and allow for the intensity of each beam to be modulated. Specially, a board beam field is de-composited into a grid of small *beamlets* and the weights of thousands of beamlets from different beam angles are adjusted iteratively in the optimization algorithm. After the non-uniform beam intensities, called optimal *fluence maps,* are obtained, they must be translated into deliverable MLC leaf motion sequences, considering MLC transmission and MLC mechanical constraints (e.g. leaf width, leaf speed, and leaf motion range, *etc.*). VMAT is an advanced rotational form of IMRT that delivers dose in one or two continuously rotating arcs around the patient while the radiation beam in constantly on. In VMAT, MLC shape can be varied and optimized as well as the dose rate and gantry speed of the LINAC, making it far more complicated than IMRT.

In the last step of treatment planning, the TPS uses the models of the virtual patient and the treatment machine to calculate the expected dose distribution in the patient with the set of optimized beam parameters. Dose volume histogram (DVH) is generated to evaluate the plan quality. Specifically, a DVH for a given organ is a function $V(D)$ which quantifies the volume of this organ that receives at least a dose level D. Typical DVHs for an OAR and a PTV are displayed in Figure 1.7. The PTV DVH appears almost as a step function with a jump at the prescription dose, indicating a good coverage with the prescribed dose level. But the OAR near the PTV is unavoidably irradiated, as nonzero doses cover part of its volume.

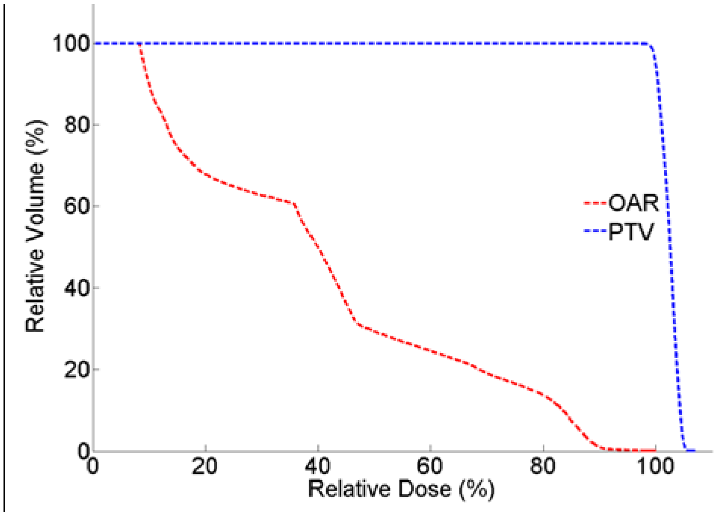

Figure 1.7: A typical DHV plot.

1.3.3 Treatment Delivery

After treatment planning, a patient-specific plan QA step needs to be performed to ensure the patient safety. Since this is the focus of the dissertation, we will give a detailed description of this step in the next section.

On the day of the treatment, it is necessary to first properly position the patient on the treatment couch relative to the LINAC to match the virtual patient model in the TPS as closely as possible. Recently, cone beam computed tomography (CBCT) technology has been introduced to obtain a volumetric image of the patient in treatment position. A typical on-board CBCT imaging system, is shown in Figure 1.3. The CBCT image can be automatically registered to the CT image used in the planning stage and therefore assist the patient alignment. After the patient setup, the radiation delivery starts and it is important to monitor the patient such that the well set patient position remains throughout the treatment.

1.4 Adaptive Radiotherapy

In a conventional radiation therapy process, a treatment plan is generated based on a snapshot of the patient anatomy captured during the treatment simulation, and the plan is delivered fractionally over a number of weeks. However, patient's anatomy may change significantly from fraction to fraction during the whole treatment course. Examples of such variations include tumor regresses in response to the treatment, organ deformations due to different filling status or changes in relative position between tumor and neighboring tissue. (Barker *et al.*, 2004; Lee *et al.*, 2004; Yan *et al.*, 2005; Lee *et al.*, 2008; Beadle *et al.*, 2009; Tyagi *et al.*, 2011). Figure 1.8 shows an example of a head and neck (HN) cancer patient treated at the UC San Diego experiencing the tumor shrinkage (contoured in blue) from the pre-treatment CT scan and the re-CT scan in the fourth week of the treatment course.

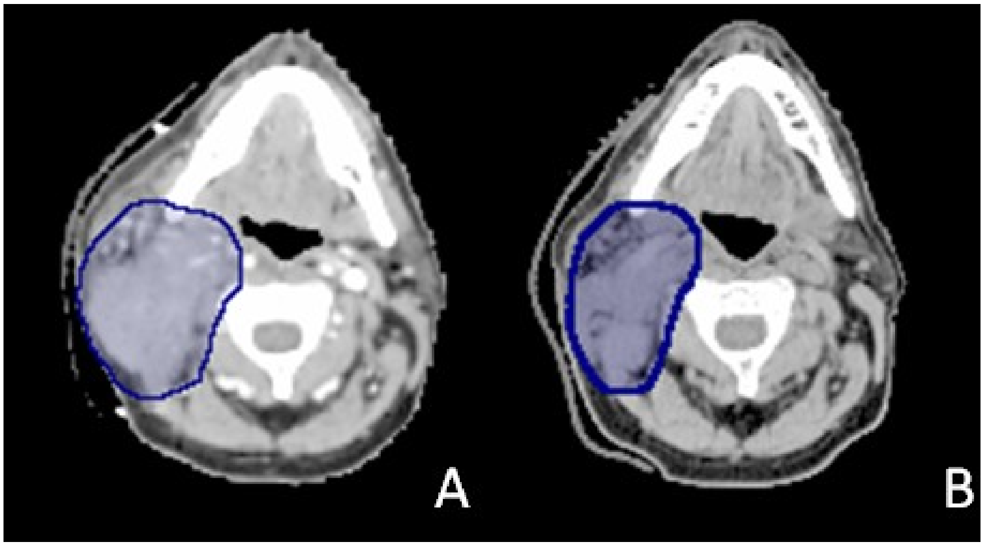

Figure 1.8: An example of a head and neck cancer patient experiencing tumor shrinkage. (A) CT scan before treatment. (B) Re-CT scan in the fourth week of the treatment course. Blue contours indicate the tumor area.

These anatomical variations can compromise the initial treatment plan quality and therefore treatment outcomes (Antolak *et al.*, 1998; van de Bunt *et al.*, 2006). To solve this problem, adaptive radiation therapy (ART) has been proposed in which the treatment plan is modified or re-optimized based on the latest patient anatomy to maintain the plan quality (Yan *et al.*, 1997). In a typical clinical practice, the main workflow of ART includes (1) obtaining the new anatomy geometry before a fraction, (2) contouring PTV and OARs on the new geometry and (3) modifying the plan or conduct re-optimization to generate a new plan. If the new plan is immediately delivered at the current fraction, we refer this as an online ART approach. In contrast, an offline ART refers the case where the new plan is used for future treatment fractions.

In the past decade, a lot of research efforts have been devoted to developing novel ART techniques (e.g.(Burridge *et al.*, 2006; Schulze *et al.*, 2009; Foroudi *et al.*, 2009; Gu *et al.*, 2010; Men *et al.*, 2010)). Among them, deformable image registration (DIR) algorithm is an important one. DIR refers to the problem of establishing a correspondence between voxels in a reference planning CT image and that in a daily image. Once such a correspondence is obtained, it can be used to propagate the contours of the PTVs and the OARs from the initial planning CT to the daily patient images (Wang *et al.*, 2005; Lu *et al.*, 2006; Zhang *et al.*, 2007; Hardcastle *et al.*, 2012). This enables an auto-segmentation on the daily patient geometry and increases the efficiency for both online and offline ART implementation in clinics. The correspondence derived from a DIR algorithm has also been used for dose accumulation, whereby the delivered dose is reconstructed on the daily patient image and is transferred back to the reference planning CT geometry (Lu *et al.*, 2006). The delivered dose accumulation helps the physician to objectively evaluate the treatment and decide when and how a re-plan or plan modification is needed. Moreover, DIR can also facilitate the re-planning process. Studies have been conducted to use the generated deformation fields between the planning CT and the daily CBCT or CT to morph the pre-existing MLC apertures or leaf sequences for a fast online re-planning (Ahunbay *et al.*, 2009).

For the details of plan modification or re-planning, please refer to multiple references (Wu *et al.*, 2002; Mohan *et al.*, 2005; de la Zerda *et al.*, 2007; Wu *et al.*, 2008; Lu *et al.*, 2008; Men *et al.*, 2009; Men *et al.*, 2010).

1.5 Quality Assurance

1.5.1 Plan Quality Assurance

Compared with conventional radiation therapy, the treatment planning for modern IMRT and VMAT technologies are much more complicated, in which a long list of beam parameters are optimized. Meanwhile, the machine deliveries are also more challenging. In IMRT, since the dose gradient may be large near OARs, the MLC leaf position accuracy is curial. In VMAT, the precise controls of beam gantry rotations and dose rate variations are additional requirements for an accurate deliver of the planed dose. Therefore potential errors in IMRT and VMAT may occur both in the dose calculation stage in TPS and in the beam delivery stage. Considering the serious consequences caused by those errors, a QA procedure is needed before the first treatment fraction for patients' safety to ensure the intended that plan dose is delivered to patients. This is referred as a patient-specific plan QA.

Current IMRT and VMAT patient-specific plan QA procedures can be separated into 2D dosimetry and 3D dosimetry approaches. The 2D dosimetry approaches compare the calculated planar dose distributions with the 2D measurements using radiographic film, matrices of detectors (Korreman *et al.*, 2009; Li *et al.*, 2009) or portal imagers (Nicolini *et al.*, 2008). For instance, a treatment plan is delivered to a phantom in which a radiographic film and an iron chamber are is inserted, or is directly irradiated to a 2D detector matrix. The calculated plan doses are then compared to the measured values. However, one of the limitations is that these measurements are time consuming and tedious, since they require accurate phantom or detector set up on the LINAC. Portal imagers have also been used for plan QA, where photon fluence is measured directly and is compared to the calculations. One critical problem in all of these 2D dosimetry methods is that the plan accuracy and delivery precision are only checked in a plane. Ideally the 3D dose distributions should be verified considering the complexity of IMRT and VMAT.

3D patient-specific plan QA methods include 3D dose measurements with advanced 3D dosimetric phantoms or dosimeters (Richardson *et al.*, 2003; Islam *et al.*, 2003; Feygelman *et al.*, 2009; Letourneau *et al.*, 2009) and 3D plan dose reconstruction using exit portal dosimetry or machine delivery records. The first popular method is to deliver a plan to 3D dosimetric phantoms and compare measurements with calculations. Examples of commercially available 3D dosimetric phantoms are shown in Figure 1.9.

Those 3D phantoms and detectors also require set up procedure and they don't represent patient geometries or tissue heterogeneity. Hence, these measurements cannot directly verify the plan dose on the patient's geometry and therefore they are not fully patient-specific QA methods. Another method, exit portal dosimetry, uses the electronic portal imaging device (EPID) to reconstruct 3D dose distributions within a patient or a phantom using a back projection method or Monte Carlo (MC) simulations (van Elmpt *et al.*, 2007; McDermott *et al.*, 2008; van Etmpt *et al.*, 2008). Yet, the accuracy of this approach heavily depends on dosimetric calibrations of EPID imagers and the verification of the imagers' geometrical accuracy, which becomes a barrier to implement this method in most clinics. Recently, LINAC log file based QA has been proposed. Machine log files record delivery information, such as cumulative dose fraction, beam on status, and MLC leaf positions, *etc*, during the plan deliveries. The accuracy of the recorded information has been validated by many research groups using film measurement, 2D detector array and portal imagers (Li *et al.*, 2003; Zygmanski *et al.*, 2003; Zeidan *et al.*, 2004). Hence using the delivery information recorded in the log files to reconstruct the dose distribution on patient images is a straightforward and accurate approach (Luo *et al.*, 2006; Schreibmann *et al.*, 2009; Teke *et al.*, 2010). Luo *et al.* (2006) and Teke *et al.* (2010) have incorporated log files into MC simulations for IMRT and VMAT QA purpose. However, based on our knowledge, computational time for these MC simulations is long due to the nature of the MC method and thus limiting the adoptions of these computational tools in clinics.

In light of these facts, the first goal of this dissertation is to develop a fast and practical computational tool for IMRT and VMAT plan QA purpose. The tool should comprehensively check potential errors in plan dose calculation in TPS and beam delivery. It should also add minimum burden onto current clinical practice to facilitate clinical adoptions.

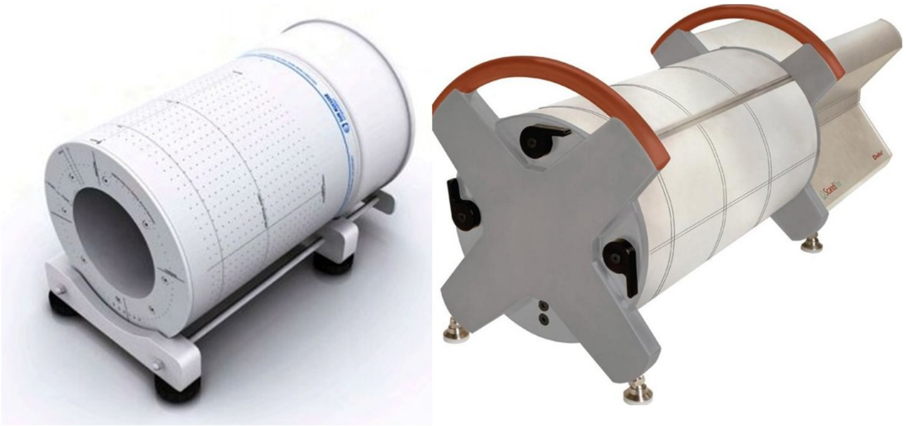

Figure 1.9: Examples of commercially available 3D dosimetric phantoms. *(*Image courtesy of ScandiDos AB and Sun Nuclear)

1.5.2 Adaptive Radiotherapy Quality Assurance

Clinical implementation of ART brings new challenges to the normal IMRT and VMAT QA program. As mentioned previously, the DIR algorithm that is heavily used in image segmentation, delivery dose accumulation and possibly re-planning, is a very crucial tool for ART. Hence the accuracy of a DIR algorithm has a significant impact for a safe and accurate implementation of ART technology. Over the years, a lot of efforts have been devoted to developing accurate DIR algorithms (Thirion, 1998; Zitova and Flusser, 2003; Lu *et al.*, 2004; Brock *et al.*, 2005; Yang *et al.*, 2008; Holden, 2008; Gu *et al.*, 2010; Zhen *et al.*, 2012). It has also been a research topic to evaluate the accuracy of these algorithms. Common evaluation methods include comparing the calculated deformation vector fields (DVF) with that derived based on landmark points (Lu *et al.*, 2004; Brock *et al.*, 2005; Kaus *et al.*, 2007; Gu *et al.*, 2010), calculating reference and deformed image similarity metrics (Lu *et al.*, 2004; Castadot *et al.*, 2008; Zhen *et al.*, 2012) and inspecting contours on both reference and deformed images (Foskey *et al.*, 2005).

Phantom-based deformable registration validation has also received a lot of attentions. Physical deformation displacements can be directly derived from the phantoms and compared with the calculated ones. Several deformable phantoms have been built for this purpose. Kashani *et al.*, (2007) and Serban *et al.*, (2008) designed two different lung phantoms that can mimic the diaphragm motion and thus to deform the modeled lung tissue. They performed quantitative evaluation of DIR algorithms based on the embedded landmarkers in the phantoms. Yet, the landmarks are usually visible in the images and DIR algorithm actually use them to achieve good registrations locally. In contrast, registration errors may be somewhat large elsewhere, especially in homogenous tissue regions. The research group at UC San Francisco have also designed two anthropomorphic deformable phantoms, a

HN phantom and a pelvic phantom (Kirby *et al.*, 2011; Kirby *et al.*, 2013), shown in Figure 1.10. Both of them resemble the corresponding tumor sites closely. A grid of nonradiopaque surface makers are placed in the phantom, which can be captured in the optical camera images but are invisible in the CT images for DIR algorithms. The actual deformation can be extracted from the optical camera images and used to verify the DIR algorithm output.

However, as pointed out by Yan (2008), a clinical QA workflow for ART demands a deformable phantom for both (1) DIR algorithm accuracy test and (2) delivered dose verification. So far, there is a lack of a deformable phantom that also provides dosimetric information for the complete ART QA purpose. Therefore, the second goal of this dissertation is to design and fabricate a physical deformable phantom tool, which should represent realistic patients' anatomy and include in-vivo dosimetry. This phantom tool will be used to verify the DIR algorithm accuracy, as well as to serve as an end-to-end QA for ART dosimetry.

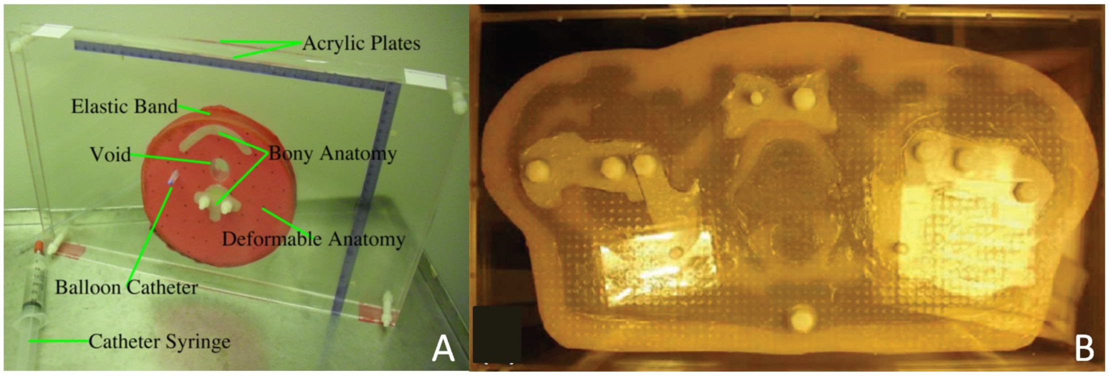

Figure 1.10: UC San Francisco deformable phantoms. (A) A HN phantom. (B) A pelvic phantom.

2. Computational Quality Assurance Tool

2.1 Overview

The purpose of a patient-specific plan QA is to identify possible errors in the TPS plan dose calculation and in the beam delivery before the treatment is actually delivered the patient. The accuracy of plan dose calculation in the TPS plays a crucial role in the success of radiotherapy. For instance, an inaccurate dose calculation in the treatment planning stage leads to a consequently faulty radiation dose delivered to the patient over the entire treatment course. Because of the high accuracy of the MC method, it is desirable to verify the plan dose calculated by TPS by comparing it with another dose independently calculated using the MC method (Yang *et al.*, 2005; Calvo *et al.*, 2012). Recently, the extension to incorporate machine log files into MC dose calculation helps to detect the potential beam delivery failure, since the machine log files record all bean delivery information necessary for the reconstruction of the delivered dose (Luo *et al.*, 2006; Teke *et al.*, 2010).

Yet, MC method is a statistical approach for dose calculations. A large number of particles are to be simulated in order to yield a satisfactory level of uncertainty. In both of the two aforementioned applications, the long computational time of existing MC dose engines limits their applications in routine clinics. Recently, with the advancements of graphics processing unit (GPU) in general purpose scientific computations, MC simulation codes have been successfully developed on the GPU architecture and high speed-up factors have been achieved, making the computational efficiency acceptable for clinical applications. (Jia *et al.*, 2010; Hissoiny *et al.*, 2011; Jia *et al.*, 2011a).

In this chapter, we will present our researches on the developments of a fast and accurate QA computation tool based on a GPU based MC dose engine. This tool performs secondary dose calculations to verify the plan dose accuracy. It also reconstructs delivered dose using machine log files to ensure beam deliverability, as well as to validate the delivery dose accuracy.

The rest of this chapter will be organized as follows. Section 2.2 introduces the MC simulation methods for radiation dose calculations with a focus on the GPU based MC dose engine, gDPM. Section 2.3 will present our investigations on the effects of statistical uncertainty in MC based dose on a commonly used dose comparison matrix, γ-index. To avoid those effects on the γ-index evaluation test, a GPU based denoising method for MC based dose calculations is presented in Section 2.4. In Section 2.5, a beam source modeling and the commissioning method have been developed particularly for this QA computation tool. Additionally, fluence map generation is discussed in Section 2.6. A web application for this GPU based MC QA tool is finally presented in Section 2.7.

2.2 Monte Carlo Simulation for Dose Calculation

2.2.1 Basics of Monte Carlo Method for Dose Calculation

MC method is commonly considered as the most accurate one for dose computation in radiotherapy. This method follows a particle propagation through medium step by step based on fundamental physical interaction process between the radiation and the matters. A large number of particle histories is simulated to provide a description of the average quantities, i.e. dose distributions, while reducing the uncertainty to an acceptable level.

A brief introduction of photon and electron interactions in the radiotherapy energy range is presented here. When a photon propagates through the medium, it may be absorbed or scattered by the medium due to various physical interactions. There are four main interaction types: Compton scattering, photoelectric effect, pair production and Rayleigh scattering. In

Compton scattering, the incident photon interacts with a valence electron resulting in the ejection of the electron and the emission of a deflected and less energetic photon. In the photoelectric effect, all of the incident photon's energy is absorbed by an orbital electron which is ejected from the atom with kinetic energy equal to the incident photon's energy less the binding energy. In pair production, the incident photon is transformed into an electron and a positron through interaction with a nucleus. In Raleigh scattering, an atom absorbs the incident photon and immediately radiates photon of the same energy in a different direction. In the therapeutic photon beam, Compton scattering is the dominant interaction in mega-voltage energy range, while the Rayleigh scattering occurs with a very low probability and is typically neglected in MC simulations.

In contrast to photons that interact with the matter in a discrete manner, electrons are constantly affected by the surrounding medium due to the long range Coulomb interaction. It is computationally prohibitive to simulate all of these interactions. Yet, most of these small interactions do no alter the electron status significantly. Hence, a "condensed history" technique has been proposed to combine these many "small-effect" collisions into a single, large-effect, virtual interaction (Berger, 1963) for the purpose of speeding up computations. Occasionally, electrons also undergo elastic collisions with large deflection angles, and other interactions, e.g. bremsstrahlung and inelastic collisions, resulting in loss of energy and excitations and ionizations of the medium. These effects have to be simulated accurately to maintain overall calculation accuracy. Secondary electrons, called “delta particles”, are also tracked following the same process described above.

Over the years, a number of general purposed MC codes have been written in radiation therapy, such as EGS4/5 (Nelson *et al.*, 1985; Bielajew *et al.*, 1994; Hirayama *et al.*, 2010), EGSnrc (Kawrakow, 2000), MCNP (Briesmeister, 1993), PENELOPE (Baro *et al.*, 1995; Sempau *et al.*, 1997; Salvat *et al.*, 2009), EGSnrc (Kawrakow, 2000) and GEANT4 (Agostinelli *et al.*, 2003). High efficiency dose calculation packages, for instance VMC++ (Kawrakow *et al.*, 1996), MCDOSE/MCSIM (Ma *et al.*, 1999; Ma *et al.*, 2002) dose planning method (DPM) (Sempau *et al.*, 2000),etc.. have also been developed by employing variance reduction techniques or simplify particle transport physics. Readers who are interested in this topic are referred to multiple references for a comprehensive review of the simulation techniques and variance reduction and efficiency enhancing methods (Larsen, 1992; Kawrakow and Bielajew, 1998; Kawrakow, 2000; Ma *et al.*, 2002; Kawrakow *et al.*, 2004; Kawrakow, 2005).

2.2.2 GPU Based Monte Carlo Code

A straightforward way of boosting MC simulation efficiency is to port the MC codes onto parallel computing architectures. For instance, Tyagi *et al.*,

(2004) parallelized DPM on a CPU cluster and achieved almost linear speed-up with the number of processors being used. However, using a CPU cluster for dose calculation in clinics are impractical due to the high cost of facility deployment and maintain, as well as inconvenience to access.

Recently, GPU based high performance computing has offered us a new approach to accelerate computational demanding tasks. Originally designed for manipulating computer graphics-related operations, GPU is a specialized electronic hardware in almost all modern computers. It consists of an enormously large number of computational cores as well as dedicated memory spaces. A typical hardware structure of a GPU card is shown in Figure 2.1. Although the processing speed of each core may not be as high as a typical CPU, the total processing power of a GPU is much higher. One can typically obtain a Tera flops (float operations per second) on a single GPU card, making it a personalized supercomputer on a desktop workstation.

In late 2006, NVIDIA introduced Compute Unified Device Architecture (CUDA) architecture and tools to make GPU programming straightforward (NVIDIA, 2013). A bloom of GPU computing appears after that. In particular, GPUs have been employed to successfully accelerate many computationally intensive tasks in medical physics (Xu and Mueller, 2005; Sharp *et al.*, 2007; Samant *et al.*, 2008; Yan *et al.*, 2008; Men *et al.*, 2009; Gu *et al.*, 2010; Jacques *et al.*, 2010; Jia *et al.*, 2010; Men *et al.*, 2010; Gu *et al.*, 2011a; Gu *et* *al.*, 2011b; Hissoiny *et al.*, 2011; Jia *et al.*, 2011b; Jia *et al.*, 2011a; Townson *et al.*, 2013), ranging from image processing to radiation dose calculations.

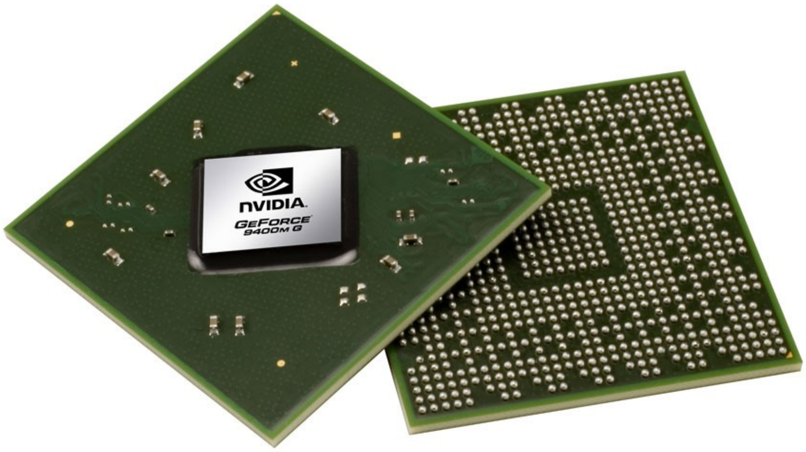

Figure 2.1: A typical hardware structure of a GPU card. *(*Image courtesy of NVIDIA)

One successful GPU based MC dose calculation engine is gDPM (Jia *et al.*, 2011a). In this package, each GPU thread simulates one particle transport. By carefully designed simulation scheme to separate photon transport and electron transport, the so-called GPU thread divergence problem is partially relieved, which would severely degrade computational efficiency if it is not addressed appropriately. Besides this simulation scheme, hardware supported linear interpolation and a high-performance random number generator are also utilized to further speed up the MC calculations. With all of these novel techniques, gDPM can finish a realistic IMRT or a VMAT plan calculation well within a minute, achieving 69-87x speedup compare to CPU based dose computations. Please refer to the reference (Jia *et al.*, 2011a) for the details of this GPU based MC dose calculation engine. Throughout the whole dissertation, gDPM will be used whenever MC based dose calculation is needed.

2.3 Monte Carlo Dose Uncertainty on Gamma-index Evaluation

2.3.1 Overview of Gamma-index Evaluation

Dose distribution comparison is a frequently performed task in radiotherapy especially for QA tasks, where the degree of agreement between an evaluation dose distribution and a reference one is established using some quantitative metrics. For example, in a typical plan QA procedure, a treatment plan is delivered to a phantom before the actual treatment, and the measured dose distribution is compared with the calculated dose distribution by TPS. Over the years, several dose comparison methods have been developed, including the quantitative dose difference test, the distance-to-agreement (DTA) test (Vandyk *et al.*, 1993; Harms *et al.*, 1998), the composite analysis for both dose difference and DTA (Shiu *et al.*, 1992; Cheng *et al.*, 1996; Harms *et al.*, 1998), the γ-index test (Low *et al.*, 1998; Depuydt *et al.*, 2002; Low and Dempsey, 2003; Bakai *et al.*, 2003; Stock *et al.*, 2005; Wendling *et al.*, 2007; Ju *et al.*, 2008; Chen *et al.*, 2009; Yuan and Chen, 2010; Low, 2010; Gu *et al.*, 2011b), and the test based on the maximum allowed dose difference (MADD)

(Jiang *et al.*, 2006). Among these methods, the γ-index test is the one most commonly used. This method combines quantifications of dose differences between two dose distributions in both the dose domain and the spatial domain. This allows for the toleration of spatial shifts when comparing the two dose distributions, which is clinically acceptable, and avoids an exaggeration of dose differences in the area of a high dose gradient. Moreover, the γ-index test is quantitatively comprehensible. Based on the user specified criteria, e.g. 3% for the dose difference criterion and 3 mm for the DTA criterion (3%-3mm), the user can judge how good the agreement is based on the value of the γ-index. The smaller the γ-index value is, the closer the two dose distributions are.

When we have two dose distributions to be compared, D_r and D_e, the γ-index at a comparison point $(r_r, D_r(r_r))$ is defined mathematically as

$$\gamma(r_r) = \min_{r_e}\left\{\sqrt{\frac{|r_e - r_r|^2}{\Delta r^2} + \frac{|D_e(r_e) - D_r(r_r)|^2}{\Delta D^2}}\right\}. \tag{2.1}$$

Here $D_r(r_r)$ is the reference dose distribution at the position r_r and $D_e(r_e)$ is the evaluation dose distribution at position r_e. ΔD and Δr are dose difference and DTA criteria. If the γ-index is equal to or less than 1, the dose at the spatial point r_r is considered to pass the test.

The graphical interpretation of the γ-index has been established previously (Ju *et al.*, 2008) and illustrated in Figure 2.2(a). Specifically, the γ-index is defined as the minimum Euclidian distance from the point O_r to the evaluation dose curve. In practice, the evaluation dose is usually defined at discrete spatial locations. To the first order approximation, Ju *et al* assumed a linear interpolation of the dose values between neighboring spatial points, and developed a simple and efficient γ-index calculation algorithm. This method is widely used nowadays, including the GPU base γ-index algorithm presented following.

2.3.1.1 GPU Based Gamma-index Evaluation

Due to the interpolation of dose grid and exhaustive search of the closest Euclidean distance in dose-distance space, the γ-index algorithm is a computational intensive task, especially when dealing with 3D γ-index calculations. Gu *et al* (2012b) implemented the γ-index algorithm on GPU using the CUDA programming environment with the geometric method (Ju *et al.*, 2008). As opposed to processing data in a serial manner, the search of closest Euclidean distance in dose-distance space can be parallelized for a large number of reference points and executed simultaneously using multiple threads. However, the number of involved evaluation points varies among threads depending on the dose difference at each spatial point, leading to threat divergence and hence longer computational time. To solve this issue, a radial pre-sorting technique (Wendling *et al.*, 2007) has been employed to pre-sorted the voxels according to the dose difference to make all threads simultaneously executed by the GPU have similar computation burdens. This strategy minimizes the divergence between GPU threads, considerably increasing computational efficiency.

With these techniques, this GPU based γ-index algorithm, gGamma, can accomplish a 3D dose comparison within a few seconds, yielding 45–75x speedup compared to CPU implementations. We are going to use this code for all the γ-index evaluation tasks throughout the whole dissertation.

2.3.2 Motivation

In many contexts, especially in QA procedures, the γ-index test is used to evaluate the agreement between two dose distributions, where one of them is calculated by MC simulations. In addition, in our proposed QA tool workflow, we will encounter a situation where two dose distributions to be compared are both calculated by MC simulations. However, MC is a statistical method and the statistical fluctuation is unavoidable in the resulting dose distributions. This fluctuation may have non-negligible impacts on the γ-index values and hence lead to biased conclusions from the γ-index test (Low and Dempsey, 2003; Low, 2010). This fact is easily understood from the graphical interpretations of the γ-index (Ju *et al.*, 2008). Let us consider a simple case where two 1D dose distributions are compared as in Figure 2.2(a). Suppose we plot the two dose distributions, $\overline{D_r}$ and $\overline{D_e}$ with normalized coordinates $r/\Delta r$ and $D/\Delta D$, where $\overline{D_r}$ and $\overline{D_e}$ are the normalized reference dose distribution and the normalized evaluation dose distribution respectively; Δr and ΔD are DTA and dose-difference criteria, respectively. It has been shown that the γ-index value at a coordinate r, denoted as γ_0, is simply the minimum Euclidian distance from the point O_r to the evaluation dose distribution, which is graphically represented by a circle centered at O_r such that the evaluation dose distribution is tangent to it. Figure 2.2(b) illustrates an example of how the γ-index value changes due to the MC statistical fluctuations in the evaluation dose. Suppose with fluctuations the evaluation dose distribution $\overline{D_e}$ becomes $\overline{D_e'}$, the new γ-index value $\gamma_0^{'}$ could be different from the original one. Similarly, Figure 2.2(c) illustrates an example where the γ-index value is affected by the MC statistical fluctuations in the reference dose. Considering these scenarios, a few key questions need to be answered before comparing two dose distributions where MC doses are involved: while the γ-index value apparently depends on a specific random realization of the dose distributions, what is the impact on average? How significant is this impact on, the clinically more important quantity, gamma passing rate? Also, since the γ-index value is not symmetric with respect to the two distributions (Low and Dempsey, 2003; Low, 2010), we have one more question: Is the impact different when the statistical fluctuation exists in the reference dose, in the evaluation dose, or in both of them?

In the next section, we will systematically investigate the impacts of the MC statistical fluctuations on the γ-index test. Specifically, we will demonstrate that to the first order approximation, statistical fluctuation in the reference dose tends to overestimate γ-index values, while that in the evaluation dose tends to underestimate γ-index values when they are within the clinically relevant range.

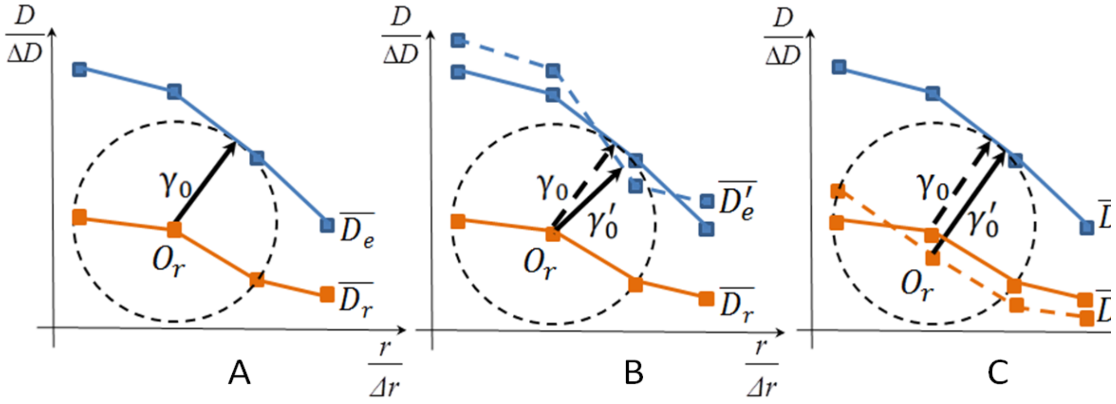

Figure 2.2: (A) Graphical interpretation of the γ-index in 1D. (B) An example demonstrating how the γ-index value changes due to MC statistical fluctuations in the evaluation dose. (C) An example demonstrating how the γ-index value changes due to MC statistical fluctuations in the reference dose.

2.3.3 Theoretical Molding

The γ-index value for a particular random realization of dose distributions is essentially a random variable. It is more meaningful to investigate how the γ-index test is affected on average, i.e. the average impact over all the random dose realizations.

2.3.3.1 MC Statistical Fluctuations in Reference Dose

Let us start the theoretical investigations based on the graphical representation of the γ-index (Ju *et al.*, 2008). In Figure 2.3, $O_{e1}O_{e2}$ is the line segment of the evaluation dose curve, O_r is the reference point, γ_0 is the original γ-index value and t parameterizes the deviation due to the statistical fluctuation. In this simplified model, the new γ-index value is always the minimum Euclidian distance from the point O_r to the line segment $O_{e1}O_{e2}$ of the evaluation dose curve, not to the other line segment of the evaluation dose curve. Here we first introduce the concept of signed-gamma index $\tilde{\gamma}$, such that its magnitude is the radius for a circle centered at the reference point on the reference dose and tangent to the evaluation dose curve, but its sign is positive if the center of the circle is below the evaluation dose curve (e.g. Figure 2.3(a)) and negative if the center is above the curve (e.g. Figure 2.3(b)). Since the number of particles in the MC simulation is usually very large to ensure a small uncertainty level of clinical relevance; and with the large number of particles, the dose to a voxel in an MC simulation is commonly considered following a Gaussian distribution (Sempau and Bielajew, 2000). In this study, we assume that probability density function $p(t)$ is symmetric around zero. Note that $\tilde{\gamma} = \gamma_0 - t\cos\theta$ where θ is the angle between γ_0 and vertical axis, it is straightforward that

$$\gamma_0 = \int_{-\infty}^{+\infty} dt\, \tilde{\gamma}(t)\, p(t), \tag{2.2}$$

For the average gamma index,

$$\bar{\gamma} = \int_{-\infty}^{+\infty} dt\, |\tilde{\gamma}(t)|\, p(t) = \int_{-\infty}^{\frac{\gamma_0}{\cos\theta}} dt\, \tilde{\gamma}(t)\, p(t) + \int_{\frac{\gamma_0}{\cos\theta}}^{+\infty} dt\, [-\tilde{\gamma}(t)]\, p(t). \tag{2.3}$$

Now, subtracting Equations 2.2 and 2.3 leads to

$$\bar{\gamma} - \gamma_0 = 2\int_{\frac{\gamma_0}{\cos\theta}}^{+\infty} dt\,[-\tilde{\gamma}(t)]\,p(t) \tag{2.4}$$

Since $\tilde{\gamma}(t) < 0$ when $t > \frac{\gamma_0}{\cos\theta}$, we can conclude that

$$\bar{\gamma} \geq \gamma_0. \tag{2.5}$$

This conclusion is valid for a general symmetric probability density function $p(t)$. It has also been theorized that the statistical fluctuations of the dose distribution in an MC calculation, termed as “noise” from here on, follow a Gaussian distribution (Sempau and Bielajew, 2000). So in this case, the average gamma index is then specified to be

$$\bar{\gamma} = \frac{1}{\sqrt{2\pi}\sigma_t}\int_{-\infty}^{+\infty} dt\,|\tilde{\gamma}(t)|\,e^{-t^2/2\sigma_t^2}, \tag{2.6}$$

where σ_t is statistical uncertainty value on the reference point. Then the Equation 2.6 can be rewritten as

$$\bar{\gamma} = \frac{1}{\sqrt{2\pi}\sigma_t}\int_{-\infty}^{\frac{\gamma_0}{\cos\theta}} \mathrm{d}t\,(\gamma_0 - t\cos\theta)e^{-t^2/2\sigma_t^2}$$

$$+\frac{1}{\sqrt{2\pi}\sigma_t}\int_{\frac{\gamma_0}{\cos\theta}}^{+\infty} \mathrm{d}t\,(t\cos\theta - \gamma_0)e^{-t^2/2\sigma_t^2} \tag{2.7}$$

$$= \gamma_0\,\mathrm{erf}\left(\frac{\gamma_0}{\sqrt{2}\sigma_t\cos\theta}\right) + \frac{2}{\sqrt{2\pi}}\sigma_t\cos\theta\,\exp\left(\frac{-\gamma_0^2}{2\cos^2\theta\sigma_t^2}\right). \tag{2.8}$$

The derivative of Equation 2.8 with respect to σ_t is

$$\frac{d\bar{\gamma}}{d\sigma_t} = \sqrt{\frac{2}{\pi}}\cos\theta\,\exp\left(\frac{-\gamma_0^2}{2\cos^2\theta\sigma_t^2}\right). \tag{2.9}$$

Since $\frac{d\bar{\gamma}}{d\sigma_t} > 0$, and when $\sigma_t \to 0$, $\bar{\gamma} \to \gamma_0$, we get the same conclusion as Equation 2.5.

The increase of the average γ-index $\overline{\gamma}$ can be understood as following. When there is a finite deviation t, there are two scenarios resulting different impacts on the average γ-index. First, when t is small for the original γ-index γ_0, i.e. $t \leq \frac{\gamma_0}{\cos\theta}$, the average of the γ-index pair $|\tilde{\gamma}(t)|$ and $|\tilde{\gamma}(-t)|$ equals γ_0. Second, when t is large, i.e. $t > \frac{\gamma_0}{\cos\theta}$, the average of the pair $|\tilde{\gamma}(t)|$ and $|\tilde{\gamma}(-t)|$ is larger than γ_0 due to the flipped sign in one of them caused by the absolute value operation. It is the latter scenario that causes the increase of $\overline{\gamma}$. Hence when the original γ-index value is relatively large for the noise standard deviation, the increase of the average γ-index $\overline{\gamma}$ will be relatively small due to the small contributions from the second scenario.

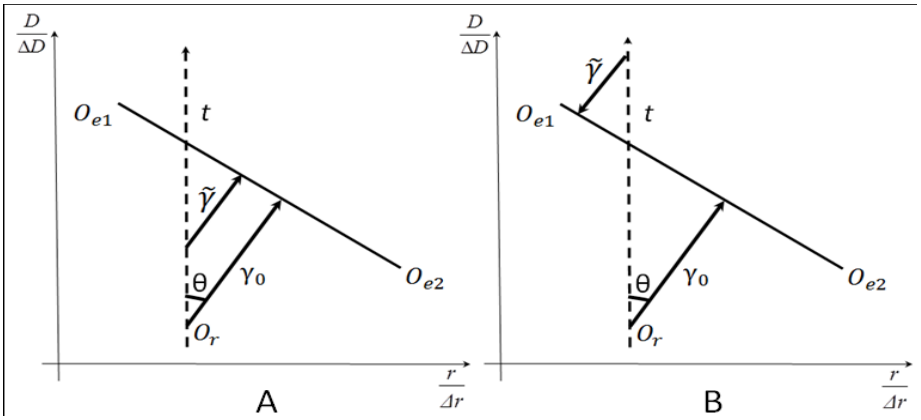

Figure 2.3: (A) and (B) Illustrations of two different contexts where noise is present in the reference dose.

2.3.3.2 MC Statistical Fluctuations in Evaluation Dose

In Figures 2.4(a) and (b), suppose without noises, $O_{e1}O_{e2}$ is the line segment of the evaluation dose curve. With the MC noises, the line $O_{e1}O_{e2}$

moves. As in the last section, similarly we assume in this simplified model, the new γ-index value is only related to the line segment $O_{e1}O_{e2}$ of the evaluation dose curve, not to the other line segment of the evaluation dose curve. σ_{t1}, σ_{t2} are the statistical uncertainties on the dose values at the points O_{e1} and O_{e2}, the average γ-index value $\overline{\gamma}$ can be calculated as,

$$\overline{\gamma} = \int_{-\infty}^{+\infty} dt_1 \int_{-\infty}^{+\infty} dt_2 \, |\tilde{\gamma}(t_1, t_2)| p(t_1, t_2), \tag{2.10}$$

where t_i, $i = 1, 2$, parameterizes the deviation of dose values at the two points O_{e1} and O_{e2} and $p(t_1, t_2)$ is the probability density function. For some noise realizations, the signed-gamma index $\tilde{\gamma}$ may change its sign from positive to negative. For instance, in Figure 2.4(a) when both t_1 and t_2 are large negative values. However, the probability of this situation is relatively small, given that σ_{ti} are small for γ_0. Hence, we first ignore the contributions of γ-indices from these situations. The consequence when this contribution cannot be ignored will be discussed later. Given this assumption, all $\tilde{\gamma}$ are positive regardless of the values of t_i.

As for the probability distribution, for the large number of particles simulated in an MC dose calculation, we assume that $p(t_1, t_2) = p(-t_1, -t_2)$. When the noises at two points $\mathrm{O}_{\mathrm{e}1}$ and $\mathrm{O}_{\mathrm{e}2}$ are statistically independent, this assumption is apparently valid, as the noise distribution at each point is symmetric about zero. In reality, there exist correlations of noises between these two points. This correlation is caused by an electron track that passes through the two voxels. In one MC simulation, the number of electron tracks simultaneously passing the two voxels fluctuates about its average, and the probability of having more tracks is equal to that of having less tracks. Hence our assumption is still valid. Under this assumption, we can rewrite Equation 2.10 as

$$\overline{\gamma} = \frac{1}{2}\int_{-\infty}^{+\infty} \mathrm{d}t_1 \int_{-\infty}^{+\infty} \mathrm{d}t_2[\,\tilde{\gamma}(t_1, t_2) + \tilde{\gamma}(-t_1, -t_2)]\, p(t_1, t_2). \tag{2.11}$$

From Figure 2.4(c), we further separate the integral domain into four different quadrants,

$$\overline{\gamma} = \frac{1}{2}\sum_{i=1}^{4} \iint_{\mathrm{I}_i} \mathrm{d}t_1\, \mathrm{d}t_2[\tilde{\gamma}(t_1, t_2) + \tilde{\gamma}(-t_1, -t_2)]\, p(t_1, t_2). \tag{2.12}$$

Since the integrals in the domain I_1 and I_2 equal to those in the domain I_3 and I_4, respectively, Equation 2.12 reduces to

$$\overline{\gamma} = \sum_{i=1}^{2} \iint_{\mathrm{I}_i} \mathrm{d}t_1\, \mathrm{d}t_2[\tilde{\gamma}(t_1, t_2) + \tilde{\gamma}(-t_1, -t_2)]\, p(t_1, t_2)\ . \tag{2.13}$$

Figure 2.4(a) illustrates the context when t_1 and t_2 are both positive (in domain I_1). Suppose $O_{e1}^{'}\,O_{e2}^{'}$ and $\widetilde{O_{e1}}\widetilde{O_{e2}}$ are the new evaluation dose lines, such that $O_{e1}\widetilde{O_{e1}}$ and $O_{e1}O_{e1}^{'}$ are of the same length, similarly $O_{e2}\widetilde{O_{e2}}$ and $O_{e2}O_{e2}^{'}$ are of the same length, and $\tilde{\gamma}(t_1, t_2)$ is represented as O_rD while $\tilde{\gamma}(-t_1, -t_2)$ is O_rA. O_rB is the original γ-index γ_0. If we set CF ⊥ $O_{e1}^{'}\,O_{e2}^{'}$, we have

$$O_rA + O_rD \leq O_rA + O_rC + CF. \tag{2.14}$$

Since $O_rA = O_rE \cdot \cos(\angle EO_rA)$ and $CF = CE \cdot \cos(\angle EO_rA)$, combining with Equation 2.14, we can get

$$O_rA + O_rD \leq O_rC \cdot [1 + \cos(\angle EO_rA)]. \tag{2.15}$$

Moreover $O_rB = O_rC \cdot \cos(\angle EO_rB)$. From the geometric relationship, we also have $\angle EO_rA = 180° - 2\alpha - 2\theta$ and $\angle EO_rB = 90° - \alpha - \theta$. Hence,

$$O_rA + O_rD \leq O_rC \cdot 2\cos^2(\angle EO_rB) \leq 2 \cdot O_rB. \tag{2.16}$$

This indicates that

$$\iint_{\mathrm{I}_1} \mathrm{d}t_1\, \mathrm{d}t_2 [\,\tilde{\gamma}(t_1, t_2) + \tilde{\gamma}(-t_1, -t_2)]\, p(t_1, t_2) \leq 2\, \gamma_0 \iint_{\mathrm{I}_1} p(t_1, t_2)\, \mathrm{d}t_1\, \mathrm{d}t_2. \tag{2.17}$$

Similarly, Figure 2.4(b) illustrates a context where t_1 is negative and t_2 is positive (in domain I_2). $\tilde{\gamma}(t_1, t_2)$ is represented as O_rD while $\tilde{\gamma}(-t_1, -t_2)$ is O_rA. O_rB is the original γ-index γ_0. With a similar derivation, we can generate the same conclusion as Equation 2.17.

$$\iint_{\mathrm{I}_2} \mathrm{d}t_1\, \mathrm{d}t_2 [\,\tilde{\gamma}(t_1, t_2) + \tilde{\gamma}(-t_1, -t_2)]\, p(t_1, t_2) \leq \gamma_0 \iint_{\mathrm{I}_2} p(t_1, t_2)\, \mathrm{d}t_1\, \mathrm{d}t_2. \tag{2.18}$$

Combine Equation 2.13, 2.17 and 2.18, we then have

$$\bar{\gamma} \leq 2\, \gamma_0 \left[\sum_{i=1}^{2} \iint_{\mathrm{I}_i} p(t_1, t_2)\, \mathrm{d}t_1\, \mathrm{d}t_2\right]. \tag{2.19}$$

Since $2\sum_{i=1}^{2} \iint_{\mathrm{I}_i} p(t_1, t_2)\, \mathrm{d}t_1\, \mathrm{d}t_2 = 1$, we can conclude that

$$\bar{\gamma} \leq \gamma_0. \tag{2.20}$$

This indicates that the presence of noise will lead to an underestimation of the γ-index value. It is important to note that when the probability for negative signed γ-index $\tilde{\gamma}(t_1, t_2)$ is not negligible, i.e. when the noise standard deviation is relatively large for the original γ-index value, Equation 2.20 is no longer valid. The simplest case is when the reference dose distribution is the same as the evaluation dose and γ-index values are all zero. In this case, the MC noise in the evaluation dose distribution leads to an overestimation of γ-index values. However, as later shown in our numerical experiments, this situation is not clinically relevant because it only happens when the original γ-index values are very small and their variation due to the MC noise does not affect the γ-index passing rate.

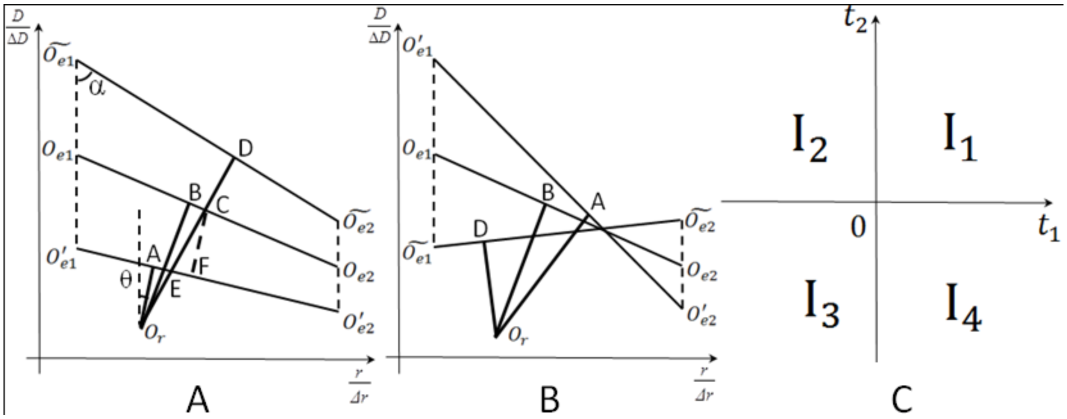

Figure 2.4: (A) and (B) Illustrations of two different contexts where noise is present in the evaluation dose. (C) Split of the integration domain for Equation 2.11.

2.3.4 Numerical experiments

To validate the theoretical model, we conducted numerical experiments on two realistic clinical cases: a 7-beam IMRT prostate plan and a 2-arc VMAT HN plan. To study the effect of using an MC dose as the reference dose or the evaluation dose in γ-index tests, a non-MC dose distribution and a set of MC dose distributions at various σ levels (including zero σ level) are required for each clinical case. For the non-MC dose, we used the dose distribution in the patient plan extracted from a commercial TPS (Eclipse, Varian Medical Inc., Palo Alto, CA) which was computed using the Analytical Anisotropic Algorithm (AAA). The resulting dose from the Eclipse system is at a resolution of 2.5×2.5×2.5mm^3 and interpolated to the MC dose resolution of 1.953×1.953×2.5mm^3. The AAA algorithm is an analytical algorithm hence there is no noise in the dose. To get the set of MC dose distributions, we first extracted the MLC leaf sequences of all beam angles from the patient plan. Using different number of particle histories in the simulation, the dose distributions of various σ level were calculated on the patient geometry using the GPU based MC dose engine, gDPM. We define the term σ *level* as the average σ value normalized to the maximum dose D_{max} within regions of dose values higher than 50% of D_{max} (VOI$_{50\%}$). The dose distributions with σ level of 0.5%, 1%, 1.5%, and 2% were calculated, which are the most clinically relevant noise levels for MC dose calculations. An additional dose distribution of σ level of 0.2% was also computed and a de-noising technique was performed across the special domain so that de-noised dose was considered to be the MC dose with zero noise level. The details of this denoising technique is presented later.

We would like to point out that the beam parameters in the gDPM code were not purposely tuned to match the Eclipse results. To analyze the situation when both the evaluation and reference doses are generated by the MC method, another set of MC dose distributions at various σ levels (including zero σ level) is desired. For this set of MC doses, we used the same MC dose engine gDPM, but shifted the isocenter position of all beams by 3mm to the patient's left, posterior, and superior directions, respectively, to simulate the dosimetric effects due to a set up error in a clinical situation.

To study the impact of the MC noise on the γ-index value, we first needed to conduct a base comparison between the non-MC dose and the MC dose with zero σ level; the resulting γ-index values of a selected group of voxels are treated as the base values. Then the γ-index results for the same voxels were followed when the non-MC dose is compared with the MC doses of increasing σ levels. These voxels are selected as the ones with more clinical relevance. Since the passing rate within a region of interest (ROI) is the most common criteria used to compare two dose distributions, we focused on a range of γ-index values that contribute to the calculation of the gamma passing rate. We also noticed that the behavior of average γ-index variation due to the MC noise is similar for close γ-index values. Thus, based on the base comparison, we selected four groups of voxels in the reference dose distribution with γ-index values from value 0.6 to 0.8 (0.6, 0.8), from value 0.8 to 1 (0.8, 1.0), from value 1 to 1.2 (1.0, 1.2), and from value 1.2 to 1.4 (1.2, 1.4). For each group of voxels, we followed the variation of the average γ-index value with the increase of the σ level in the MC dose distribution. Furthermore, the γ-index passing rates were also reported for each comparison between the non-MC dose and the MC dose. In this study, in addition to VOI$_{50\%}$, we also selected another ROI where dose values were higher than 10% of D_{max} (VOI$_{10\%}$).

Since the MC noise is a random variable, for the comparison at each σ level, we repeated the γ-index test ten times for ten different random realizations of the dose distributions to get the mean of the γ-index test results. And during our experiments, all dose distribution comparisons were performed using the GPU based fast γ-index algorithm, gGamma.

2.3.5 Experiment Results

2.3.5.1 MC reference dose vs Non-MC evaluation doses

To study the effect of using an MC dose as the reference dose in γ-index tests, we treated the set of MC doses as the reference doses and the non-MC dose as the evaluation dose. Figures 2.5 (A) and (B) show the average γ-index values of voxels whose original γ-indices fall within the range of (0.6, 0.8), (0.8, 1.0), (1.0, 1.2) and (1.2, 1.4) as functions of the σ level in the reference dose ($\overline{\sigma_{ref}}$) for both prostate and HN cases. For Figures 2.5(A) and (B), we used the most common clinical γ-index test criterion: 3%-3mm. We can see that the average γ-index value within each group slightly increases with $\overline{\sigma_{ref}}$. Figures 2.5 (C) and (D) show the passing rate within VOI$_{50\%}$ and VOI$_{10\%}$ as function of $\overline{\sigma_{ref}}$ for two different γ-index test criteria: 3%-3mm and 2%-2mm. It is noted that, although the average γ-index value does not change much, the gamma passing rate decreases significantly with the increase of the σ levels in the reference dose, especially for $\mathrm{VOI}_{50\%}$ for these two clinical cases.

To better understand the effect of the MC noise on the gamma passing rate, we examined the voxels that contribute to the gamma passing rate calculation. We defined *Type-I voxels* as those with γ-index values larger than one in the base comparison when the MC σ level is zero and γ-index values smaller than or equal to one when the MC σ level is 2%. *Type-II voxels* are those with the opposite situation, *i.e.*, γ-index values increasing from below or equal to one to above one when the σ level increases from zero and 2%. Since the MC noise is a random variable, for a γ-index test with a random realization of the MC dose distribution, a particular voxel with the γ-index value around one can be either Type-I or Type-II. However, when running the γ-index test for many random realizations of the MC dose distributions, this voxel will have more chance to be Type-II than Type-I when using the MC dose as the reference dose. Table 2.1 summarizes the average percentages of Type-I and Type-II voxels within two ROIs for two comparison criteria after running the γ-index test for 10 different random realizations of the MC reference dose distributions. It is noted that percentage of Type-II voxels is higher than that of Type-I. The net effect, Type-II percentage minus the Type-I percentage, is equal to the change of the gamma passing rate with the MC dose of 2% σ level, as shown in Figures 2.5 (C) and (D).

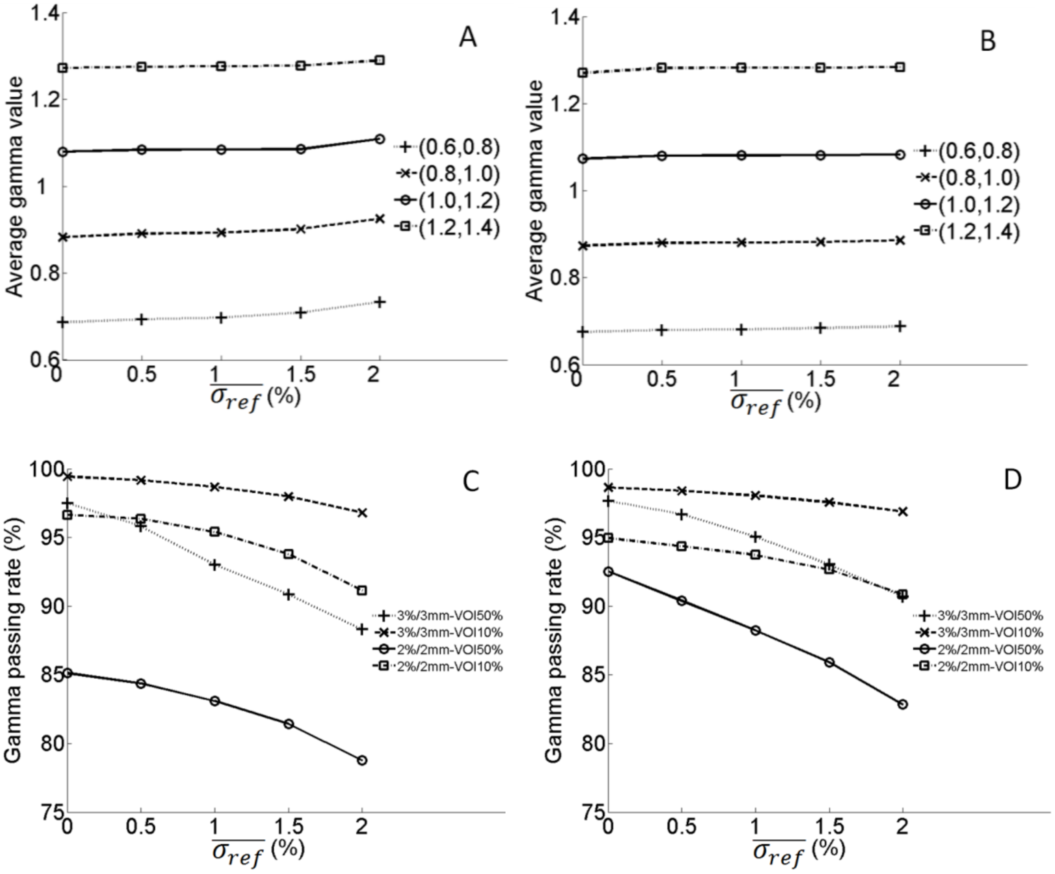

Figure 2.5: Average γ-index and gamma passing rate as functions of σ level in the reference dose for MC reference doses vs non-MC evaluation dose. (A) and (C) Prostate case. (B) and (D) HN case.

Table 2.1: Percentages of Type-I and Type-II voxels within $VOI_{50\%}$ and $VOI_{10\%}$ for MC reference doses of 2% σ level vs the non-MC evaluation dose with 3%-3mm and 2%-2mm criteria.

Clinical case	Prostate				HN			
Criteria	3%-3mm		2%-2mm		3%-3mm		2%-2mm	
ROI	$VOI_{50\%}$	$VOI_{10\%}$	$VOI_{50\%}$	$VOI_{10\%}$	$VOI_{50\%}$	$VOI_{10\%}$	$VOI_{50\%}$	$VOI_{10\%}$
Type-I Voxels (%)	1.09	0.23	5.92	1.19	0.33	0.30	2.24	1.04
Type-II Voxels (%)	10.31	2.87	12.27	6.70	7.31	2.04	11.93	5.14
Type-II – Type-I (%)	9.22	2.64	6.35	5.51	6.98	1.74	9.69	4.10

2.3.5.2 Non-MC reference dose vs MC evaluation doses

To study the effect of MC noise in the evaluation dose in γ-index tests, we treated the non-MC dose as the reference dose and the set of MC doses as the evaluation doses. Figures 2.6 (A) and (B) show the average γ-index values of voxels whose original γ-indices fall within each range as functions of the σ level in the evaluation dose ($\overline{\sigma_{eva}}$) for prostate and HN cases. The average γ-index value within each group decreases dramatically with $\overline{\sigma_{eva}}$. Figures 2.6 (C) and (D) show, for two different γ-index test criteria, 3%-3mm and 2%-2mm, the passing rate within $\mathrm{VOI}_{50\%}$ and $\mathrm{VOI}_{10\%}$ as function of $\overline{\sigma_{eva}}$. We observed that, the gamma passing rates saturated for 3%-3mm criterion, while the gamma passing rates for 2%-2mm criterion increases with the increase of $\overline{\sigma_{eva}}$, especially for $\mathrm{VOI}_{50\%}$. Table 2.2 summarizes the average percentage of Type-I or Type-II voxels within the ROIs. For the non-MC reference dose vs the MC evaluation dose of 2% σ level, the percentage of Type-I voxels is higher than that of Type-II which means that, statistically, there are more voxels where the γ-index value sinks below one than voxels where the γ-index value rises above one. The net difference between Type-I percentage and Type–II percentage, is the same as the change of the gamma passing rate with the MC dose of 2% σ level, shown in Figures 2.6 (C) and (D).

In Section 2.3.3.2, we have noticed that, when the statistical standard deviation in the MC evaluation dose distribution is relatively large for the original γ-index value, the γ-index value will be overestimated on average due to the noise. Figures 2.7 (A) and (B) show the average γ-index value of voxels with small original γ-index values, ranging from 0.1 to 0.24, as functions of $\overline{\sigma_{eva}}$ for the prostate and HN cases. From Figure 2.7 we can see that when the original γ-index value is large enough, i.e. larger than 0.2, the average γ-index decreases with $\overline{\sigma_{eva}}$ (shown in blue and dashed lines); however, when the original γ-index value is very small, i.e. smaller than 0.14, the average γ-index increases with $\overline{\sigma_{eva}}$ (shown in green and dotted lines). For the in-between original γ-index value, the average γ-index first decreases and then increases with $\overline{\sigma_{eva}}$ (shown in red and dashed/dotted lines). We would like to point out that voxels with this range of original γ-index values do not contribute to the passing rate change.

Table 2.2: Percentages of Type-I and Type-II voxels within $VOI_{50\%}$ and $VOI_{10\%}$ for the non-MC reference dose vs MC evaluation doses of 2% σ level with 3%-3mm and 2%-2mm criteria.

Clinical case	Prostate				HN			
Criteria	3%-3mm		2%-2mm		3%-3mm		2%-2mm	
ROI	$VOI_{50\%}$	$VOI_{10\%}$	$VOI_{50\%}$	$VOI_{10\%}$	$VOI_{50\%}$	$VOI_{10\%}$	$VOI_{50\%}$	$VOI_{10\%}$
Type-I Voxels (%)	0.50	0.09	7.20	1.22	0.510	0.097	3.63	1.06
Type-II Voxels (%)	0.02	0.01	0.48	0.20	0.004	0.003	0.38	0.16
Type-I – Type-II (%)	0.48	0.08	6.72	1.02	0.506	0.094	3.25	0.90

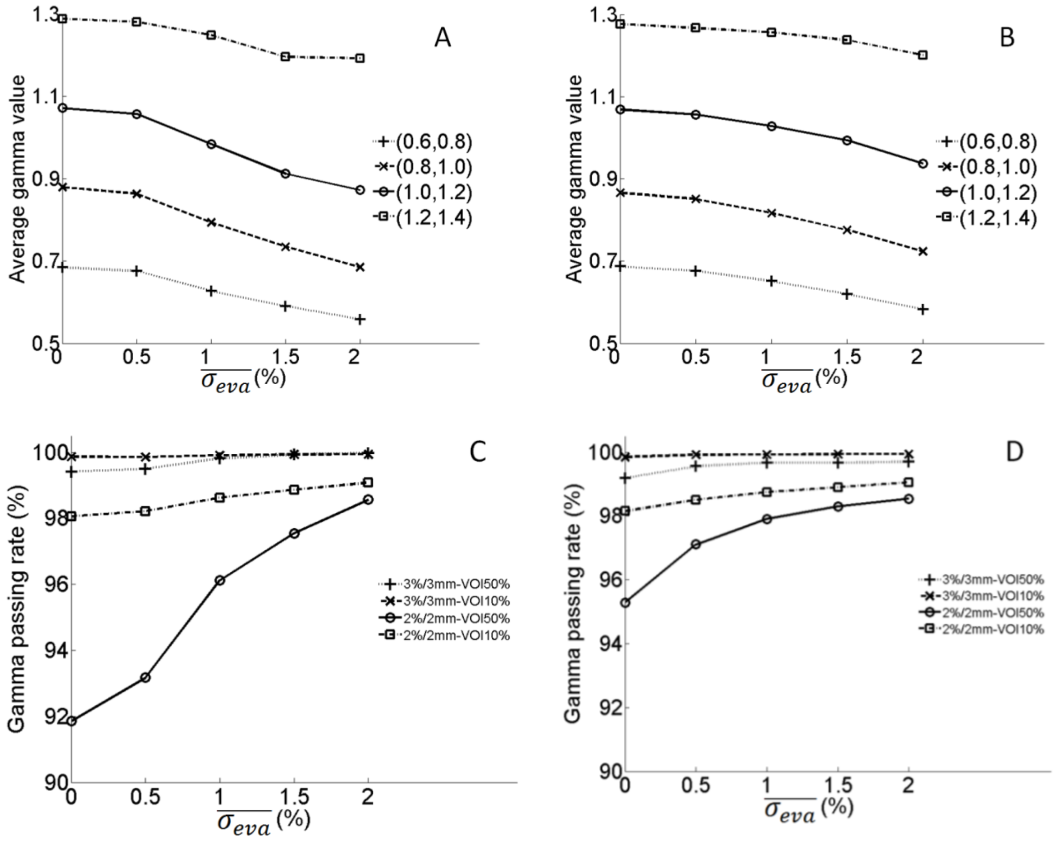

Figure 2.6: Average γ-index and gamma passing rate as functions of σ level in the evaluation dose for non-MC reference dose vs MC evaluation doses. (A) and (C) Prostate case. (B) and (D) HN case.

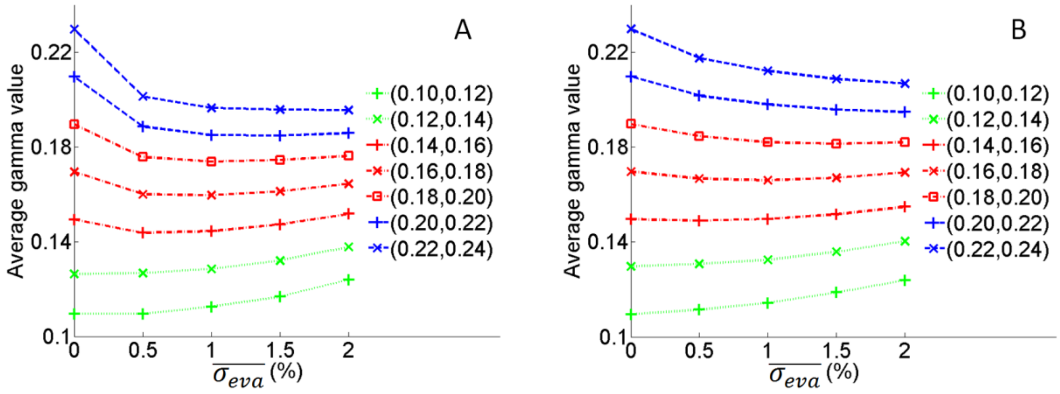

Figure 2.7: Average γ-index as functions of σ level in evaluation dose for non-MC reference dose vs MC evaluation doses. (A) Prostate case. (B) HN case.

2.3.5.3 MC reference dose vs MC evaluation dose

To analyze the situation when both the evaluation and reference doses are generated by the MC method, we considered the set of MC doses as the reference doses and the other set of MC doses with the shifted isocenter as the evaluation doses. Figure 2.8 shows the color maps of the gamma passing rate in high dose region $\mathrm{VOI}_{50\%}$ under 3%-3mm criterion. The x-axis is the σ level in the evaluation dose, while the y-axis is the σ level in the reference dose. The values at origin of the two maps are the base value with zero σ level in both reference and evaluation doses. Along the x-axis, the results correspond to the cases for the non-MC reference dose versus MC evaluation doses, same as in Figures 2.6 (C) and (D). Along the y-axis, the results correspond to the cases for MC reference doses versus the non-MC evaluation dose, same as in Figures 2.5 (C) and (D). The black lines in Figure 2.8 illustrate iso-value lines on which the passing rate is the same as the base value for MC doses of zero σ level. The iso-value line splits the map into two regions: the upper-left region, where the MC noise level is relatively high in the reference dose leading to the underestimation of the gamma passing rate, and the lower-right region, where the MC noise level is relatively high in the evaluation dose leading to the overestimation of the gamma passing rate. The shape of iso-value line and the way that it splits the map are case-dependent. When both doses are the MC doses, we redefine *Type-I voxels* as those with γ-index values larger than one when the σ level is zero in both the evaluation and the reference doses and less than or equal to one when the σ level is 2% in both doses; *Type-II voxels* are those with the opposite situation, *i.e.*, γ-index values increasing from below or equal to one to above one when both σ levels increase from zero and 2%. From Table 2.3, the average percentage of Type-I is higher than the percentage of Type-II voxels and the net contribution matches with the increased gamma passing rate in the right upper corner with 2% σ level in both reference and evaluation doses.

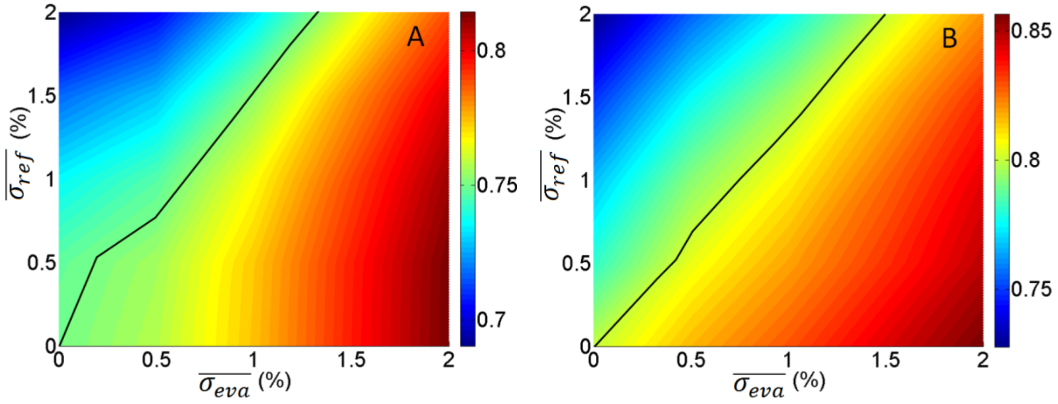

Figure 2.8: The color maps of gamma passing rate within VOI50% as functions of σ level in the reference and evaluation doses for MC reference dose vs MC evaluation dose with 3%-3mm criterion. (A) Prostate case. (B) HN case.

Table 2.3: Percentages of Type-I and Type-II voxels within VOI50% for the MC reference dose of 2% $\boldsymbol{\sigma}$ level vs the MC evaluation dose of 2% σ level with 3%-3mm criterion.

Clinical case	Type-I Voxels (%)	Type-II Voxels (%)	Type-I – Type-II (%)
Prostate	7.80	3.91	3.89
HN	6.54	4.39	2.15

2.3.6 Discussion and Conclusion

In this section, we have first demonstrated in a simplified 1D model that, to the first order approximation, MC statistical fluctuation in the reference dose tends to overestimate the γ-index, while that in the evaluation dose tends to underestimate the γ-index when the original γ-index value is relatively large. To validate the theoretical conclusions, we conducted numerical experiments on two clinical cases: an IMRT prostate case and a VMAT HN case. We focused on voxels with clinically relevant γ-index values in the absence of noise, range of 0.6 to 1.4, and found that when performing γ-index tests between an MC reference dose and a non-MC evaluation dose, the average γ-index is overestimated but the change is not significant. Second, when performing γ-index tests between a non-MC reference dose and an MC evaluation dose, the average γ-index is underestimated and decreases with the increase of noise level in the evaluation dose. This is doubly confirmed by the blue dashed curves in the Figure 2.7. When the original γ-index value γ_0 is larger than 0.2, the average γ-index monotonically decreases with the increase of the noise level. For the green dotted curves in the Figure 2.7, when the γ_0 is smaller than 0.14, the average γ-index increases with the noise level. For those cases with γ_0 lying in between the above two limits, the average γ-index first decreases when the noise level is low and then increases. Nonetheless, in the latter two situations, the changes of γ-index values due to the MC noise are not expected to considerably impact the gamma passing rates, since the small original γ-index values are much smaller than one. Hence these two situations are not clinically relevant.

The change for the gamma passing rate within the ROI due to the MC noise is most relevant for the clinical applications of γ-index test. In the experiment, we defined two quantities, percentage of Type-I voxels and percentage of Type-II voxels and we found the following. (1) When performing γ-index test between an MC reference dose and a non-MC evaluation dose, the gamma passing rate decreases with the increase of the statistical noise level in the reference dose. (2) When performing γ-index test between a non-MC reference dose and an MC evaluation dose, the gamma passing rate increases with the increase of the noise level in the evaluation dose. In these two situations, the magnitude of the change of gamma passing rate when 2% σ level exists in the MC dose equals to the difference between the percentage of Type-I and that of Type-II voxels. (3) When the reference dose and the evaluation dose are both MC doses, the gamma passing rate increases when the statistical noise in the evaluation dose increases. It decreases when the statistical noise in the reference dose increases. Considering again the correlation between the neighboring voxels in the MC evaluation dose, this effect on the γ-index is usually local in the spatial domain. However, since the gamma passing rate is a statistical overall effect from all the voxels within the ROI, the local effect will be smeared out in the whole ROI.

For the two clinical cases we have tested, the effect on the gamma passing rate is quite significant. Taking the 3%-3mm test criterion as an example, when there exists 2% MC σ level in the reference dose, the gamma passing rate in $\mathrm{VOI}_{50\%}$ drops from 97.5% to 88.3% and in $\mathrm{VOI}_{10\%}$ from 99.4% to 96.8% for the prostate case. For the HN case, the gamma passing rate in $\mathrm{VOI}_{50\%}$ drops from 97.7% to 90.7% and in $\mathrm{VOI}_{10\%}$ from 98.6% to 96.9%, respectively. On the other hand, when 2% MC noise level exists in the evaluation dose, the resulting increase of the gamma passing rate is not significant under the 3%-3mm criterion. This is because the passing rate is already very close to one in the absence of noise for this relatively loose criterion. However, the changes are more obvious under 2%-2mm criterion. Especially in $\mathrm{VOI}_{50\%}$, it increases from 91.9% to 98.6% for the prostate case and from 95.3% to 98.5% for the HN case. Based on our theoretical and numerical results, we conclude that great caution is needed when dealing with MC doses in γ-index tests. The MC statistical fluctuation effect should be considered when analyzing the γ-index test results to avoid biased conclusions.

2.4 Denoising for Monte Carlo Based Dose

2.4.1 Overview of Monte Carlo Based Dose Denoising

Besides the effects of statistical uncertainty in MC based dose calculations on γ-index evaluation tests studied in the last section, the impacts of noise on other treatment plan evaluation criteria have also been examined (Keall *et al.*, 2000; Buffa and Nahum, 2000). These studies indicate that it is necessary to reduce the MC noise to a certain level to avoid any bias when MC calculated doses are involved. A simple way to reduce the statistical fluctuations in MC based dose calculation is by performing the MC simulation with a very large number of particle histories. Yet, this is generally impractical in routine clinics due to the long computation time especially before the advancements of fast MC algorithms.

Another possibility is to post process the MC based dose by removing or reducing the statistical uncertainty using a smoothing or denoising algorithm. A powerful denoising algorithm estimates the true dose distribution based on MC simulation results with reduced number of particle histories. It hence improves the computational efficiency. In the past, many research groups have been devoted to develop denoising methods. Such methods include image digital filtering (Deasy, 2000), wavelet thresholding (Deasy *et al.*, 2002), adaptive anisotropic diffusion (Miao *et al.*, 2003), content adaptive median hybrid filtering (El Naqa *et al.*, 2003) and denoising based on an optimization problem (Fippel and Nusslin, 2003; Le *et al.*, 2007a).

The denoising algorithms are typically well suited for the GPU architecture, because the voxels data can be divided into different GPU threads and the executions can be conducted at the same time. To our knowledge, however, no work has been done to develop a denoising algorithm for MC based dose distributions on GPUs. In light of this, as well as the needs of reducing MC noise in the calculated dose distributions to avoid bias in dose evaluations, we have also developed a denoising module in our computational QA tool. In addition to the GPU implementation, a novel model taking into consideration the noise property is also invented.

2.4.2 Denoising Algorithm

It has been well known that the noise signal $\widehat{D}\,(\boldsymbol{v})$ at a voxel in a MC based dose distribution follows a Poisson distribution. With this knowledge, we propose to estimate the true dose value $D(\boldsymbol{v})$ by solving an optimization problem

$$\begin{aligned} D(\boldsymbol{v}) &= \mathrm{argmin}_D\, E[D] \\ &= \mathrm{argmin}_D \int d\boldsymbol{v}\,\left(D - \widehat{D}\; logD\right) + \frac{\beta}{2}\int d\boldsymbol{v}\;|\nabla D|^2\,, \mathrm{s.t.}\, D(\boldsymbol{v}) \geq 0. \end{aligned} \tag{2.21}$$

$E[D]$ is the objective function where the first term is a data-fidelity term considering the Poisson noise (Le *et al.*, 2007) and the second term is a penalty term to ensure the smoothness of the de-noised dose $D(\boldsymbol{v})$. β is a parameter to control the relative importance between the two terms.

Since this is a convex objective function with a nonnegative constraint, we employ a well-known gradient projection method (e.g.(Bazaraa *et al.*, 2006)) to solve this problem. At each iteration the new solution is given by

$$D_{k+1} = P\big(D_k - \lambda_k\, \nabla E(D_k)^{\mathrm{T}}\big), \tag{2.22}$$

where P denotes the projection of the dose onto the feasible set and λ_k denotes the step size at iteration k. Specifically, the non-negativity constraint is handled by

$$P\big(D_k - \lambda_k\, \nabla E(D_k)^{\mathrm{T}}\big) = \max(0, D_k - \lambda_k \nabla E(D_k)^{\mathrm{T}}). \tag{2.23}$$

To obtain the step size λ_k, we combine the Barzilar-Borwein method (Barzilai and Borwein, 1988) with the Armijo's line search rule (Armijo, 1966). The line search starts with an initial step size λ_0, which is calculated using the formula from the Barzilar-Borwein method. After updating the solution with this step size using Equation 2.22, if the new objection function is less than a threshold T_k, we will accept this step size and update the solution. Otherwise the step size is decreased by a factor α >1. This process is repeated until the threshold objective function value is met. Since the line search direction is the negative gradient direction, the Armijo's rule gives an expression for the threshold as follows with 0< ε <1:

$$T_k = E(D_k) - \frac{\varepsilon}{\lambda}\,(D_{k+1} - D_k)(D_{k+1} - D_k)^{\mathrm{T}}. \tag{2.24}$$

We iterate this process to minimize the objective function. The iteration process is terminated when the relative decrease of the objective function between two successive steps is less than a user defined value δ,

$$|E(D_k) - E(D_{k+1})|/E(D_k) < \delta, \text{ where } \delta = 10^{-4}. \tag{2.25}$$

The entire algorithm is summarized as following:

```
Initialization: Set initial solution $D_1 = \widehat{D}$ ; Select parameters $\varepsilon, \alpha$.

Main loop:
    1. Set $d_k = \nabla E(D_k)$;
    2. If $k = 1, \lambda = \lambda_0 = \frac{100}{\|\nabla E(D_k)\|}$;
       else
           $s_{k-1} = D_k - D_{k-1}, y_{k-1} = d_k - d_{k-1}$;
           $\lambda = \lambda_0 = \begin{cases} \frac{s_{k-1}{}^{\mathrm{T}} y_{k-1}}{y_{k-1}{}^{\mathrm{T}} y_{k-1}}, \text{k is even} \\ \frac{s_{k-1}{}^{\mathrm{T}} s_{k-1}}{s_{k-1}{}^{\mathrm{T}} y_{k-1}}, \text{k is odd} \end{cases}$;
       End if
       $D_{k+1} = \max(0, D_k - \lambda d_k)$.
    3. If $E(D_{k+1}) < T_k$ , go to step 5; else go to step 4.
    4. $\lambda = \frac{\lambda}{\alpha}$; $D_{k+1} = \max(0, D_k - \lambda d_k)$; go to step 3.
    5. $|E(D_k) - E(D_{k+1})|/E(D_k) < \delta$, stop; else k=k+1, go to step 1.
```

Figure 2.9 illustrates the flow chart of our GPU implementation of this algorithm. The major computations shown in the grey boxes are parallelized on GPU, e.g. objective function evaluation, gradient calculation, and smoothed dose update. Only those simple arithmetic operations shown in the white boxes run on the CPU side. The utilization of GPU greatly enhanced the computational efficiency.

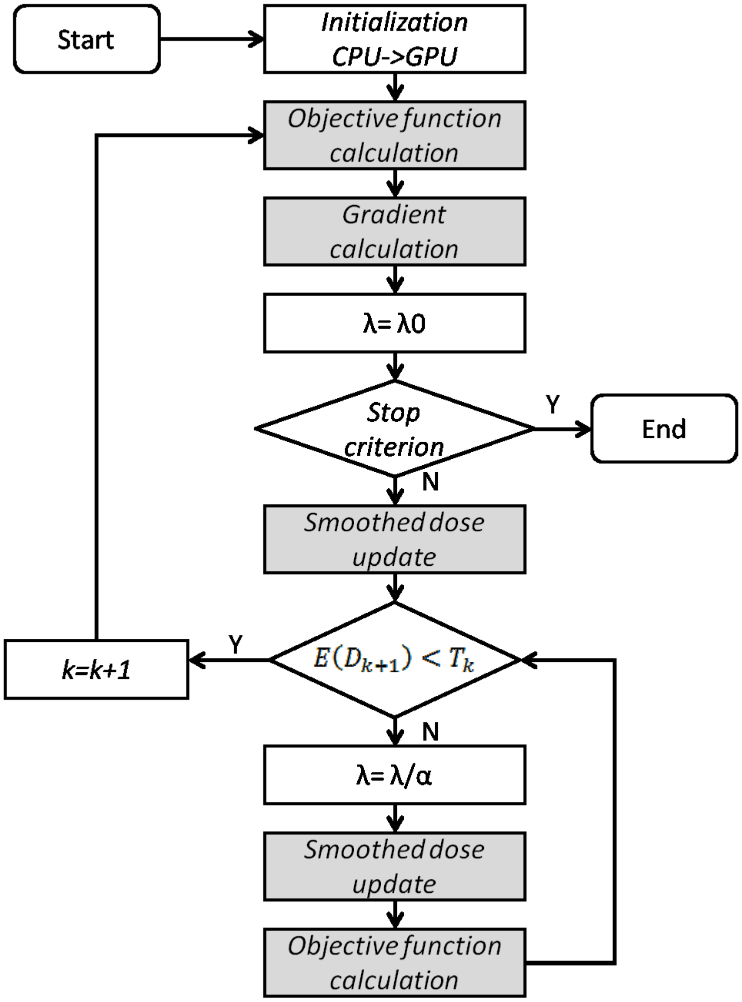

Figure 2.9: Flow chart of our GPU based denoising algorithm. Grey boxes denote CUDA kernels and white boxes denotes C code on CPU.

2.4.3 Numerical Experiments

To verify the accuracy of this denoise algorithm, we conduct numerical experiments using two realistic clinical cases: a 7-beam IMRT prostate plan and a 2-arc VMAT HN plan. For each patient cases, first we simulate the MC dose distribution using the GPU based MC code, gDPM with a very large number of particle histories, such that the σ *level*, defined as average uncertainty value normalized to the maximum dose D_{max} within the 50% isodose line, is less than 0.15%. This dose distribution is considered as the ground truth dose distribution, MC_g. The noisy MC dose, MC_n is obtained by the same MC code, such that the defined σ level is around 2.0%. Then the denoising algorithm is applied to the MC_n to obtain the denoised result, MC_s. Three test criteria, maximum dose difference, root-mean-square difference (RMSD) and the visual inspection of iso-lines and dose profiles, are used to evaluate the denoise algorithm's performance by comparing MC_n and MC_s with the ground truth MC_g, respectively (Kawrakow, 2002). The maximum dose difference ΔD_{max} and the RMSD are reported in a unit of D_{max} of MC_g. The spatial resolution of all MC dose cases is $1.953\times1.953\times2.5\text{mm}^3$.

2.4.4 Experiment Results

Table 2.4 summarizes the values for maximum dose difference ΔD_{max} and RMSD results. For both the prostate and the HN patient cases, a significant decrease on the maximum dose difference and the RMSD is observed in the smoothed dose distribution compared to the noisy dose. Figure 2.10 and Figure 2.11 show the iso-lines for the ground truth, the smoothed and the noisy dose distributions in the central transversal slices of the prostate and the HN patients. Corresponding dose profiles are also plotted. The improvements via the denoising approach is obvious. In particular, the iso-lines and the dose profiles of the denoised dose are almost the same as those of the ground truth dose and no essential information is lost by the denoising process.

The MC simulation time T_g and T_n for $\mathrm{MC_g}$ and $\mathrm{MC_n}$ together with the running time for smoothing process T_{sm} are summarized in Table 2.5. The denoise process takes only a couple of seconds to obtain the smoothed dose distribution. The time $T_n + T_{sm}$ represents the time required to obtain a dose distribution that has very low σ level. Compared to the time T_g necessary to yield a dose with the same level of uncertainty but from full and long MC simulations, the denoising method effectively improves computational efficiency considerably without sacrificing result accuracy.

Table 2.4: Maximum dose difference and RMSD for smoothed dose distributions and doses with 2% σ level compared with ground truth dose distributions.

Patient case	ΔD_{max} $(\% \ D_{max})$		RMSD $(\% \ D_{max})$	
	MC_g vs. MC_n	MC_g vs. MC_s	MC_g vs. MC_n	MC_g vs. MC_s
HN	5.04	0.37	0.37	0.17
Prostate	6.20	1.05	0.46	0.26

Table 2.5: Computational time for simulating ground truth and dose with 2% σ level using gDPM and denoising.

Patient case	Volume size	T_g(sec)	T_n (sec)	T_{sm}(sec)
HN	256×256×186	3224	35.6	2.7
Prostate	256×256×160	2534	27.8	1.8

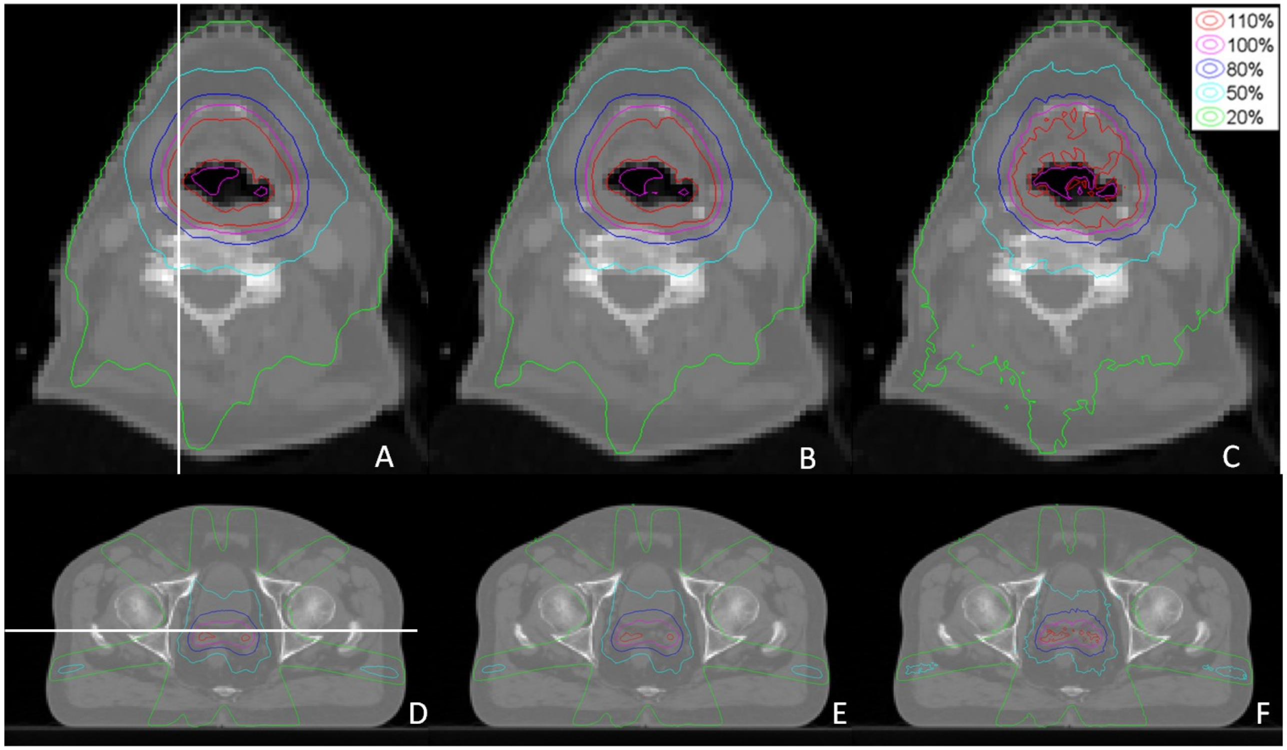

Figure 2.10: Iso-dose lines for prostate (A-C) and HN (D-F) cases in central transversal slice. (A) and (D) Ground truth dose distributions. (B) and (E) Smoothed dose distributions. (C) and (F) Dose distributions with 2% σ level.

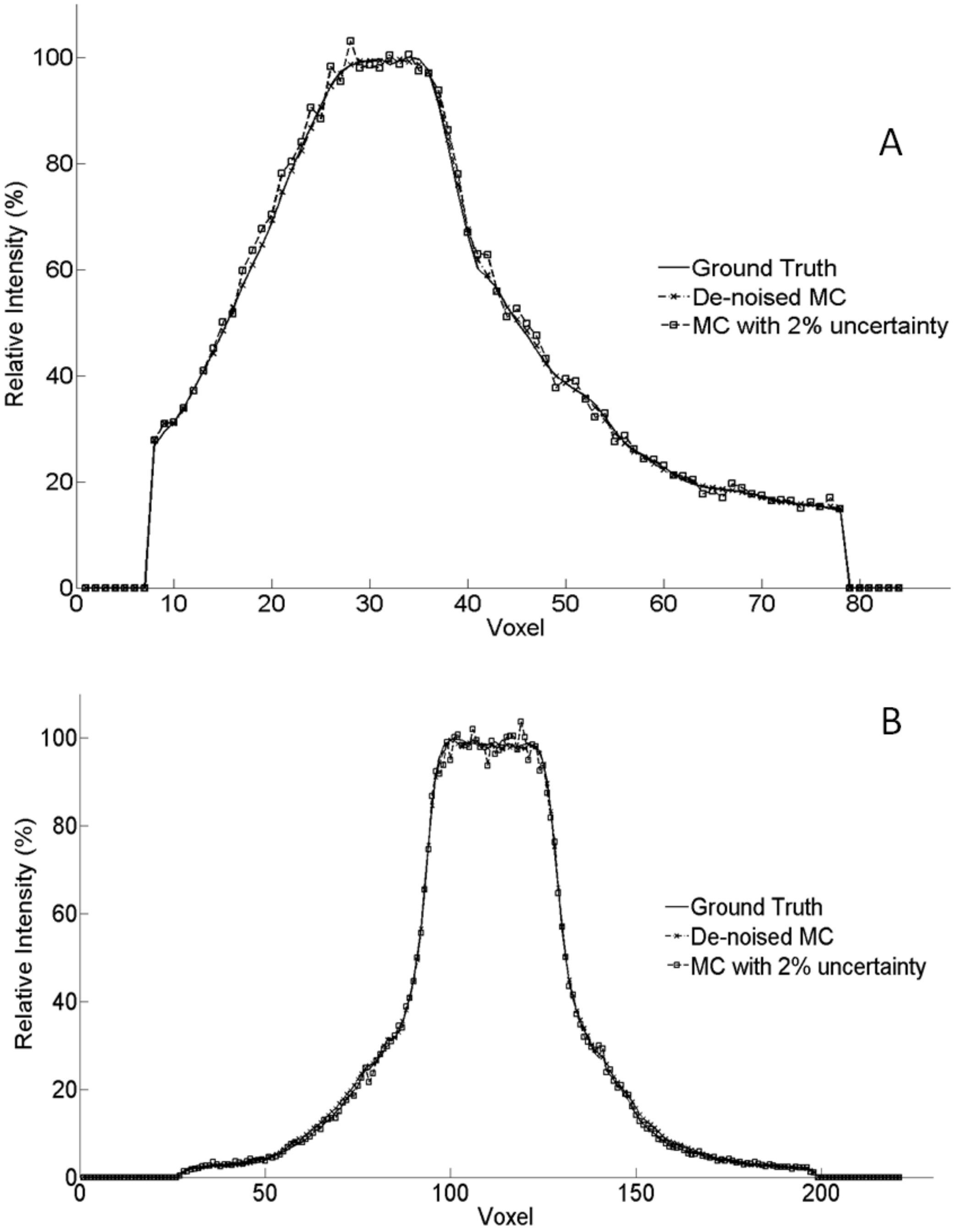

Figure 2.11: Dose profiles. (A) HN case and (B) Prostate case.

2.5 Monte Carlo Source Modeling

Another module necessary for our computational QA tool is source model in a MC simulation. Without an accurate characterization of a LINAC source in a MC dose calculation process, the sampled photon from the LINAC cannot represent the clinical realism and hence the resulting dose accuracy is deteriorated. In this section, we will first briefly discuss dosimetric properties of a clinical photon beam in radiation therapy. Then we will present our researches towards the development of a simple yet practical LINAC source model specifically for the QA purpose.

2.5.1 Dosimetric Properties of Photon Beams

Figure 1.2 illustrates the LINAC beam head components for the production of X-ray with LINAC machines. The major component of the output radiation beam is a source of *primary photon radiation* that is produced directly from the target without any intermediate interactions. Meanwhile, an *extrafocal scattered radiation* is generated by the primary photon interacting with the LINAC head components. In addition, the *contaminating charged particles,* e.g. electrons, are also released in these interactions.

The range of the contaminating charged particles is fairly short, and hence their contribution to the absorbed dose inside a patient is only within the first 1-2cm from the surface. Since a photon beam is primarily used to treat deeply seated tumors, the dose contributions from the contaminating electrons can be safely ignored. Inside a patient, the dose is deposited through photon interacting with the medium. *Primary dose* denotes the dose deposited by the charged particles released from the interactions of the incident primary photon. *Scattered dose* denotes the dose deposited by electrons released from the scattered photons. Depending on the source of the scattered photon, the scattered dose can be further divided into *head scattered* if the scattered photon is produced in the LINAC head or the *phantom scatter* if the photon is scattered inside the medium.

Since it is hard to measure the dose directly inside a patient or in-air, a water phantom which has close radiation absorption and scatter properties to real patients is always utilized to qualify the dosimetric properties of a photon beam. The most common quantity defined is called percentage depth dose (PDD), that characterizes the dose variation along the central axis of the beam in the water phantom. It is defined as a percentage of the dose at any depth d to the dose at a fixed reference depth d_0. Usually the reference depth is chosen at the depth of the maximum dose d_{max}. A typical PDD curve for a 6 MV photon beam in a homogenous water phantom is shown in Figure 2.12. The dose rise from a relative low value at the surface to the maximum value at d_{max}. This region is referred to the buildup region. This is due to the fact that the ejected electrons by incident photons at the surface or at the shallow depth travel along a forward direction. The increased electron density with increase depth lead to elevated dose levels. After the buildup region, the dose decreases with the depth because of the photon beam attenuates. The depth of d_{max} and the shape of PDD curves depend on the beam energy, filed size and source to (phantom) surface distance (SSD), etc..

Figure 2.13 plots dose profiles at different depths, i.e. 5cm, 10cm and 20cm, for a typical 6MV photon beam with 40x40cm^2 open field. The profile has three regions: *plateau*, *penumbra* and *umbra*. The flattening filter in the LINAC head is designed to attenuate the forward peaked photon beam ejected from the LINAC target more in the center than in the periphery region, so that the plateau (central region of the beam) is relatively uniform at 10cm in water. However because of different level of beam hardening and scattering at different depths, the profiles are over flattened at shallow depths (i.e. 5cm) and exhibit *horns* in the plateau near the field edge. Penumbral is usually defined as the region between the 80% and the 20% dose level of the central axis value, which is contributed mainly by scattered dose. Umbra is the region far from the radiation field edge where the dose is ascribed to the scatter photons, as well as the radiation transmitted from the LINAC head.

The third important quantity is beam output factor. For a given field size, it is defined as the ratio of the dose on the central axis at the reference depth to the dose for the reference field size under the same geometry condition. In most of cases, 10x10cm^2 is referred to as the reference field size. A typical 6MV photon beam output factor curve is depicted in Figure. 2.14. The monotonically increasing trend of the curve is due to more and more head scatter and phantom scatter, as the field size is increased.

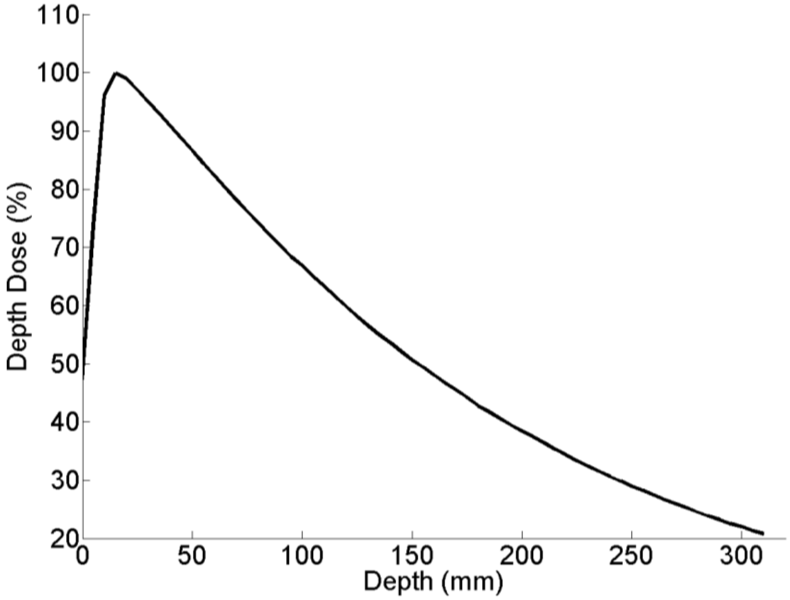

Figure 2.12: A typical PDD curve for a 6MV photon beam.

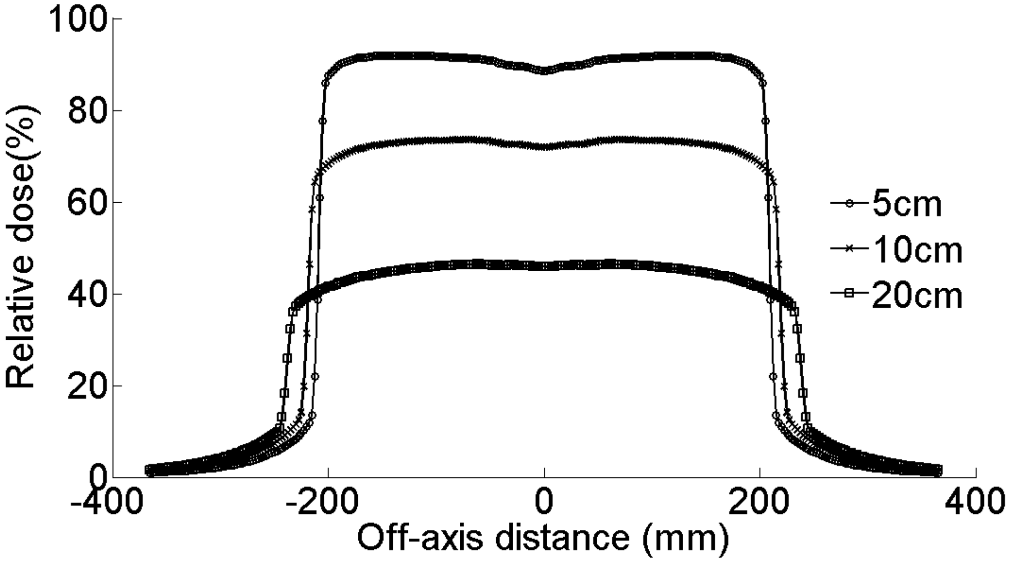

Figure 2.13: Dose deposition profiles at difference depths for a typical 6MV photon beam.

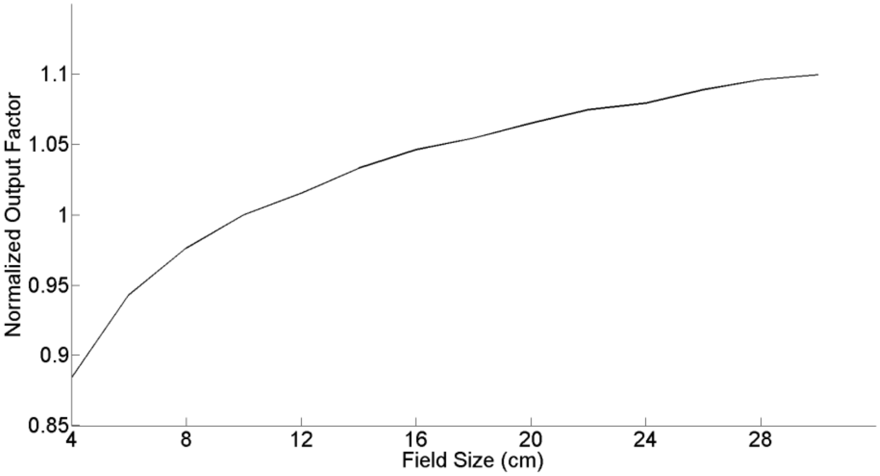

Figure 2.14: Beam output factor curve for a typical 6MV photon beam.

2.5.2 Overview of Monte Carlo Source Modeling

In an MC simulation for dose calculation, the overall accuracy is determined by the accuracy of LINAC beam source model and that of particle transport inside the patient. Therefore, developing a source model and commissioning it against a specific LINAC are important for implementing the MC based dose calculations for clinical use (Jiang *et al.*, 2000; Deng *et al.*, 2003). Several types of source models and the associated commissioning methods have been developed over the years. (1) Direct use of a phase-space file generated from LINAC head simulations. A phase-space file stores information of output particles from the LINAC head, including particle type, energy, position, direction, progeny and weights. Direct use of a phase-space file has the potential to provide the most accurate beam characteristic and has been employed by many popular CPU based MC dose calculation tools such as DOSXYZnrc (Walters *et al.*, 2005), MCNP (Siebers *et al.*, 1999), some versions of VMC++ (Gardner *et al.*, 2007) and the GPU based, gDPM (Townson *et al.*, 2013). The phase-space file is usually generated by another full MC simulation by simulating the physical process inside a LINAC head. This simulation is time consuming and requires detailed knowledge about the specific LINAC head geometry and materials, which may not be available to normal clinical users. (2) Phase-space-derived multiple-source models with or without enhancement from measurements (Ma *et al.*, 1997; Ma, 1998; von Wittenau *et al.*, 1999; Deng *et al.*, 2000; Fix *et al.*, 2004; Davidson *et al.*, 2008). These models divide the whole source model into different sub-sources, where the energy spectrum and particle fluence are derived from a phase-space file. However, this approach depends on the availability of a phase-space file for the LINAC. (3) Measurement based analytical or hybrid models (Jiang *et al.*, 2001; Fippel *et al.*, 2003). In these models, energy distributions and direction distributions are expressed in certain functional forms and parameters in these functional forms are tuned to match calculated data with measurement data in a commissioning process. Nonetheless, the commissioning process usually requires a large set of measurement data which are tedious to obtain. In addition, tuning the parameters usually requires solving a highly nonlinear and non-convex optimization problem, making it hard to control the algorithm convergence and numerical stability.

2.5.3 Our Source Model and Commissioning Method

We approach the source modeling and commissioning problem from a different angle compared to a mentioned available methods. For a QA purpose, identifying significant or catastrophic errors are most important and hence a few percents of error in source modeling is tolerable. The simplicity of the model is also important to ensure its practicality, as a clinical user may not have the expertise to finely tune the model. As such, we have proposed a practical point source model in the GPU based MC QA tool. Three main factors are considered in our model. (1) a source energy spectrum is used to tune the dose deposition behavior along the depth direction. (2) a beam fluence is used to modulate the dose along the lateral direction, particular the "horn effect". (3) The omitted scatter component in the source model leads to incorrect beam output, which is compensated by an output correction factor. All of those parameters in this source model are derived from a minimum number of clinical measurement data.

As for the commissioning process, it should be accomplished semi-automatically and requires no knowledge about the LINAC head geometry details. This makes it easy for the normal clinical personals to adopt it for various versions of the LINAC machines. Hence, we proposed a commissioning process associated with our beam model as following. (1) It is known that under a reference condition the shape of PDD curve in water phantom mainly depends on the energy spectrum. Therefore, we first evenly divide a full energy spectrum into different energy bins. Then compute dose in water from a point source with a uniform photon fluence for different energy bins. When it comes to the dose for a full energy spectrum case, it is simply a sum of the doses from those energy bins weighted by the factors associated with the bin. Hence, the energy spectrum is derived by adjusting the weighting factor for each energy to match the resulting PDD with the measured one. (2) We partition the beam front with a 2D rectangular grid and each of the grid space is called a *beamlets*. Once the spectrum is determined, We first compute dose from each beamlet with the previously commissioned spectrum considered. Then for a beam with a nonuniform photon fluence, the total dose is a sum of the doses from all beamlets weighted by the factors associated with those beamlets. These factors can be obtained by matching the dose profiles at several depths with the corresponding measured ones. (3) Lastly, to correct the output factors, we compute the output factor for various field size using the previously commissioned spectrum and fluence factors. We also measure real beam output factors in water. The ratio of the measured output factor to the calculated factor at each field size is the correction factor.

2.5.4 Implementation Details

There are two parts of input data required to conduct our commissioning procedure. One part is a small set of standard beam measurement data, such as PDD and lateral profiles, which already exist at the commissioning stage of the LINAC beam. At UCSD, the beam commissioning is performed using a homogeneous water tank with 100cm SSD setup. The data we need is the PDD curve for the reference field size 10x10cm^2, dose profiles at different depths for open beam of 40x40cm^2 field size, as well as the beam output factor for square fields of various sizes.

The second part of input data are the MC pre-calculated beamlet PDDs and dose profiles. In our implementation, we evenly divide the 2D 40x40cm^2 beam front into a grid of small beamlets with 1x1cm^2 resolution, and divide the energy range of a 6MV beam into 10 energy bins, i.e. [0MeV,0.66MeV], [0.66MeV,1.32MeV],..., [5.96MeV,6.6MeV]. We pre-calculated the dose deposition in a water phantom for each energy bin at each beamlet location using the MC dose engine gDPM. In all of these calculations, the resolution of the water phantom is $0.5\times0.5\times0.5$cm^3 and the phantom is set at 100cm SSD. With the dose distribution indexed by the beamlet and the energy, the data required in the commissioning can be obtained by summing doses along the energy or the spatial dimension. For instance, the dose data required in the spectrum commissioning stage, i.e. dose for each energy bin with a flat beam fluence can be obtained by summing the pre-generated dose data along the spatial dimension.

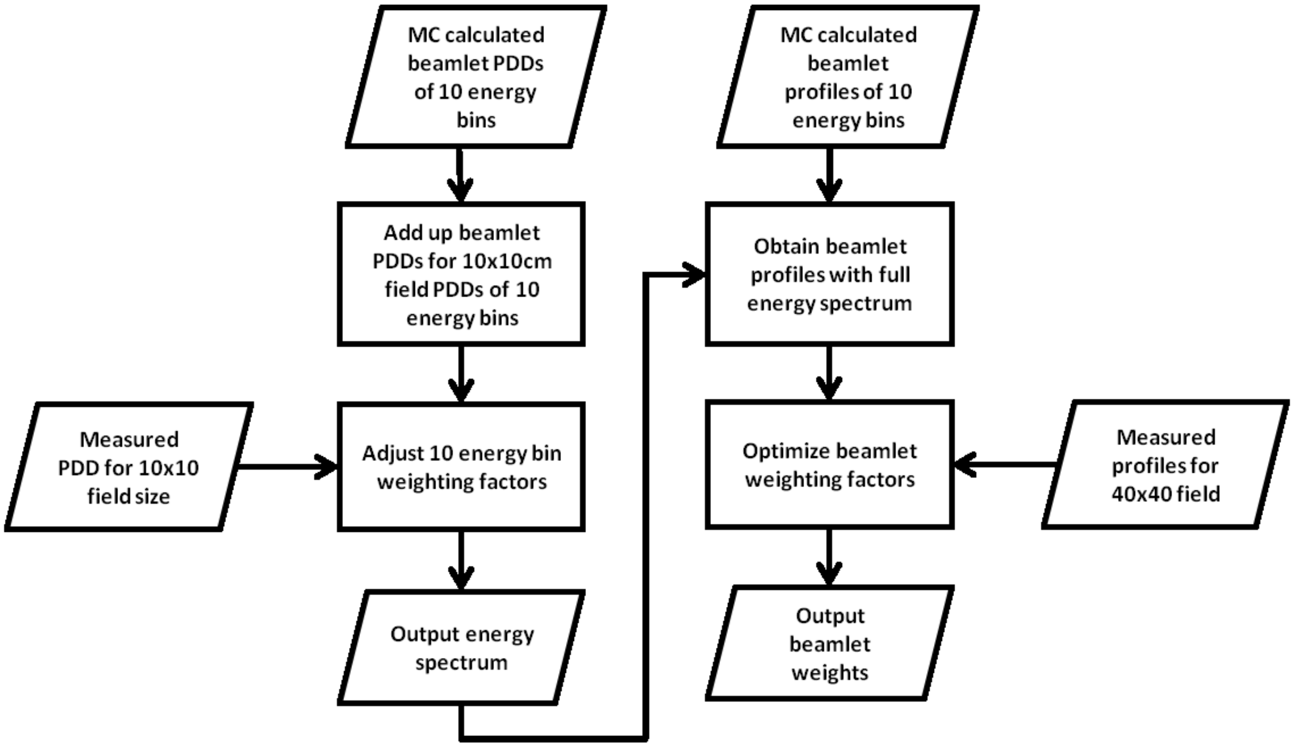

Figure 2.15: Workflow of commissioning procedure to obtain energy spectrum and beam fluence.

Figure 2.15 illustrates the commissioning workflow to obtain the energy spectrum and the beam fluence. There are a few details that we would like to present. First, being able to adjust each energy bin weights provides the maximum flexibility to fine tune the energy spectrum comparing with those methods of modeling the spectrum shape using some function forms (Davidson *et al.*, 2008). However some constraints can still be helpful to ensure the correctness of the resulting spectrum. From our experience and MC simulation results for LINAC head, there are several characteristics of a 6MV beam spectrum: (1) there is only one peak; (2) the peak usually appears at the energy bin [0.66MeV,1.32MeV]; (3) the average energy value for 6MV beam is usually between 1.5 MeV to 2 MeV. Considering these constraints, we have designed a graphical user interface (GUI) in Matlab (MathWorks Inc., Natick, MA) for users to easily adjust the energy bin weighting factors. Once a user updated a weighting factor at an energy bin, factors at other bins are also automatically modified to reflect the spectrum characteristics. Meanwhile, the corresponding PDD curve is generated and its max difference with respect to the measured PDD is calculated, as well as the average energy value from the current energy spectrum. The user can easily modify the spectrum using this GUI to achieve a desire one.

Once the user is satisfied with the energy spectrum shape and the commissioned PDD curve. The user confirms the energy spectrum and the dose profiles with the spectrum for each beamlet can be immediately obtained.

The following step of determining beamlet weights is conducted in an automatic fashion. Mathematically, we would like to solve a linear equation,

$$Aw = y, \tag{2.26}$$

where w is a vector containing the weighting factors of all beamlets that are needed to be commissioned. Each column of the matrix A represents a vector of the pre-calculated dose profiles of full energy spectrum for a corresponding beamlet and y is a vector of the measured dose profiles. For the measured dose profiles, they are taken at depths greater than d_{max} to exclude the dose contributions from the electron contaminations.

Since the number of beamlets is typically more than the number of measurement data due to the fine spatial resolution of the beamlets, the problem is apparently underdetermined and there exist infinitely many solutions. In order to solve this issue, we add a symmetric property to the vector w such that

$$w = B\widehat{w}. \tag{2.27}$$

Here, $\widehat{w}(r)$ is a function of radius r on the beam front and B is a linear operator that extends $\widehat{w}(r)$ to the entire 2D plane by rotating $\widehat{w}$ around the origin. In addition, we suppose the beam fluence is smooth along the spatial dimension. Therefore, we minimize the gradient of $\widehat{w}(r)$ to enforce the smoothness requirement. These considerations lead to an optimization problem of:

$$\hat{w} = \operatorname{argmin}_{\hat{w}} |\nabla \hat{w}(r)|^2, \quad s.t.\ AB\hat{w} = y. \tag{2.28}$$

Augmented Lagrangian (Hestenes, 1969; Powell, 1969) method is adopted to solve the problem in Equation 2.28, which iteratively performs the two steps:

(P1): $\hat{w}^{(n+1)} = \operatorname{argmin}_{\hat{w}} |\nabla \hat{w}(r)|^2 + \frac{\alpha}{2} \left\| AB\hat{w} - y^{(k)} \right\|_2^2,$ (2.29)

(P2): $y^{(n+1)} = y^{(n)} - \beta(AB\hat{w}^{(n)} - y).$ (2.30)

Here, α is the parameter to adjust the relative weight between the smoothness penalty and data fidelity term. β controls the convergence speed. For the sub-problem (P1), since the cost function defined in this minimization problem is quadratic, it is sufficient to consider its optimality condition:

$$\alpha C^T C\hat{w} - \Delta\hat{w} = C^T y^{(n)}. \tag{2.31}$$

Here, we use $C = AB$ for convenience. T denotes the matrix transpose, and Δ is the Laplacian operator. Since the operator $K = \alpha C^T C - \Delta$ is symmetric and positive definite, we use conjugate gradient method to solve the problem $K\hat{w} = h$, where $h = C^T y^{(n)}$. The two steps are iterated, until the objective function doesn’t decrease more 0.1% in five consecutive steps.

After finishing commissioning the energy spectrum and the beam fluence, the output factors of our model for different field sizes are corrected against the beam measurement. Specifically, the point dose at the depth of 5cm is calculated using the commissioned spectrum and beam fluence. The result is normalized by the dose at the same depth for the reference field size $10x10cm^2$. For the clinical relevant field size, we measure the beam output factors for various square field from 4x4cm to 30x30cm. The ratio between the measured value and the calculated value for each field size is the correction factor.

2.5.5 Commissioning Results

Figure 2.16 displays the MATLAB GUI for our energy spectrum commissioning. For this dissertation, we commission the source model against a Varian TrueBeam 6MV energy photon beam. Individual PDD curves of reference field size of $10x10cm^2$ for different energy bins are shown in Figure 2.17. The commissioned energy spectrum is displayed in Figure 2.18. The spectrum shape is very reasonable with our pre-knowledge and the average energy value is 1.65 MeV. The commissioned PDD and its difference with the measurements are also plotted in Figure 2.19. Good agreement between the two PDD curves is observed and the maximum difference after the d_{max} is below 0.5%.

Figure 2.20 displays the commissioned beam fluence as well as line profile along the center axis. The increased fluence with the off-axis distance accounts for the "horn effect" seen in the dose profiles at the shallow depths. In Figure 2.21(A), the commissioned dose profiles at different depths are plotted in blue and the measurements are in red. Profiles calculated using a uniform beamlet fluence is also shown in green curves. It is observed that a much better agreement with the measurement is achieved when considering the "horn effect" in the beam fluence. In Figure 2.21(B), differences of profiles with respect to measurement data at 10cm depth are shown. The average dose difference in the plateau region drops considerably after the commissioning. Yet, a relatively large discrepancy still appears at the beam penumbra region, which can be ascribed to the LINAC head scatter dose that is not considered in our beam model. Finally, the source model output factor before correction is compared with the measured beam output factor data in Figure 2.22. This yields the correction factor ranging from 0.93 at the field size 4x4cm^2 to 1.04 at the field size 30x30cm^2.

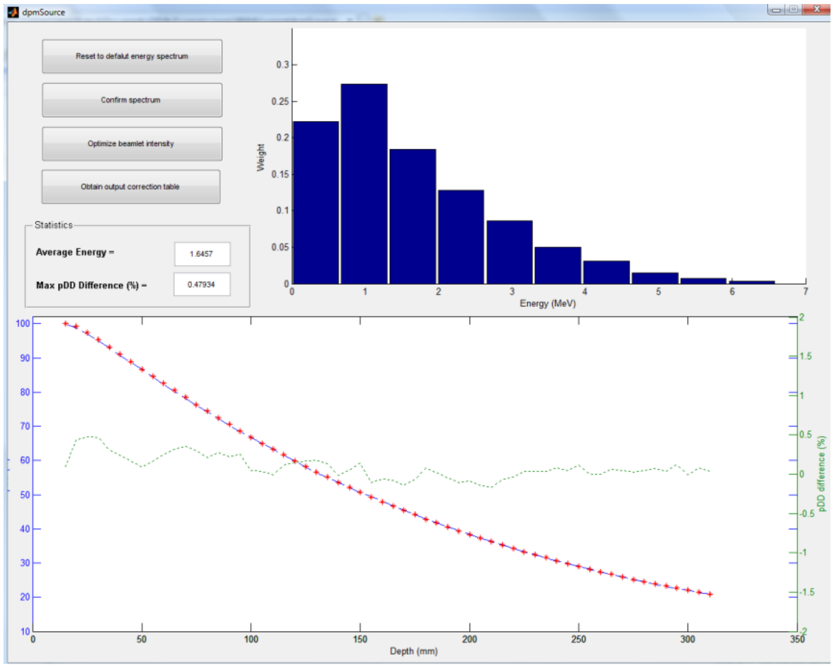

Statistics

Average Energy = 1.6457

Max pDD Difference (%) = 0.47934

Figure 2.16: MATLAB GUI for our source commissioning.

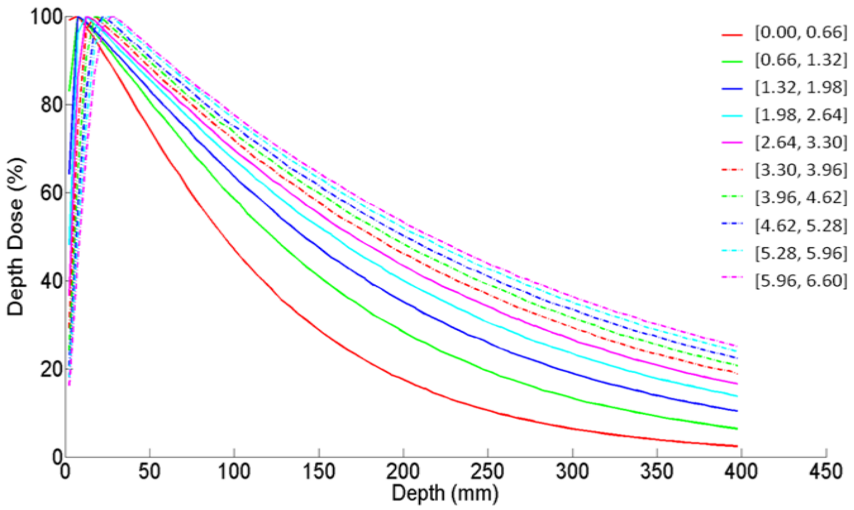

Figure 2.17: Reference field size PDD curves for different energy bins.

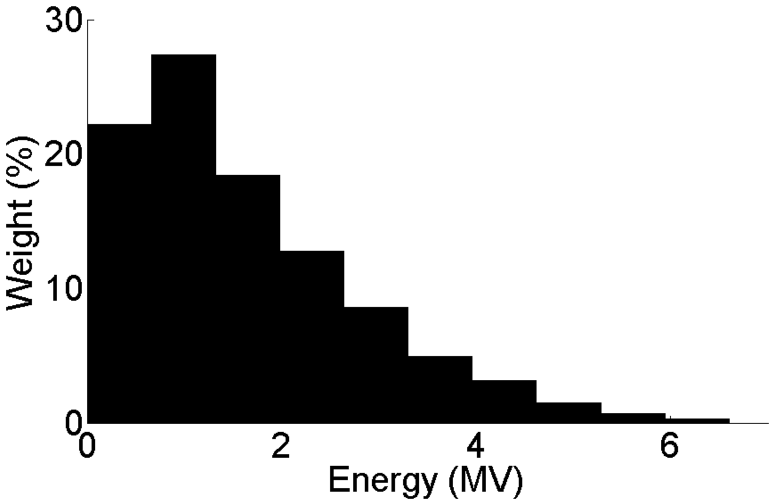

Figure 2.18: Commissioned energy spectrum for a 6MV beam.

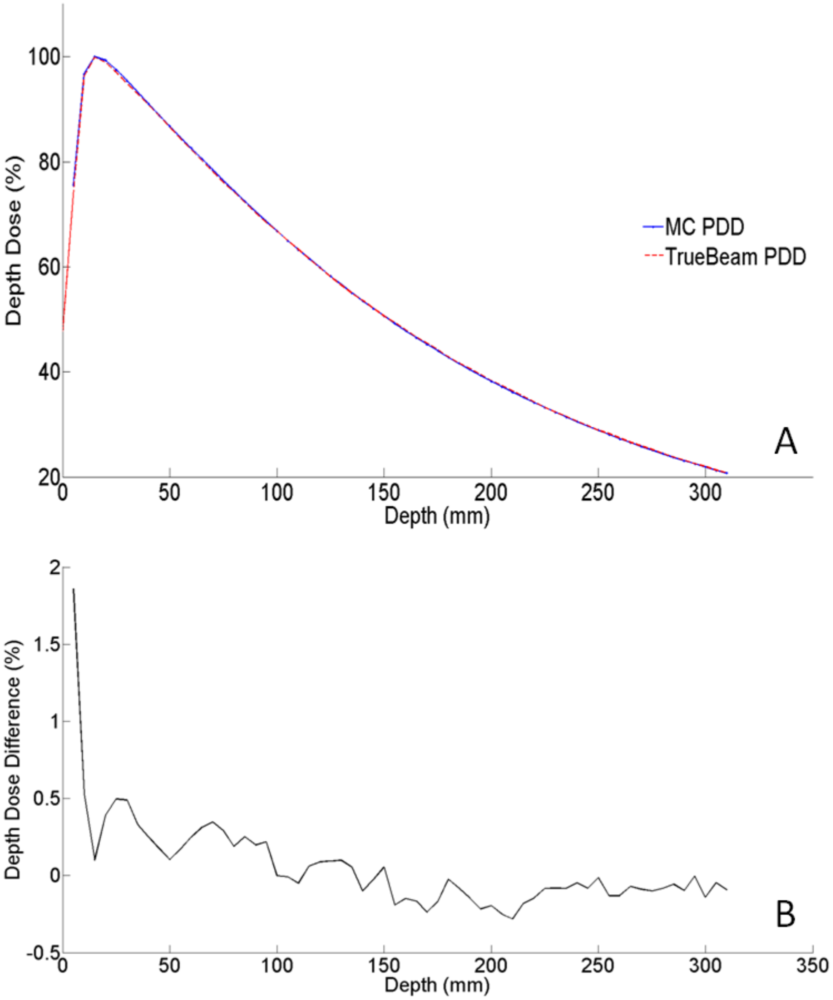

Figure 2.19: (A) Commissioned PDD vs measured PDD. (B) Difference plot.

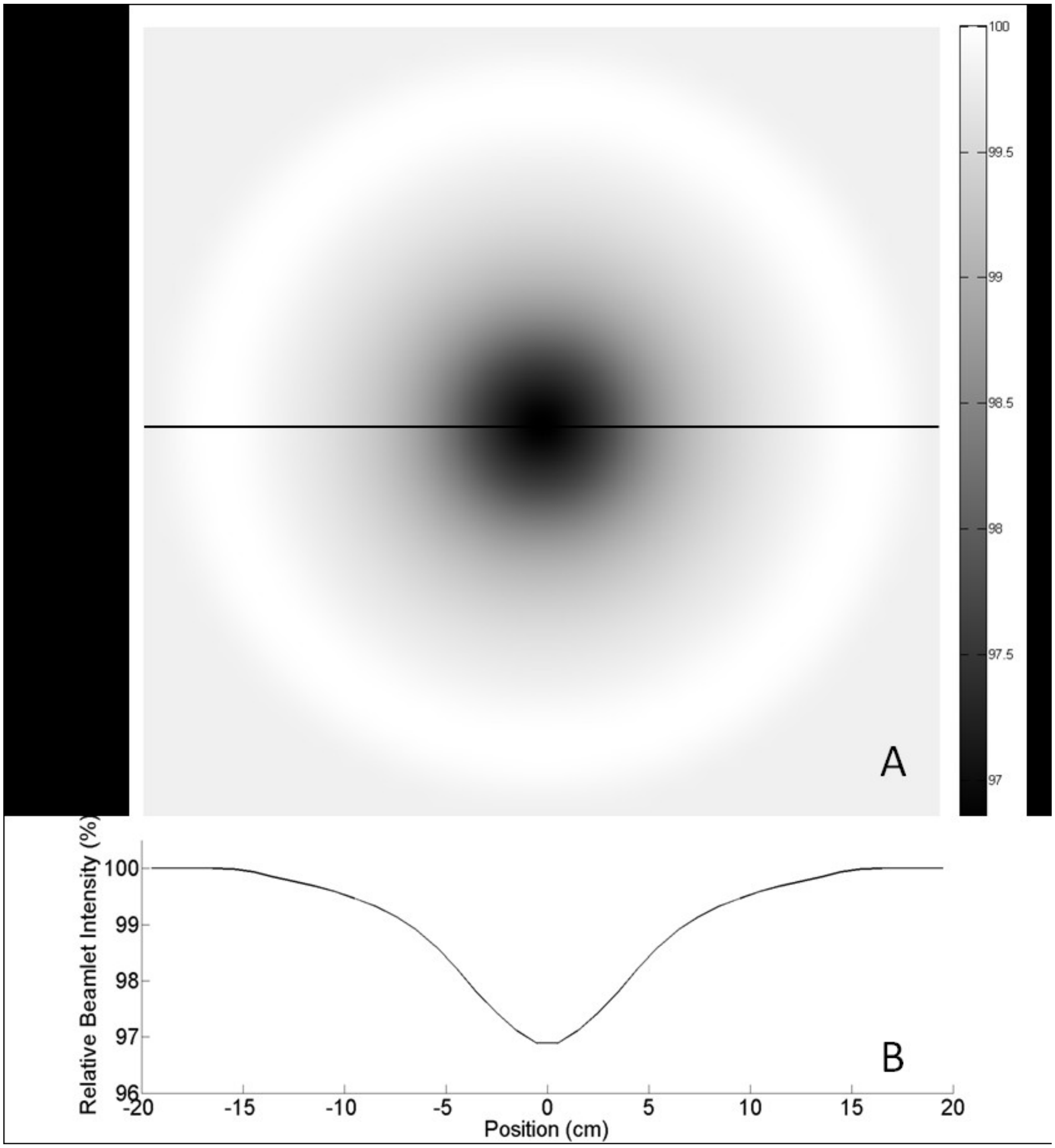

Figure 2.20: (A) 2D commissioned beam fluence. (B) Line profile along the center.

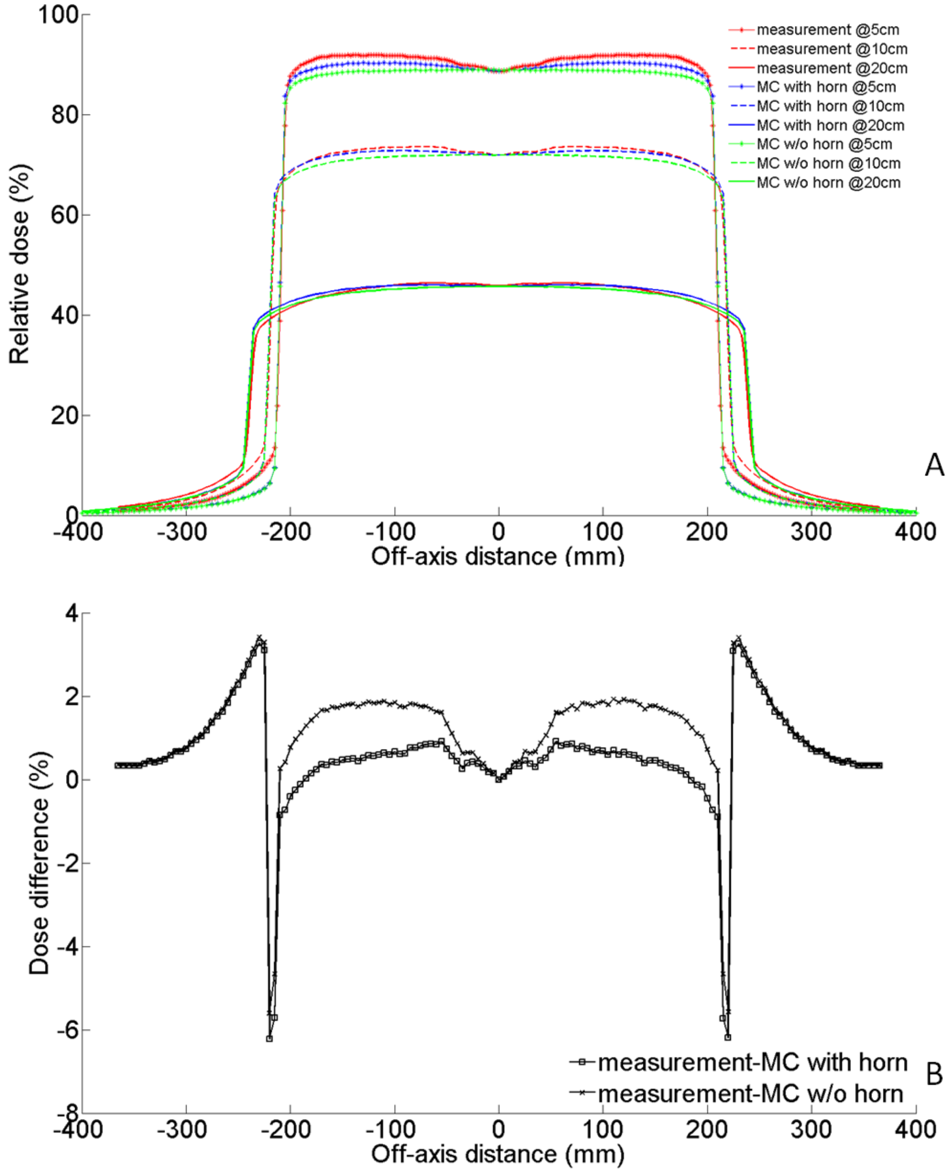

Figure 2.21: (A) Dose profiles at 5cm,10cm and 20cm depths. (B) Difference of profiles at 10cm depth.

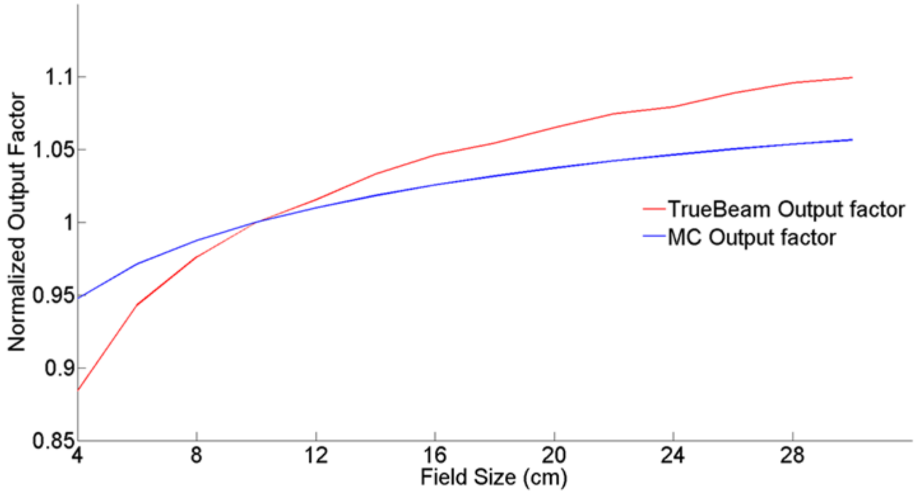

Figure 2.22: The source model output factor before correction is compared with the measured beam output factor data.

2.5.6 Patient Case Validation

We have also validated our source model in a prostate case and a HN patient case. In these cases, the ground truth dose data is calculated using MC code gDPM together with a source model developed by Townson *et al.* (2013) based on the pre-processed patient-independent phase-space file of a Varian TrueBeam 6MV beam obtained at www.iaea.org. This beam model is referred as the phase-space-let (PSL) method from here on. The accuracy of the dose calculation results using this PSL beam model has been well accepted, since the phase-space file provides the most accurate beam characteristic.

To calculate a patient plan dose, either using our beam model or the PSL beam model, plan fluence maps are first derived from the MLC leaf motion sequence stored the patient-specific treatment plan in a DICOM format. We have developed a computational module to achieve this goal. The details of the fluence map generation will be presented later.

To eliminate the effects of statistical uncertainty in dose comparisons, we simulated a large number of particles histories in each MC dose calculations, so that the average uncertainty level within 50% isodose line is less than 0.2% of D_{max}. In all the cases, the dose voxel resolution is $2.5x2.5x2.5cm^3$. GPU based 3D γ-index test, gGamma, is performed to compare the dose calculated using our beam model with the ground truth dose with 2%/2mm criteria.

Table 2.6 summarized the γ-index evaluation results. For both cases, the maximum γ and the mean γ are very low. This fact holds both for the high dose region inside the 50% isodose line and the low dose region inside the 10% isodose line. In particular, over 99% of the voxels within the two regions pass 2%/2mm criteria. These results clearly show the good agreement between the dose results calculated by our source model and the PSL model, indicating that the accuracy of our model is sufficient for QA purpose.

Table 2.6: γ-index test results for MC dose distributions using our source model and using PSL model.

Case	High dose region statistics			Low dose region statistics		
	max γ	mean γ	passing rate(%)	max γ	mean γ	passing rate(%)
Prostate	1.38	0.23	99.79	1.38	0.15	99.98
HN	1.39	0.16	99.98	1.39	0.17	99.99

2.6 Fluence Map Generation

Once the MC beam is commissioned, it can be used in dose calculations for real patient cases. Nonetheless, in an IMRT or a VMAT case, the intensity is not homogeneous across the entire beam region. Instead, a beam modulation is achieved by a MLC leaf motion sequence that is specifically designed for a patient, so that the resulting dose distribution focuses on the tumor area, while maximally sparing critical organs. The beam modulation is typically described by a fluence map, a 2D function characterizing the photon fluence on a plane perpendicular to the beam direction. Hence it is necessary to develop another module to calculate the fluence map from a MLC leaf sequence. In this chapter, the transmission property of a MLC will be first discussed. Our fluence map generation module will be then presented.

2.6.1 MLC Transmission Property

A MLC that has 60 pairs of opposing leafs is installed on a Varian TrueBeam LINAC machine. It is 53.9cm away from the X-ray target. Each leaf has a rounded leaf end with 8cm radius of curvature. Let us consider an MLC leaf position e in Figure 2.23. The leaf-tip position e projected to the iso-center level is E. Because of the rounded leaf end, a light field boundary is defined by a ray line that is tangent with the rounded end, i.e. the line SdD. Boyer and Li (1997) analyzed the geometric relationship between the light field edge, X_i and the leaf-tip projection position, W_i, yielding

$$X_i = \frac{W_i \cdot \mathrm{SCD} \pm \mathrm{SAD} \cdot R \cdot \left(1 - \mathrm{SAD}/\sqrt{\mathrm{SAD}^2 + {W_i}^2}\right)}{\mathrm{SCD} \pm R \cdot W_i/\sqrt{\mathrm{SAD}^2 + {W_i}^2}}, \qquad (2.32)$$

where SCD and SAD denote source to collimator (MLC) distance and source to axis (isocenter) distance, respectively and *R* is the radius of the leaf end. The plus sign is used in the solution for leaves that are not across the beam central axis and the minus sign is used otherwise.

In contrast to the light field, X-ray can penetrate through the MLC with its intensity attenuated by the MLC material. Beyond the light field boundary, the more lateral an X-ray is, the longer the X-ray path length intersecting with the MLC, leading to gradually reduced X-ray intensity. To compute the profile of transmission intensity as a function of spatial location, it is necessary to first compute the length that an X-ray line intersects with the leaf.

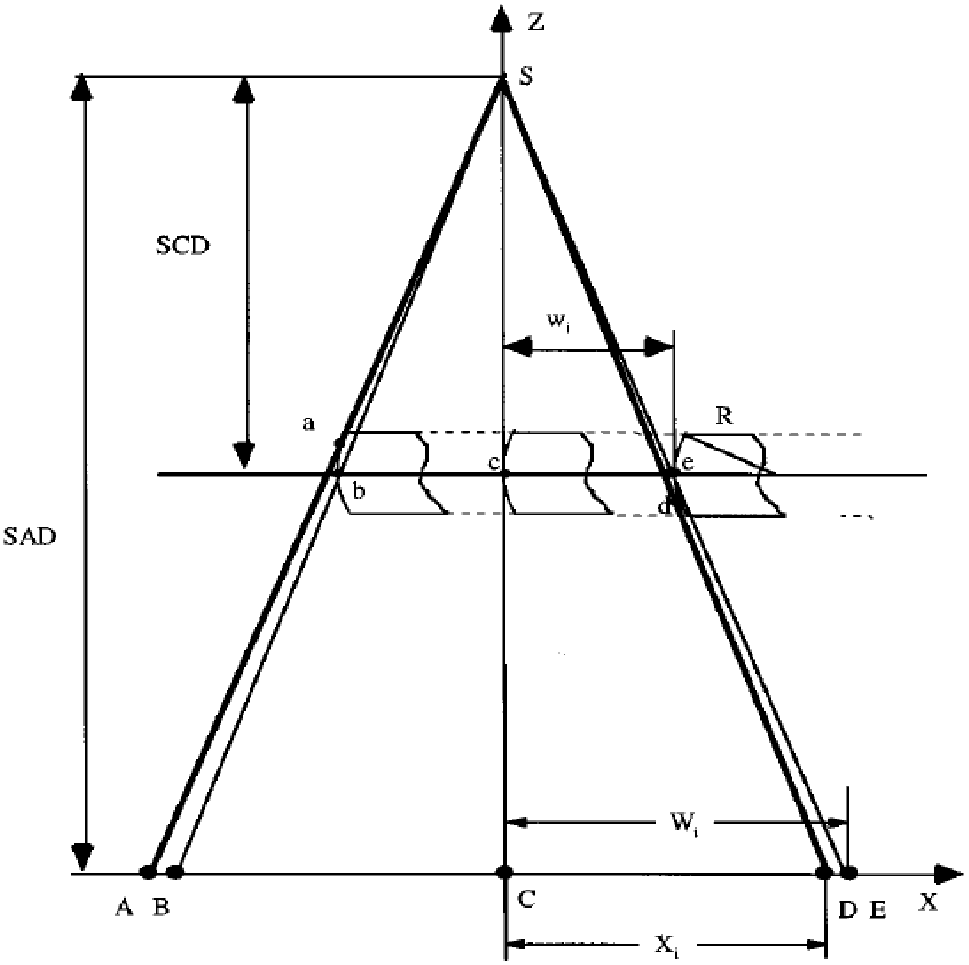

Figure 2.23: Diagram showing the relation between the light field edge and leaf-tip projection. C is the machine isocenter. The points A,B,C,D and E at the SAD distance are the projection of the points a,b,c,d and e at the leaf end distance, respectively. (Adopted from Boyer and Li (1997))

As in Figure 2.24, suppose an X-ray ray line passes through the leaf end with a pass lengths l, it is displaced from the light-field ray by a distance d. d' denote the projection of d onto the horizontal planes at the point where the light-field is tangent to the rounded leaf end. Denote δ the projection of d' on the isocenter plane, we can derive that

$$\delta = \frac{(R-\sqrt{\mathrm{R}^2-\frac{l^2}{4}})\cdot\sqrt{\mathrm{SAD}^2+{W_i}^2}}{\mathrm{SCD}\pm R\cdot W_i/\sqrt{\mathrm{SAD}^2+{W_i}^2}}. \tag{2.33}$$

The transmission factor α through the rounded leaf end is

$$\alpha = e^{-\frac{\ln 2}{\mathrm{HVT}}\cdot l}, \tag{2.34}$$

where HVT represents half-value thickness of the leaf material, which is 0.95cm for the tungsten material in our MLC . Considering Equation 2.33, the transmission α is derived as

$$\alpha(\delta) = \exp\left(-\frac{\sqrt{2R\delta r_1}}{\mathrm{r}_2}\right), \tag{2.35}$$

where $r_1 = \frac{\mathrm{SCD}\ \pm R\cdot W_i\cdot\sqrt{\mathrm{SAD}^2+{W_i}^2}}{\sqrt{\mathrm{SAD}^2+{W_i}^2}}$ and $r_2 = \frac{\mathrm{HVT}}{2\ln 2}$. An example of the transmission factor through the rounded MLC leaf end as a function of the distance δ from the light-field edge, when the light-field edge is at the middle of beam, is shown in Figure 2.25. The transmission initially stays at 100% level where the X-ray is not blocked. It then monotonically decays in a region called a penumbra region. When the distance is far away from the light-field edge, the transmission reaches the background value 0.19%. This is determined by the path length when the X-ray intersects with the portion of the MLC with parallel up and down sides, as opposed to intersecting with the rounded leaf end.

In dose calculation for a patient case, we always compute fluence through a beamlet with a finite size. If the beamlet is in the transmission penumbra region, the average transmission in a beamlet is given by,

$$\overline{\alpha}(a,b) = \frac{\int_{a}^{b} \alpha(\delta)\, d\delta}{b-a}\,, \tag{2.36}$$

where a and b are the coordinates of the beamlet edges. Combing Equation 2.35 and 2.36, we obtain that

$$\overline{\alpha}(a,b) = \frac{-2}{\mu(b-a)} e^{-\mu t}\left(t + \frac{1}{\mu}\right)\Big|_{t=\sqrt{a}}^{t=\sqrt{b}}. \tag{2.37}$$

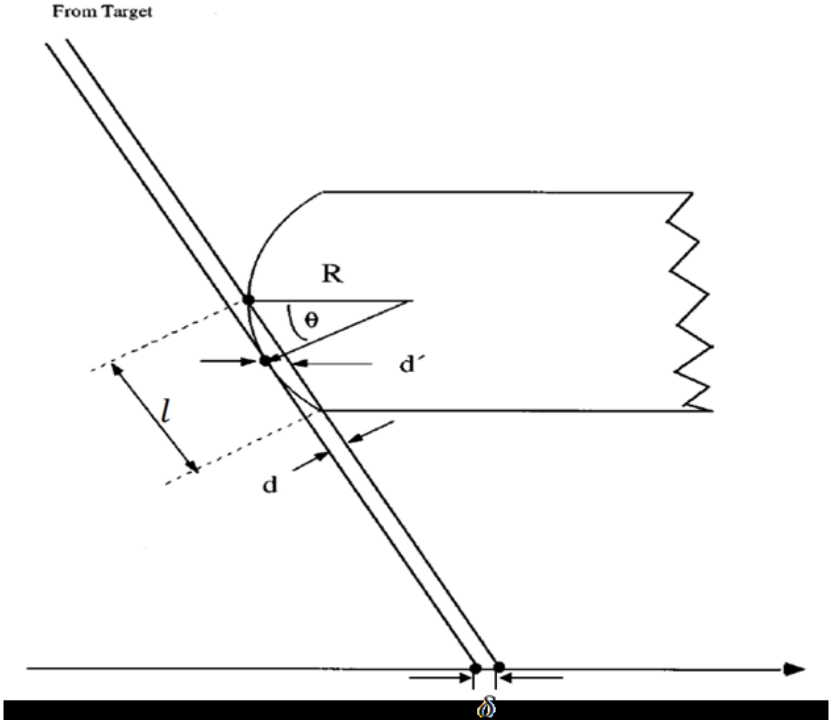

Figure 2.24: Diagram of X-ray passing through MLC rounded end leaf (adopted from Boyer and Li (1997)).

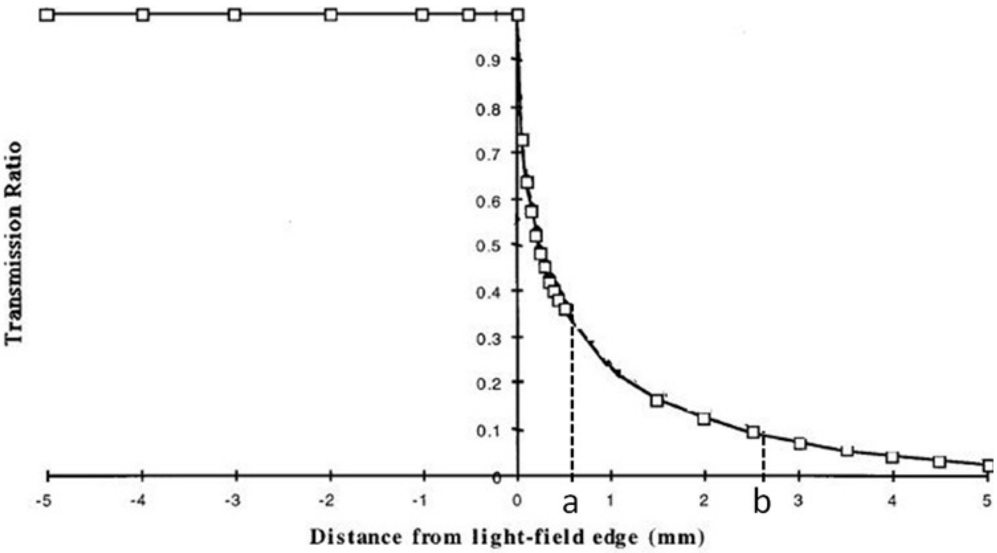

Figure 2.25: An example of radiation transmission ratio with the distance to light field edge when light field edge is at the middle of beam field (adopted from Boyer and Li (1997)).

2.6.2 Fluence Map From DICOM Files

The Varian version of 60-pairs MLC consists of 40 central leave pairs and 20 outer pairs and the projected widths of the central and the outer leafs at the isocenter plane are 0.5cm and 1cm, respectively. We divide the 2D 40x40cm^2 open field beam into a grid of beamlets with a resolution 0.5x0.2cm^2, where 0.5cm is along the leaf width direction, which is the highest resolution we can achieve in this MLC due to the leaf widths. 0.2cm is along the leaf motion direction.

A treatment plan for a patient case is usually stored in an DICOM file, where the beam intensity modulation at a particular beam angle is defined as a MLC leaf motion sequence at a set of control point series. At each control point, the leaf positions and fractional MU are recorded. Assume there are K control points for this beam, the fluence intensity I of beamlet x_n is the summation of the contributions of all the control points,

$$I(x_n) = \sum_{i=0}^{K} f_i \, \alpha_i(x_n), \tag{2.37}$$

where f_i is the fractional MU of the *i* th control point and $\alpha_i(x_n)$ is the transmission factor at x_n corresponding to the MLC configuration at the *i* th control point. These transmission factors are simply calculated using the formula shown in the previous subsection. Moreover, we assume the jaws are perfect collimators, such that the transmission factor is 0% for those beamlets outside the jaw opening.

Here, we give an example of fluence maps for a typical 7-beam IMRT prostate plan. To demonstrate the fact of the MLC rounded leaf end, we also compute the fluence maps generated without considering the transmission in the penumbra area. Figure 2.26 displays example fluence maps at two selected beam angles, as well as the difference fluence map between maps computed with and without the round leaf end considered. It is apparent that the MLC transmission from the rounded end leaf is important to accurately generate a fluence map for subsequent dose calculation accuracy.

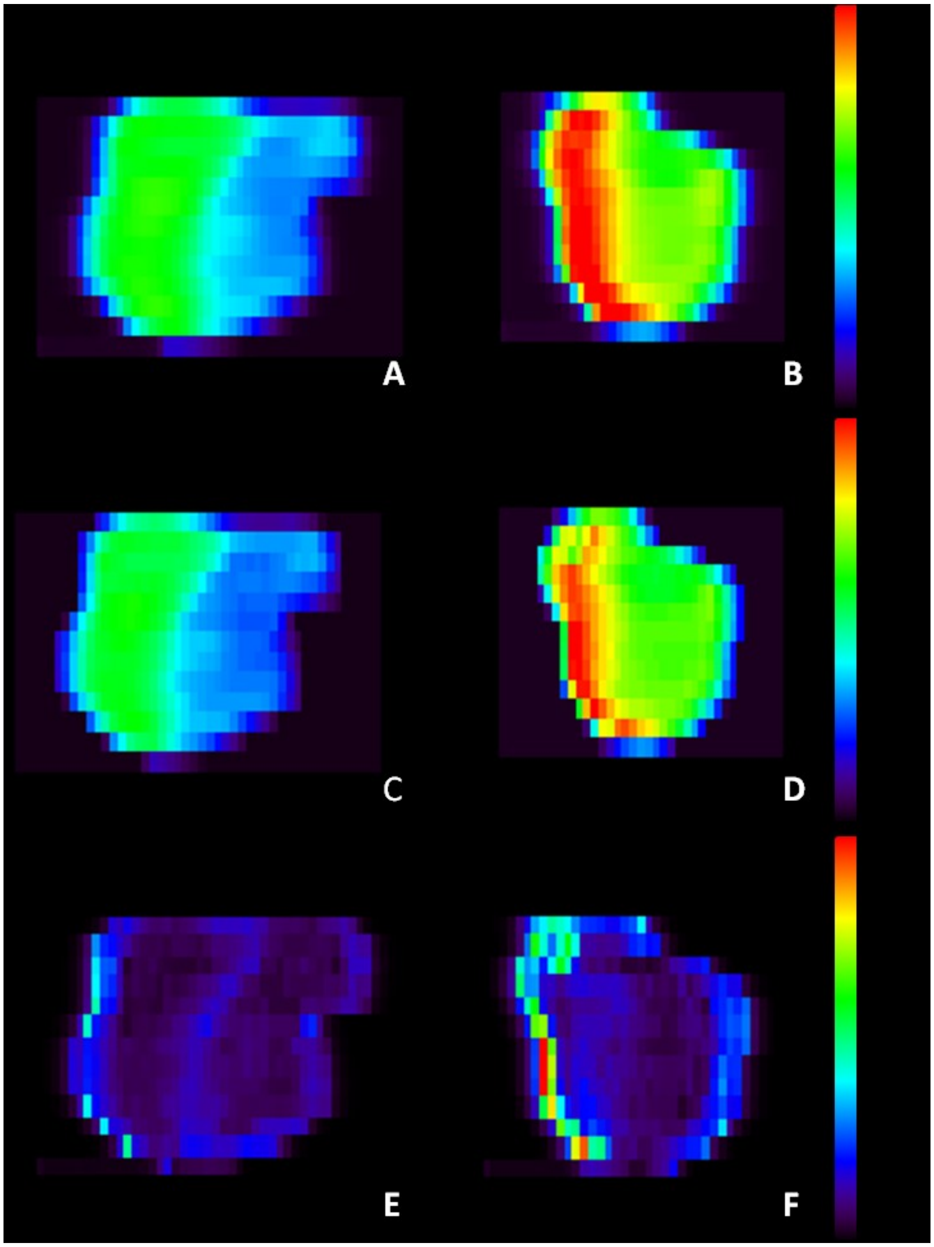

Figure 2.26: Fluence map examples. (A) and (B) Considering MLC rounded end leaf transmission. (C) and (D) Without considering MLC rounded end leaf transmission. (E) and (F) The fluence intensity differences. The two columns are for two beams in a IMRT plan.

2.6.3 Fluence Map From Log Files

During treatments, the Varian TrueBeam system logs segmental machine delivery information every 10 ms by the MLC controller, including MLC leaf positions, beam angle, collimator angle, cumulative dose fraction, jaw positions, beam hold status, *etc*., The recording continues till the treatment is completed, and the segmental information is stored to a trajectory log file afterwards. Each of these data has a planned value designed in the treatment plan and an actual value achieved during the delivery. An extensive summary of the data contained in the trajectory log file can be found in the reference (System, 2010). The accuracy of the recorded information has been validated using film measurement, 2D detector array and portal imagers (Li *et al.*, 2003; Zygmanski *et al.*, 2003; Zeidan *et al.*, 2004).

Calculating fluence maps from a trajectory log file follows the similar idea to that from a DICOM file. The fluence intensity I of a beamlet x_n is the summation of the contributions of all recorded segments in the log file. Hence,

$$I(x_n) = \sum_{i=0}^{S} f_i \, \alpha_i(x_n) \, B_i \, , \tag{2.38}$$

where S is the total number of segments, f_i is the fractional MU of the *i* th segment, $\alpha_i(x_n)$ is the transmission factor of the *i* th segments at the beamlet x_n. Comparing to Equation 2.37, there is an additional factor B_i , which is one or zero depending on the beam status on or off for the *i* th segment.

Two example fluence maps derived from a typical 7-beam IMRT prostate plan are shown in Figure 2.27. Results computed from both the plan through the DICOM file and from the log file are shown. A small difference is observed between them. The small magnitude of the difference indicates the high fidelity of beam delivery process with respect to the plan.

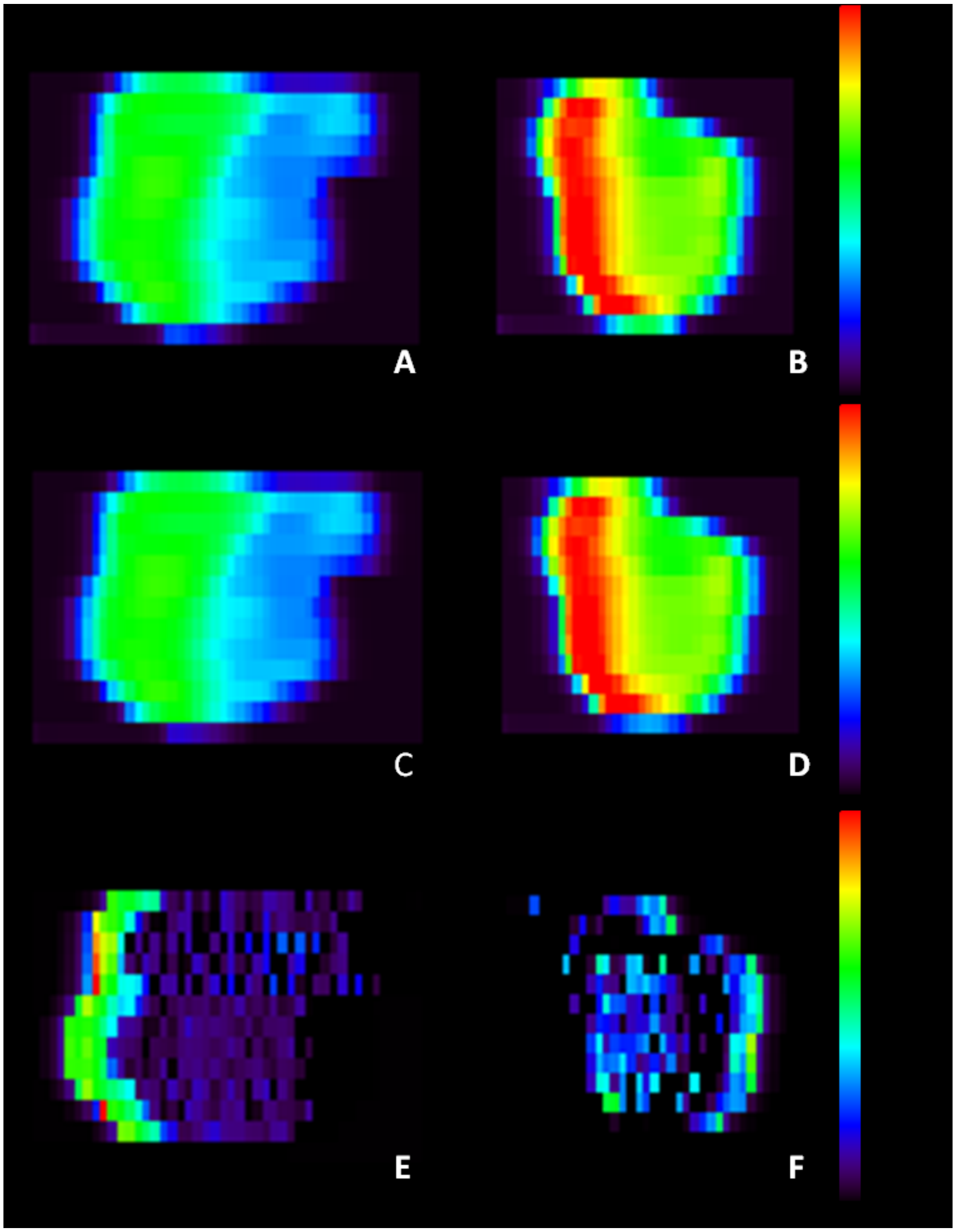

Figure 2.27: Fluence map examples. (A) and (B) From Dicom. (C) and (D) From Trajectory Log File. (E) and (F) The fluence intensity differences. The two columns are for two beams in a IMRT plan.

2.7 Web Application for Quality Assurance Tool

2.7.1 Quality Assurance Tool Workflow

With all of the issues studied in the previous part of this chapter, as well as those modules developed, we proceed to present our GPU based MC computational tool for QA purpose.

Figure 2.28 presents the workflow for this proposed tool. After a treatment plan is obtained from the TPS, all the beam parameter and the MLC leaf motion sequence are stored in the DICOM format. First we can obtain the initial plan DICOM and generate the plan fluence maps. Then the GPU-based MC dose engine, gDPM, is employed to calculate secondary dose (SD) on the patient CT using the generated plan fluence maps along with our source model. In this process, the resulting dose is smoothed using the GPU-based denoising algorithm to effectively reduce the MC uncertainty.

We also transfer the treatment plan to the TrueBeam LINAC machine and deliver the plan on it without any phantom setup. After the delivery, the trajectory log file which records machine delivery information is available. With the log files, we extract actually delivered fluence maps and calculate delivered dose (DD) using gDPM and denoising algorithm. γ-index evaluation tests and DHV comparisons are conducted among SD, DD and TPS plan dose (PD) to check for all possible error sources. (1) SD vs. PD can be used to check the TPS plan dose calculation accuracy. (2) Since DD and SD are obtained by the same dose calculation algorithm, the difference between them can demonstrate machine deliverability errors. (3) The comparison between DD and PD shows the accumulative errors including both the plan dose calculation inaccuracies and the beam delivery errors.

2.7.2 Web Application

To facilitate the clinical utilization of our tool, we have also developed a web application using HTML5, Python and Django. It provides a user-friendly interface for users to upload zipped DICOM data and machine log files and set parameters for the MC dose calculation and dose comparison criteria. After the files are uploaded, the MC dose calculation is then executed on the remote GPU server and the resultant dose distributions are displayed in the web GUI for the user to review. A 3D γ-index map and DVH curves are also displayed to the user. Finally, a QA report that summarizes the QA results can be downloaded in PDF format. Figure 2.29 presents the screen captures for the web application and a sample QA report is attached in the appendix. Such a tool is supported by all modern web browsers and it can be run on any major platform, even on all mobile devices. This web application makes remotely access possible and users can test and utilize this QA tool without purchasing expensive GPU hardware.

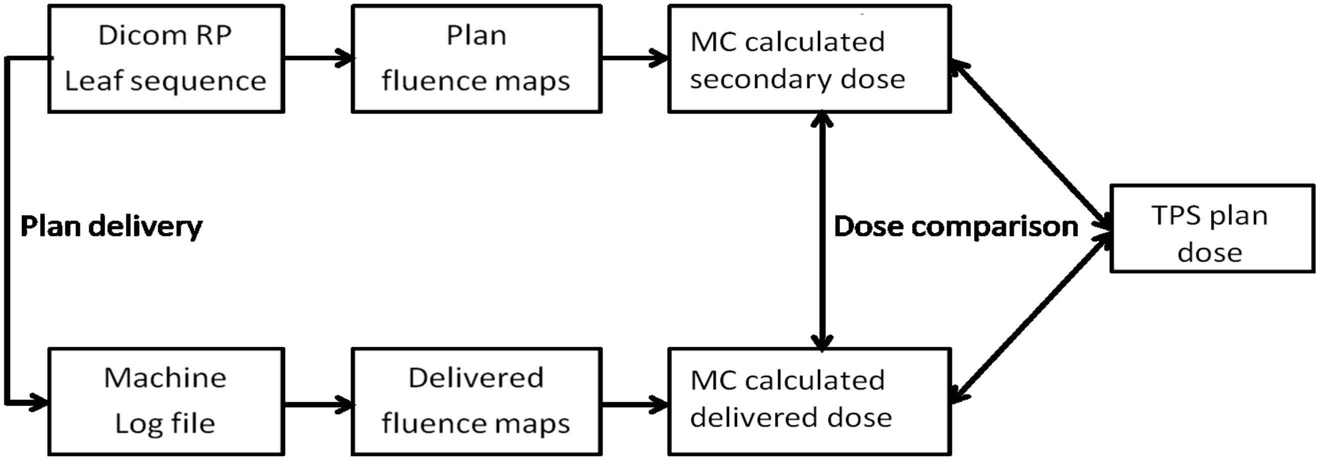

Figure 2.28: Workflow for the computational QA tool.

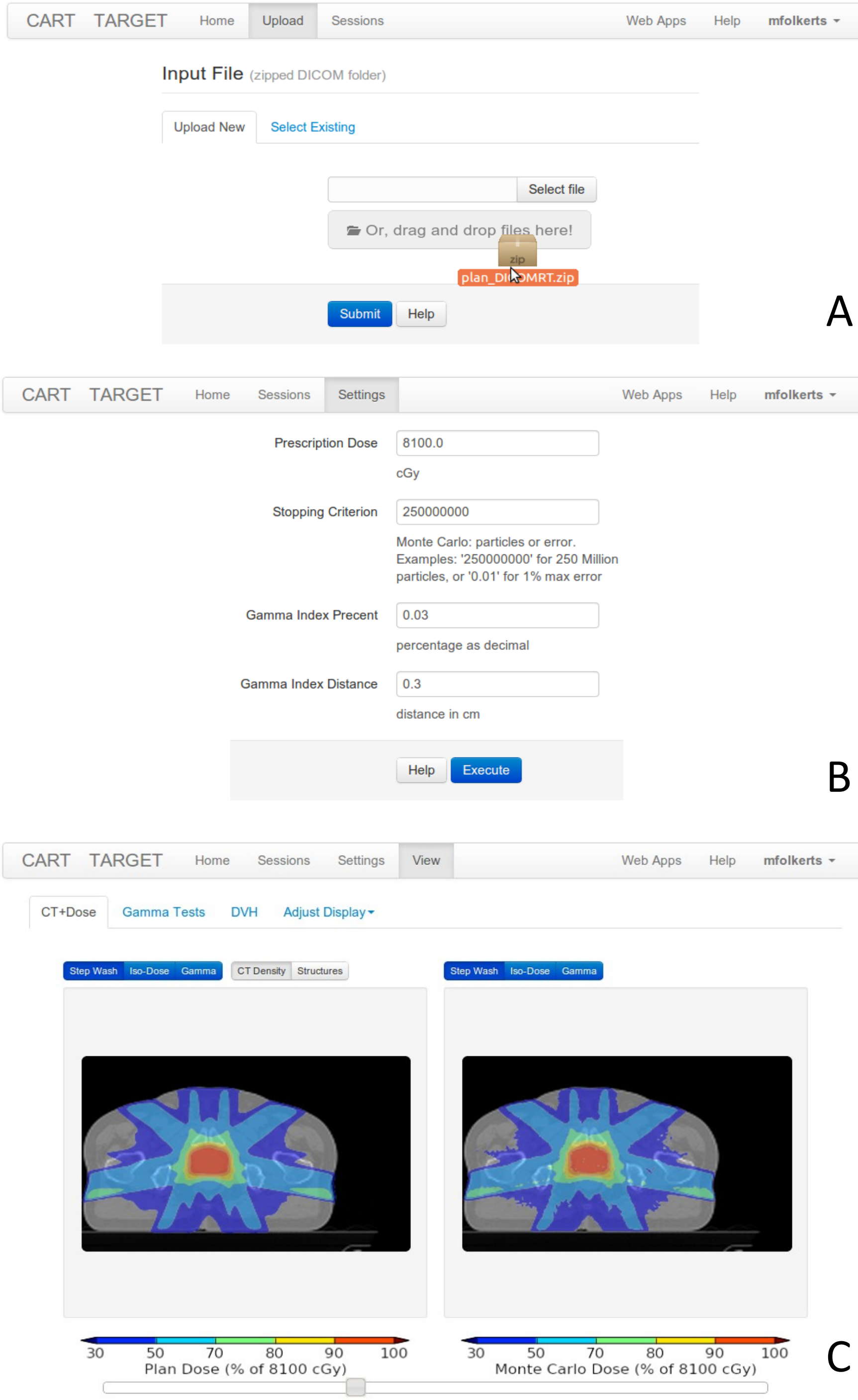

Input File (zipped DICOM folder)

Prescription Dose: 8100.0
cGy

Stopping Criterion: 250000000
Monte Carlo: particles or error. Examples: '250000000' for 250 Million particles, or '0.01' for 1% max error

Gamma Index Precent: 0.03
percentage as decimal

Gamma Index Distance: 0.3
distance in cm

Figure 2.29: Screen captures of the web application of the QA computational tool. (A) Data uploading. (B) Parameter setting. (C) Result Review.

2.7.3 Patient Quality Assurance Results

We demonstrate the clinical utility of our GPU-base MC QA tool using a typical IMRT prostate cancer case and a VMAT brain cancer case. The plan dose and the MC based SD and DD are displayed on an axial CT slice in Figure 2.30 and Figure 2.31 together with the γ-index maps for three pairs of comparisons. Table 2.7 summarizes the γ-index results in low dose region within 10% isodose line for three pair comparisons with 3%-3mm criteria. Very good agreements between SD vs PD, SD vs DDC and DD vs PD for both cases have been observed. Please note that both the IMRT and the VMAT plans have already been through a QA process in our clinic and have been delivered to patients. Hence the plan calculation accuracy and machine deliverability have already been ensured. Table 2.8 lists the computation time for obtaining the dose distributions using MC simulations and the three pairs of γ-index comparisons for both cases. With the use of the web application, the whole process from data upload to viewing results and downloading report takes less than five minutes and the efficiency of this tool is well suitable for clinical uses.

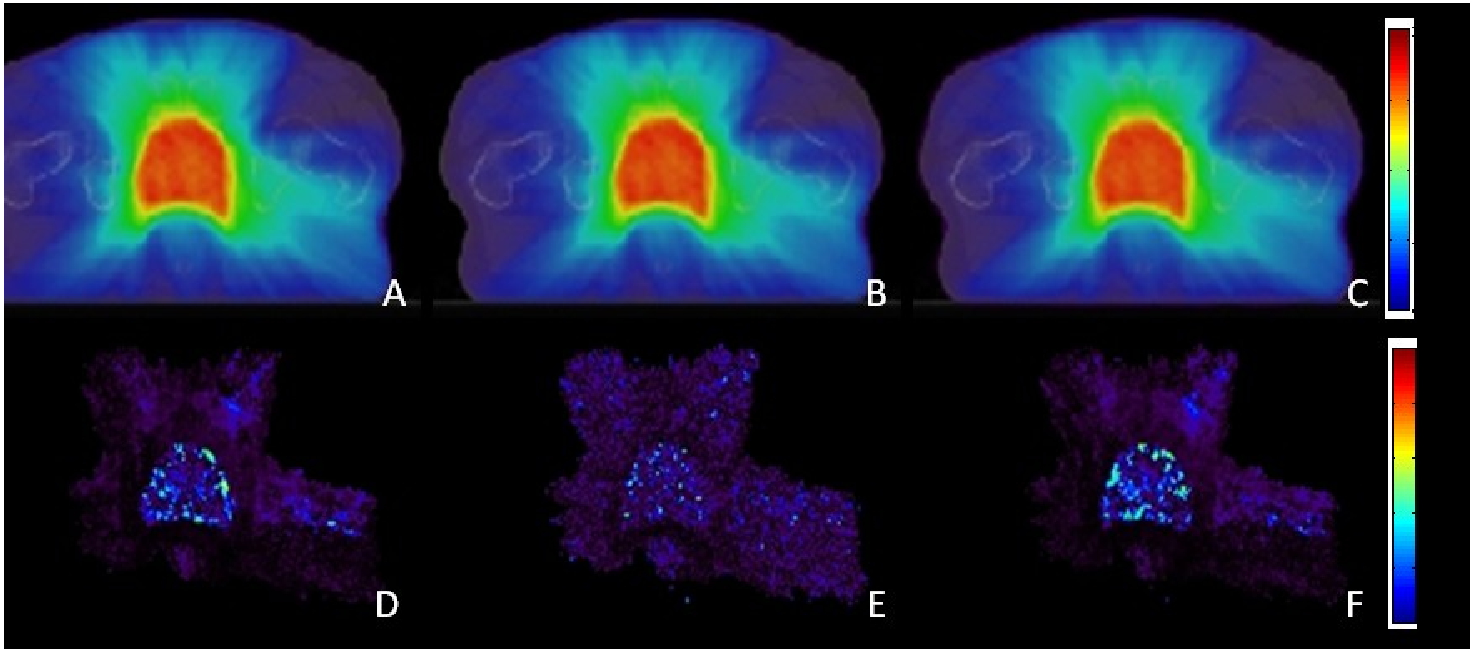

Figure 2.30: Dose distributions for a IMRT prostate case (A) Secondary dose (SD) (B) Delivered dose (DD) (C) Plan dose (PD). γ-index map for (D) SD vs. PD (E) SD vs. DD (F) DD vs. PD.

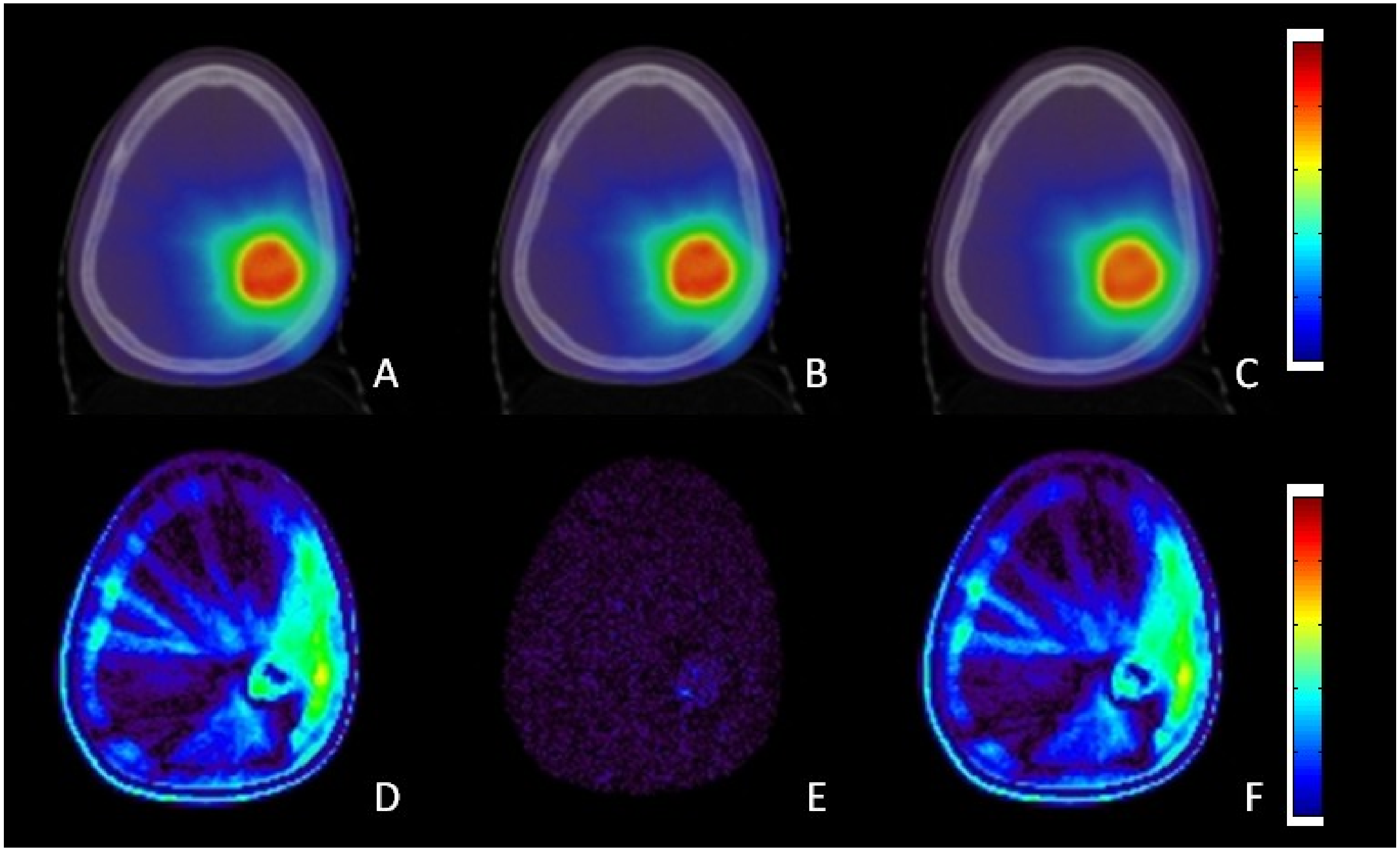

Figure 2.31: Dose distributions for a VMAT HN case (A) Secondary dose (SD) (B) Delivered dose (DD) (C) Plan dose (PD). γ-index map for (D) SD vs. PD (E) SD vs. DD (F) DD vs. PD.

Table 2.7: γ-index result for three pairs of dose comparisons.

	SD vs PD		SD vs DD		DD vs PD	
	Mean γ	Passing Rate (%)	Mean γ	Passing Rate (%)	Mean γ	Passing Rate (%)
HN	0.34	99.0	0.05	100.0	0.34	98.9
Prostate	0.18	99.3	0.09	99.9	0.24	99.5

Table 2.8: Computation time in seconds for MC simulations and γ-index comparisons.

	MC Simulation		γ-index Comparisons		
	SD	DD	SD vs PD	SD vs DD	DD vs PD
HN	35.7	38.0	2.6	1.5	2.4
Prostate	25.4	27.6	2.1	1.2	2.2

2.8 Summary

In this chapter, we have developed a fast and accurate computation tool for the patient-specific QA purpose. At the center of this tool is a GPU-based MC dose calculation engine. It was first developed by Jia X, *et al* (2011) by implementing a MC dose calculation code, called dose planning method, on the GPU platform to achieve high computational efficiency, while maintaining the dose calculation accuracy. Other modules necessary for the streamline of the QA process have also been developed.

First, we have investigated the impacts of MC noise on plan QA and developed a denoising module to post-process the MC calculated doses. We have found that the statistical uncertainty in MC dose leads to biased results for a commonly used dose comparison matrix, γ-index. Both theoretical modeling and simulation experiments using clinical patient cases have demonstrated that MC statistical fluctuation in the reference dose tends to overestimate the γ-index, while that in the evaluation dose tends to underestimate the γ-index, when the original γ-index value is relatively large. Moreover, simulation studies show that, when the reference dose and the evaluation dose are both from MC simulations, the gamma passing rate increases when the statistical noise in the evaluation dose increases. It decreases when the statistical noise in the reference dose increases. To mitigate the impacts caused by the MC uncertainty, a GPU based denoising algorithm is proposed to reduce the noise level in MC calculated dose distributions. This denoising method is implemented as an optimization problem. Noise property from a Poisson distribution is considered in our approach. Numerical experiments show that this method is able to reduce the 2% noise level in a MC dose distribution to about 0.15% noise level without prolonging simulation time.

The second module is a LINAC point source model used in MC simulations particularly designed for the QA tool. This source model contains three main factors: a source energy spectrum to model the penetration property of the beam, a beam fluence to model the "horn effect", and an output correction factor to compensate the omitted scatter components in a real LINAC. The commissioning process is very straightforward and requires only a small set of clinical beam measurements. No knowledge about the LINAC head geometry details is needed. The source energy spectrum is obtained by a manual adjustment of each energy bin weights and the beam fluence and the output correction factor are achieved automatically. We have validated the source model accuracy by comparing the MC calculated dose distributions using our proposed model and that using the most accurate phase-space file source model. Over 99% of the voxels within the high and the low dose regions pass 2%/2mm criteria in γ-index evaluations. These results clearly show that the accuracy of our source model is sufficient for the QA purpose.

The last module is fluence map generation, which computes a fluence map specific to a treatment plan or a delivery process. MLC geometry and transmission properties have been modeled. The plan fluence map is derived from MLC leaf sequence stored in a DICOM file, while the actual delivered fluence map is obtained from machine delivery information recorded in trajectory log files.

With all the modules in our QA tool, we have built a system that employs the GPU based MC dose engine to perform an independent plan dose calculation (secondary dose (SD)) and delivery dose reconstruction (delivered dose (DD)) using the planned fluence maps and the delivered fluence maps, respectively. The TPS plan dose calculation accuracy can be verified by comparing SD and plan dose, while the machine deliverability is checked by DD-SD comparison. The comparison between DD and plan dose shows the cumulative errors from both the plan dose calculation inaccuracies and the beam delivery errors. Meanwhile, a web application is developed to facilitate the clinical utilization of our QA tool. This user-friendly web application allows users to upload the data, to run the QA tool remotely on a GPU server, and to view and download the QA results.

Chapters 2 contains material published in Physics in Medicine and Biology 2013. Graves, Yan J.; Jia, X.; Jiang, Steve B., IOP Publishing. The dissertation author was the primary investigator and author of this paper. Chapters 2 also contains material being prepared for submission to Physics in Medicine and Biology. Graves, Yan J.; Folkerts, M.; Kim, G.; Teke, T.; Popescu, I. A.; Cerviño, L.; Jia, X. and Jiang, Steve B. 2013. The dissertation author was the primary investigator and author of this manuscript.

3. Physical Quality Assurance Phantom

3.1 Overview

It is desirable to incorporate ART into modern radiation treatment to overcome the problem caused by inter-fractional anatomy variation in order to achieve the optimal treatment quality (Yan *et al.*, 1997; de la Zerda *et al.*, 2007; Lu *et al.*, 2008). However, before being fully integrated into routine clinical practice, the novel ART technology should undergo a comprehensive QA procedure to ensure its quality and feasibility. So far, the QA procedure and clinical tools for ART are not well established compared to various commercially available clinical tools for other mature technologies, such as IMRT QA, let alone the QA guidelines

One core component in ART procedure is DIR, which play an important role for its success. It is hence of central importance to QA the performance of DIR algorithms. In the past, several deformable phantoms have been developed to validate the accuracy of DIR algorithms (Kashani *et al.*, 2007;

Serban *et al.*, 2008; Kirby *et al.*, 2011; Kirby *et al.*, 2013). However, none of them provides any dosimetry verification information and hence cannot serve as an end-to-end ART QA phantom. With the increased interests in the implementation of ART in clinics, an ART QA phantom which could be used for both DIR algorithm accuracy test and delivered dose verification is in high demand (Yan, 2008).

To solve this problem, we have developed a deformable phantom with a real HN patients' geometry, that also has in-vivo dosimetry capability. In this chapter, we will first present the design of this physical phantom and its fabrication process in Section 3.2 and the phantom property in Section 3.3. In Section 3.4, we will discuss the diode dosimeter. The DIR accuracy test and its result are presented in Section 3.5, while the experiment and results of ART dosimetric verifications are in Section 3.6.

3.2 Design and Fabrication

3.2.1 Phantom Design

It is common for a head and neck cancer patient to experience tumor and normal tissue changes during the course of radiation treatment. These changes can be dramatic, including shrinkage of primary tumor and parotid glands, medial shift in parotid glands, and alterations in body contours due to weight loss (Barker *et al.*, 2004). Hence we choose the HN cancer patient case as a representative site.

The geometrical content of this phantom is determined based on a single CT slice of a typical HN cancer patient who most likely requires ART during their treatment (Figure 3.1(A)). The key anatomic components to be modeled in this slice are tumor, parotids, pharynx, mandible, spinal cord, skin and soft tissue, including dense soft tissue (i.e. muscle) and light soft tissue (i.e. fat). The PTV and the parotids contours are displayed on the patient CT slice in Figure 3.1. To make the phantom realistic, the materials are selected such that they have x-ray attenuation coefficients similar to those in the human body. These deformable tissues are sandwiched between two parallel acrylic plates. Inside the tissue, a balloon catheter acts like a tumor, such that the deflation of the balloon by injecting various amount of saline water simulates the tumor variations. Small glow-in-dark nonradiopaque marker dots are glued on the two sides of the deformable material surfaces. These markers don't appear on CT images but are visible in optical camera images through the acrylic plates, based on which the tissue deformation ground truth can be derived.

As a HN ART QA phantom, the in-vivo measurements of interest are the dose to the normal organs, i.e. mandible, cord and parotid, especially the one near the tumor, and the dose inside the PTV. To acquire these doses, we select the SRS diode as our detector. The details of the SRS and its properties will be presented later. To hold the diode inside the phantom, a detector holder is designed particularly for the diode dimension. We have selected four measurement locations of interest. *diode 1* is near the mandible, *diode 2* is inside the cord, *diode 3* is inside the PTV, and *diode 4* is inside the left parotid. Since there is negligible deformation from tumor shrinkage near the mandible or inside the cord, the detector holders for *diode 1* and *diode 2* are fixed inside the local tissue. In contrast, *diode 3* and *diode 4* should move with tissue deformation, when the simulated tumor shrinks. To allow for the movement of these diodes inside the phantom, we have designed rails for the detector holders, shown in Figure 3.2. Specifically, the tissue deformation directions from the tumor shrinkage at *diode 3* and *diode 4* locations are estimated and then the rail tracks are installed along these directions in the acrylic plates, so that the detector holders are guided and can move along the rails inside the phantom. The construction diagram with the marked diode detector locations and rail trackers is shown in Figure 3.1(B)

This phantom is designed to have a thickness of 4.5 cm along the superior-inferior (SI) direction. But its content remains unchanged among different transverse planes and the deformation is constrained only inside plane perpendicular to the SI direction, as will be presented below. Therefore this phantom is essentially considered a 2D one.

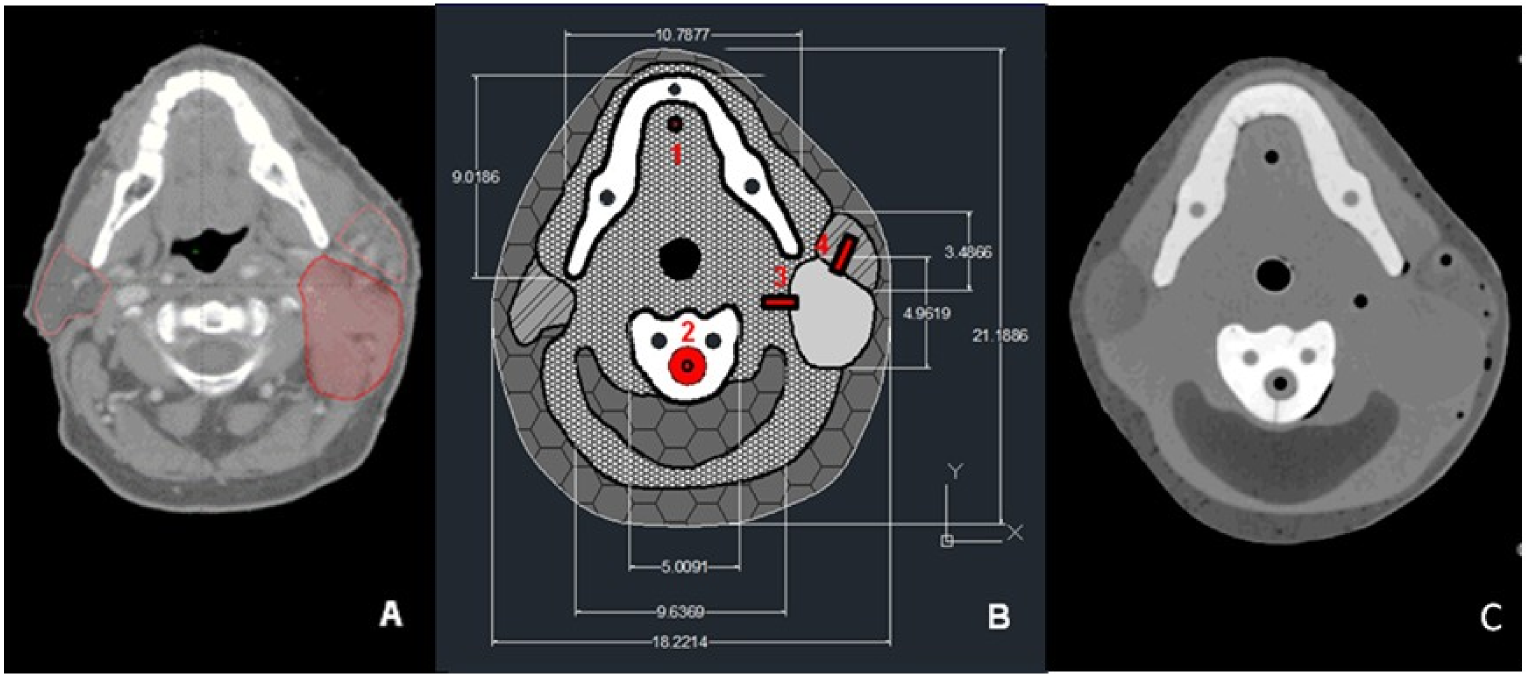

Figure 3.1: (A) CT image of a representative HN patient with PTV and parotids contours. (B) Construction diagram with marked diode holder locations and rails. The dimensions are in cm. (C) CT slice at the middle of the constructed phantom.

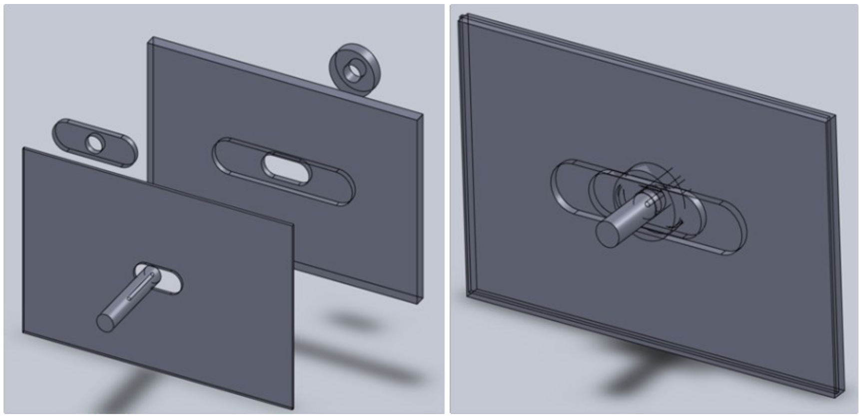

Figure 3.2: Design diagram of the diode holders on rail.

3.2.2 Material Selection and Fabrication

To make this phantom anthropomorphic, not only should the geometric contents represent a HN patient, the phantom material should also have similar X-ray attenuation properties to the tissue in a real patient anatomy. Since the HU value from a CT scan is directly related to the material linear attenuation coefficient, we utilize a GE CT scanner (GE Four-Slice Qxi LightSpeed CT, GE Healthcare, USA) to scan different sample materials, as shown in Figure 3.3, and then choose the ones with HU values close to the values for patient anatomy components. Besides the material for major anatomic contents, the construction components, such as the supporting bolts, detector holders and rails cannot have metal components to avoid metal artifacts seen in CT images.

As such, gypsum plaster is used for casting the bony anatomy, i.e. mandible and spine, and they are rigidly attached to the acrylic plates with small size nylon bolts. Soft tissue is made of highly flexible silicone rubber. The base silicon rubber represents the dense soft tissue. Micro-balloon filler is added into silicon rubber gel to create lighter weight casting. Parotids and light soft tissue are mixtures of base silicone gel with 10% and 20% micro-balloons filler, respectively. The soft tissue and parotids solidifies around the bones with a nylon tube in the pharynx position to create an air cavity. Urethane rubber is painted on the soft tissue surface to simulate skin. A latex balloon catheter filled with saline water acts as a tumor. The balloon catheter is connected to a plastic tube that passes through the acrylic plate. A syringe is attached to the plastic tube so that the balloon volume can be adjusted by modifying the amount of saline water injected. The concentration of the water inside the balloon is adjusted to have a similar HU value to the surrounding tissue. On the two sides of deformable material surfaces, small glow-in-dark nonradiopaque marker dots are glued to form a 2D grid with approximately 1.5cm spatial resolution. Middle size nylon bolts are installed at the four corners of the acrylic plates to hold the deformation tissue in place and four glow-in-dark markers are also glued on the bolt tops as calibration markers to assist optical image distortion correction and CT to optical images alignment. In addition, a water based lubricant is applied to the acrylic plates to reduce friction between the plates and deformable material surfaces. The diode holder is made of acrylic and fits to the diode with 2mm tube thickness. All the components for detector rail trackers are made of plastic. Since the radiation sensitive area is at the tip of the diode, the diode holder is constructed such that, when the diode is in place, its tip aligns with the middle plane of the deformable phantom.

Figure 3.3: CT scanning for different dense tissue material samples.

3.3 Phantom Properties

The prototype of this deformable HN phantom is presented in Figure 3.4. The orange latex balloon, which mimics the tumor, is easily seen through the acrylic plate. The deformable phantom consists of six materials that represent bone, shrinking tumor, air cavity, parotids and soft tissue including light and denser tissue. Figure 3.1 displays a comparison between the CT slice at the middle of the deformable phantom, the represented HN patient CT, and the phantom design diagram. From the CT slices, the geometry of each of the components is easily observed, and the anatomic relationships of the phantom are similar to that of the patient. The average HU values for bone, dense and light soft tissue, and parotids from the phantom and the representative HN patient are summarized in Table 3.1. For each component material, we are able to reproduce similar HU values to that in the real patient.

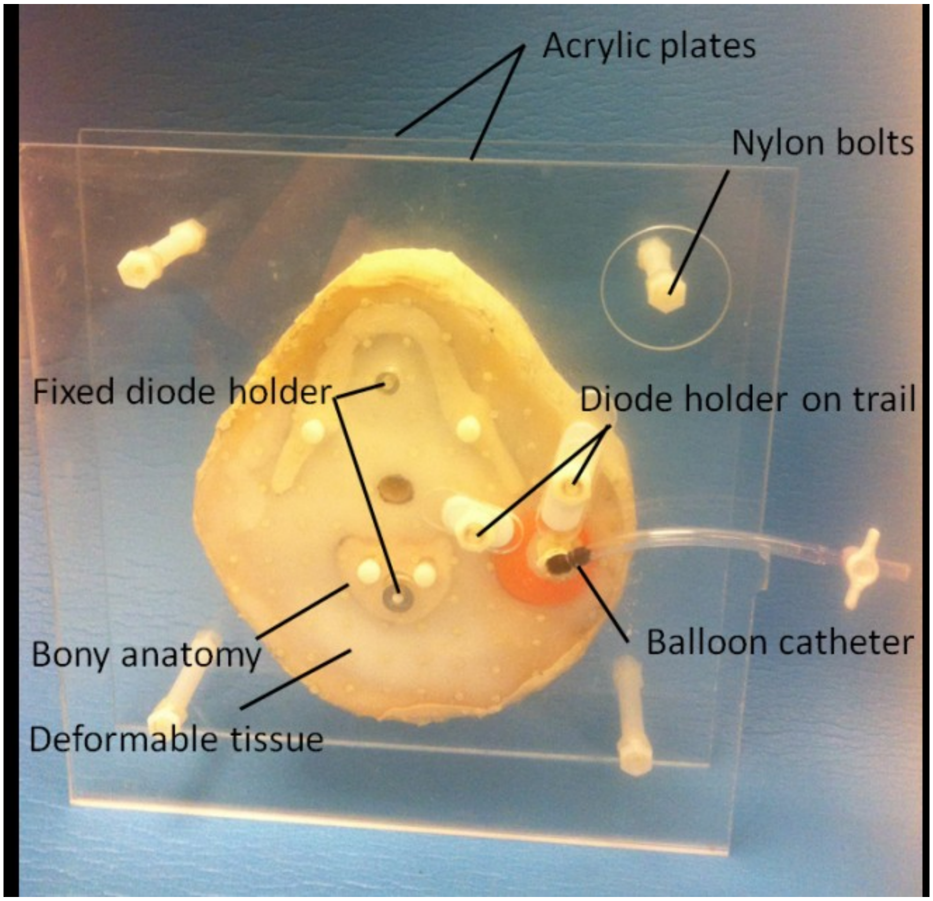

Figure 3.4: Prototype of the deformable HN phantom.

Table 3.1: Average HUs for phantom and patients' anatomic components.

Components	Bone	Dense soft tissue	Light soft tissue	Parotids
Phantom	865	140	-35	9
Patient	920	100	-50	65

3.4 Radiation Diode

Figure 3.5 presents a SRS diode that we select as the in-vivo dosimeter. It is an unshielded p-type silicon diode with 5mm diameter. Because of its small size, it is commonly used for small field photon beam measurement (i.e.<5x5cm^2).

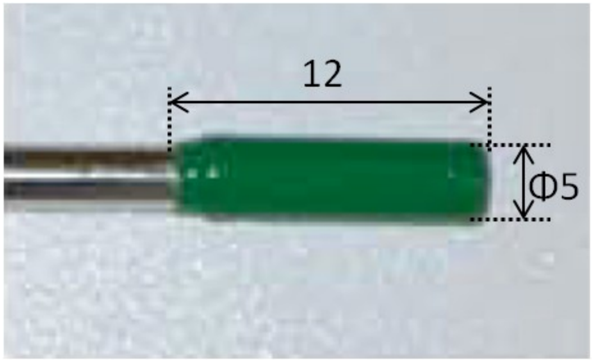

Figure 3.5: SRS diode. Dimensions are in mm.

3.4.1 Angle Dependence Property

A conventional setup for the diode is to align its cylindrical long axes parallel to the beam axis. However, in our application, the diode is inserted into the phantom such that its long axes is perpendicular to the beam axis. Hence, before adopting this setup, the angular dependence of this diode performance should be evaluated. A calibration procedure should also be performed for absolute dose measurements.

The angle dependence is defined as the response of the diode to different beam angles around the diode’s long axis under the isocentric condition, normalized to the reference response. The reference condition refers to the isocentric setup with beam angle at zero degrees. In our experiments, an acrylic buildup cap, shown in Figure 3.6(A) is designed and built for this investigation to increase dose depositions to the diode.

The reference response is obtained when 100 MU radiation is delivered with a 5x5cm^2 field size. Different diode responses with 100 MU radiation from 7 evenly distributed angles (i.e. at 0, 51, 102, 153, 207, 258, 309 degrees) are measured and are normalized to the reference response. The beam angles with respect to the orientation of the diode is illustrated in Figure 3.6(B). Figure 3.7 shows the isocentric setup for the diode to obtain the reference response.

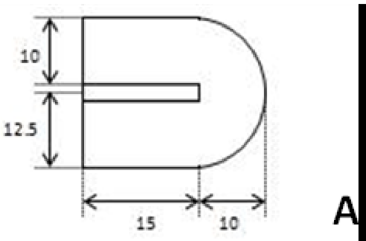

Figure 3.6: (A) Diagram of the buildup cap. Measurements are in mm. (B) Orientation of beam angles with respect to the diode.

Figure 3.7: Isocentric setup to obtain the diode symmetry property.

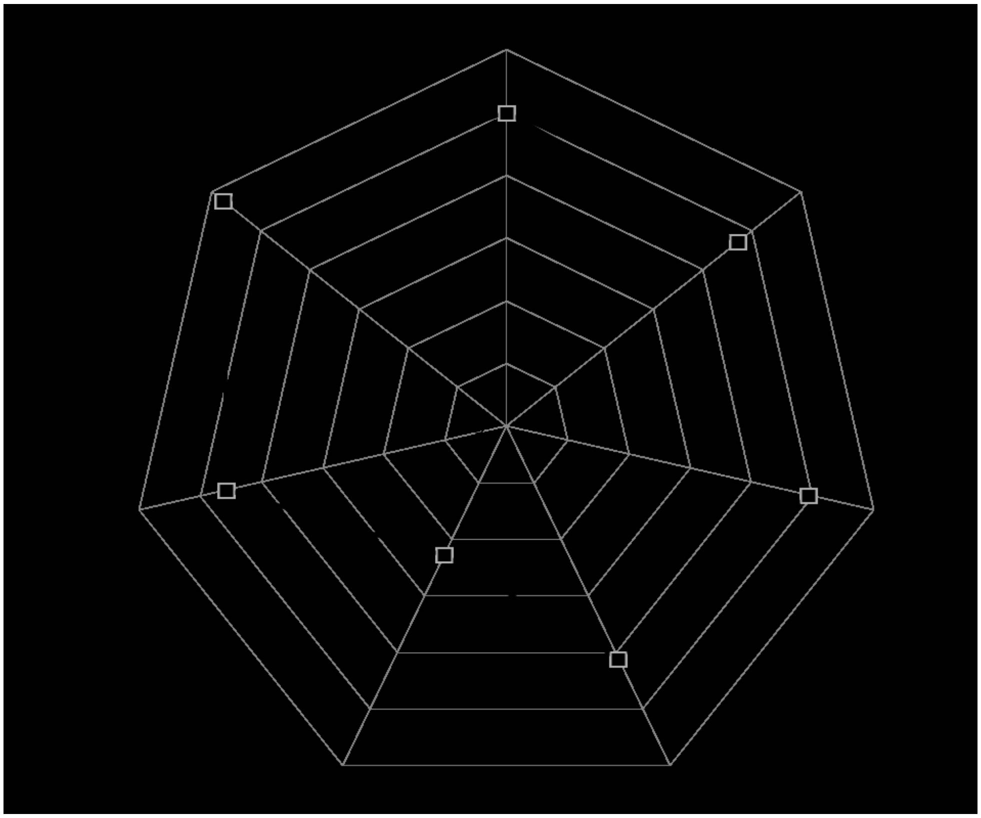

Figure 3.8: Graph of diode response at different angles against response at zero degree gantry angle.

The responses are averaged from two rotations of radiation beam delivery and the results values are plotted in Figure 3.8. The greatest asymmetry appears at 207 degree angle, at which the response is 1.36% lower than the reference value. Derivations from the reference response at other angles are within 0.5%. Because of the low angular dependence of the diode response, we will ignore this issue when using it for in-vivo measurement inside of the phantom with its long axes being set perpendicular to the beam axis.

3.4.2 Dosimetry Calibration

Before we conduct dosimetric validations using the SRS diode, we need to calibrate the diode dosimeter reading. Specifically, the diode calibration is performed at the isocentric condition for a 10x10cm^2 field size at 10cm depth in a solid water phantom. The long axis of the diode is perpendicular to the beam axis and the tip of the diode is aligned with the isocenter. The electrometer reading R_0 of the diode under a 100 MU 6MV beam radiation is recorded. Then the calibration factor f_{cal} is obtained, which converts the electrometer reading to dose in water :

$$f_{cal} = \frac{D_0}{R_0}, \tag{3.1}$$

where R_0 and D_0 are the electrometer reading and dose to water at the calibration condition. Here, D_0 can be easily obtained, since the dose to water under the setup in our experiments is well studied in external beam calibration process. It is also found that the diode sensitivity slightly depends on the radiation history. Therefore, the diode is frequently calibrated every time right before a dosimetric verification experiment. Once the calibration coefficient f_{cal} is obtained, in a dose measurement, we can obtain the absolute dose value D_m as:

$$D_m = f_{cal} \times R_m \,, \tag{3.2}$$

where R_m is the electrometer reading of the diode response in the measurement.

3.5 Deformable Image Registration Algorithm Accuracy Test

To represent the original large tumor volume, 160ml salt water is injected into the latex balloon catheter using a syringe. Optical camera images with a pixel size of 0.33mm are acquired in the dark. To simulate the tumor shrinkage, we deflate the balloon volume to 65ml and the diode 3 and diode 4 holders move towards to the tumor’s center with the tissue deformation. Again, optical images of the surface markers are acquired with the camera location the same distance as that for the original large tumor geometry. An example of the optical images is shown in Figure 3.9. In addition, two sets of CT images are obtained for the phantom before and after the deformation using the GE CT scanner. The CT image resolution is 0.98mm and the slice thickness is 2.5mm.

The grids of small nonradiopaque markers on the deformable phantom surface provide the ground truth to verify the accuracy of the DVFs calculated from DIR algorithms. An in-house program is developed to detect the physical marker dots in the optical images taken before and after the deformation. This is achieved by applying a threshold value in the green channel of the RGB optical images. After that, we set the origin of a 2D coordinate at the calibration marker on the anterior-right corner of the image. *y* and *x* denote the patient's anterior and left directions, respectively. The calibration markers on the nylon bolts are known to form a square with 29.7cm size. This information is then used to interpolate the x and y coordinates of the initial and final centroid positions of the surface marker dots from the optical images to correct for any camera geometry distortion. Finally, the deformation motion vectors are obtained from the phantom surface markers and are considered as the measured deformation ground truth, denoted by $\overrightarrow{v_m}$.

To test the accuracy of a DIR algorithm, the measured deformation is compared to the DIR calculated DVFs. As such, the vectors at 94 marker locations are extracted from the calculated vector field, denoted as $\overrightarrow{v_{cal}}$. The average error between the measured deformation and the calculated one is used to characterize the algorithm accuracy as

$$\delta = \frac{\sum_{i=1}^{94} \left| \overrightarrow{v_{i,m}} - \overrightarrow{v_{i,cal}} \right|_2^2}{N}, \tag{3.3}$$

where N=94.

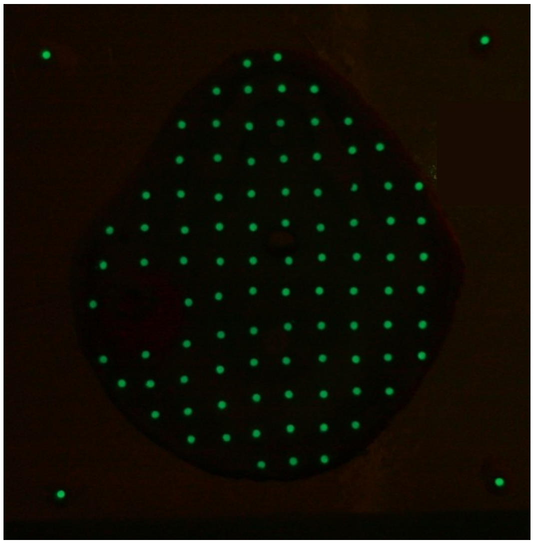

Figure 3.9: Example of the optical image of the markers in dark.

3.5.1 Overview of Demons Algorithm

In this dissertation, we select a GPU based demons algorithm (Gu *et al.*, 2010) as our tested DIR algorithm example. The basic idea of demons algorithm is to register the *moving image* $I_m\,(x)$ and the *reference image* $I_r\,(x)$ by a vector field $v(x)$ which relates the two images by $I_m\left(x+v(x)\right)=I_r\,(x)$. $v(x)$ is solved in an iterative fashion, where the incremental displacement vector $\mathrm{d}\mathbf{r}\,(x)$ is determined based on the image intensity at the voxel x in each iteration step. There are six variants of the demons algorithm and they differ from each other in the way of calculating $d\mathbf{r}\,(x)$. In this test, we choose to use the double force demons where $\mathrm{d}\mathbf{r}$ is defined as:

$$d\mathbf{r}^{(k+1)}=\frac{\left(I_m^{(k)}-I_r\right)\nabla I_r}{\left(I_m^{(k)}-I_r\right)^2+|\nabla I_r|^2}+\frac{\left(I_m^{(k)}-I_r\right)\nabla I_{\mathrm{m}}^{(\mathrm{k})}}{\left(I_m^{(k)}-I_r\right)^2+\left|\nabla I_{\mathrm{m}}^{(\mathrm{k})}\right|^2}, \qquad (3.4)$$

where the $I_m^{(k)}$ and I_r are the intensities of the moving image at the kth iteration and the original reference image, respectively.

However, we would like to emphasize that the main focus of this study is not to investigate the demons algorithm accuracy but to demonstrate the feasibility of utilizing our phantom for the DIR algorithm accuracy test.

3.5.2 Algorithm Performance

The CT slice of the middle of phantom is used in the demons algorithm to calculate the DVF. As such, the CT slice with the large tumor before the shrinkage is considered as the reference image and that with the small tumor is the moving image. The moving image (Figure 3.10(B)) is registered to the reference image (Figure 3.10(A)) to produce the deformed image (Figure 3.10(C)). The demons performance is qualitatively evaluated by comparing the difference image between the reference and the moving images (Figure 3.10 (D)) with the difference image between the reference and the deformed one (Figure 3.10 (E)). After the deformation, the intensity in the difference image is greatly reduced and the mean pixel difference drops from 2% to 0.038% of the maximum reference image intensity, indicating the accuracy of the registration. Figure 3.10 (F) displays the generated deformation vector fields overlaid on the reference image.

The detected grow-in-dark surface markers before and after the tumor shrinkages are shown in Figure 3.11(A) and (B). We have also plotted the centroid positions of the markers overlaid on the reference CT image in Figure 3.11(C), with the initial positions of the markers in red, the final positions in green. A marker motion vector field is also drawn in blue by connecting the initial and the final locations of each marker. A good visual agreement between the measured deformation and the DIR output shown in Figure 3.11(D) is observed. The quantitative difference of the vector field is also summarized in Table 3.2. The average error magnitude at the 94 surface markers is 2.1mm. It is also found that there exists larger variance for left-right (LR) direction than for the anterior-posterior (AP) direction.

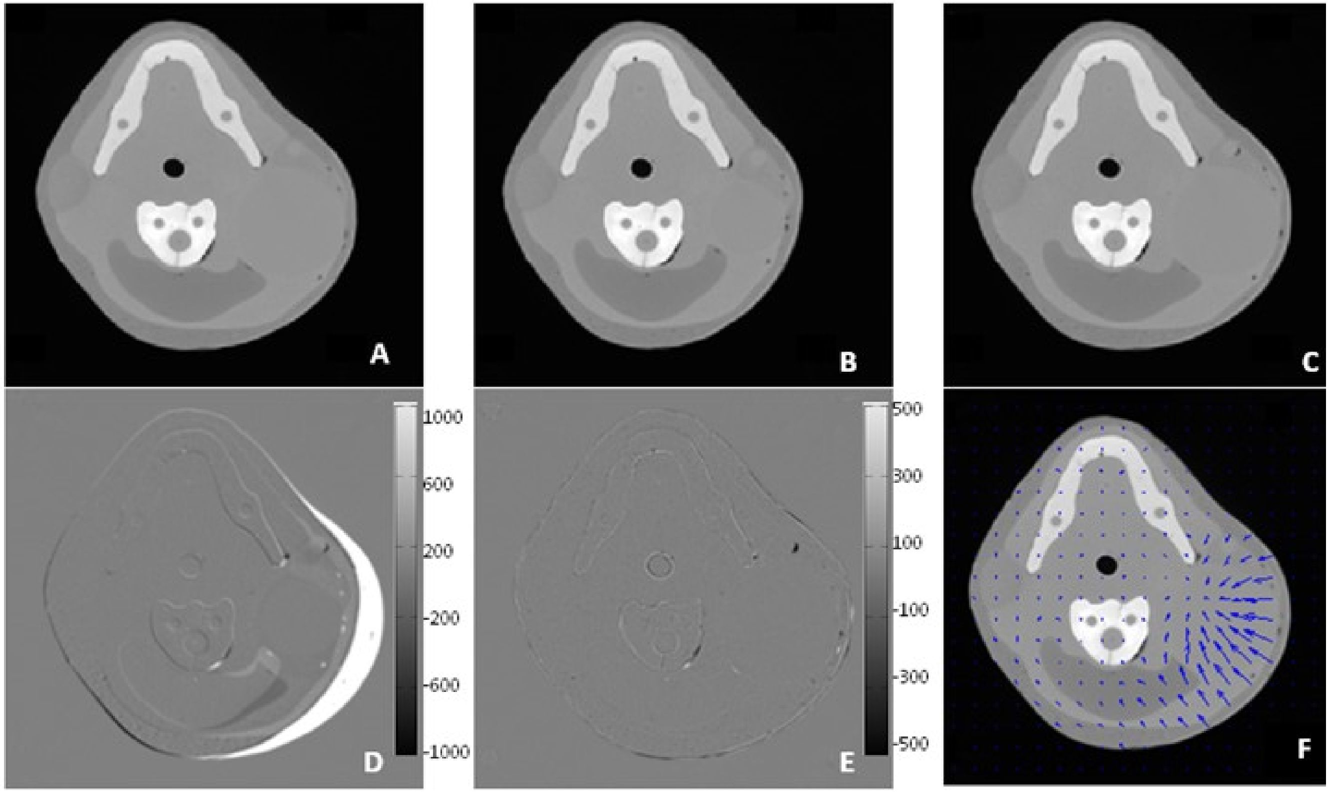

Figure 3.10: Images of demons algorithm. (A) Reference image. (B) Moving image. (C) Deformed image. (D) Difference image between the reference and moving images. (E) Difference image between the reference and deformed images. (F) Generated deformation vector filed overlaid on the reference image.

Table 3.2: Mean and standard deviation of the average error for DIR calculated deformation vectors compared with the measured deformation vectors.

AP (mm)	LR (mm)	δ (mm)
1.0±1.0	1.5±2.0	2.1±2.2

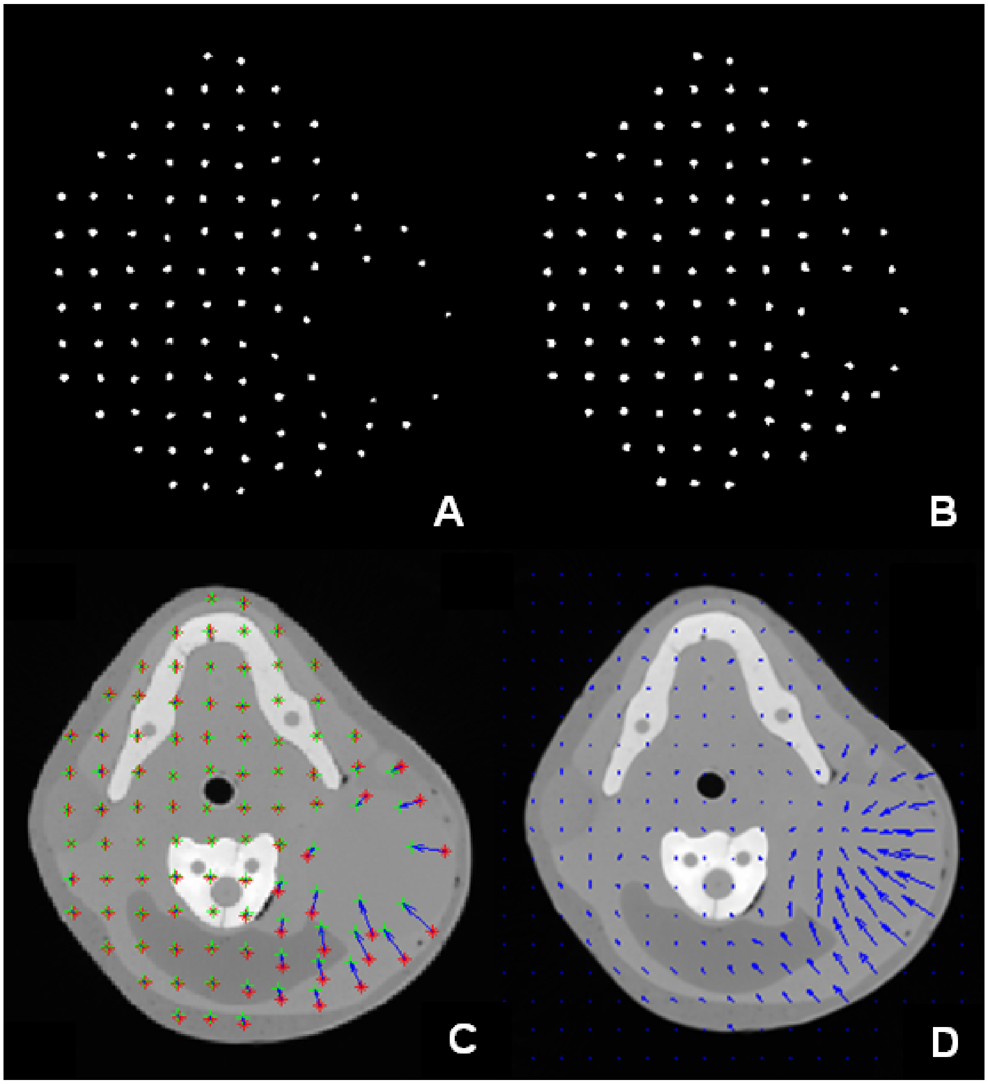

Figure 3.11: (A) Initial marker positions. (B) Final marker positions. (C) Initial and final marker position with the measured deformations overlaid on the reference CT image. (D) Generated deformation vector filed overlaid on the reference CT image.

3.6 Adaptive Radiotherapy Dosimetry Verification

To use this phantom as an end-to-end test for ART QA, this deformable phantom is treated exactly in the same way as for a real patient, going through initial CT scan, treatment planning, plan delivery, geometry deformation, re-CT scan, re-planning and re-plan delivery procedure.

First, after the CT image is acquired for the phantom with a large tumor geometry (160ml salt water into the latex balloon), the PTV and organ contours are drawn. We deliberately extend the tumor contour to include *diode 3* inside the PTV, so that the diode provides the dose measurement inside the PTV target. Then an IMRT plan with a set of seven co-planer equiangular 6MV beams are generated on the large tumor geometry using Eclipse (Varian Medical Inc., Palo Alto, CA) treatment planning system, with clinically relevant constraints to organs satisfied. After the phantom is properly set up on the treatment couch using the on-board CBCT system for image guidance, the plan is delivered to the phantom and the four diode readings are obtained and compared to the calculated results from the TPS. After the tumor shrinkage (60ml salt water into balloon), the PTV and organ contours are re-drawn in the new CT image. Figure 3.12 shows PTV and organ contours on both geometries. With the same beam angles and plan constraints, the new geometry is used for re-planning in Eclipse. Then both the new plan and the initial plan are delivered to the new phantom geometry to evaluate the dosimetric gain from ART re-planning. The diode readings are compared with the calculation from Eclipse to verify the ART accuracy. The calculated dose of the new plan irradiated on the small tumor geometry is transferred back to the large one given the DVFs derived from the demons algorithm and is added to the initial plan dose. The summation of the diode measurements of the initial plan radiated to the large tumor geometry and that of the new plan delivered to the small tumor geometry is then used to verify the dose accumulation calculation accuracy.

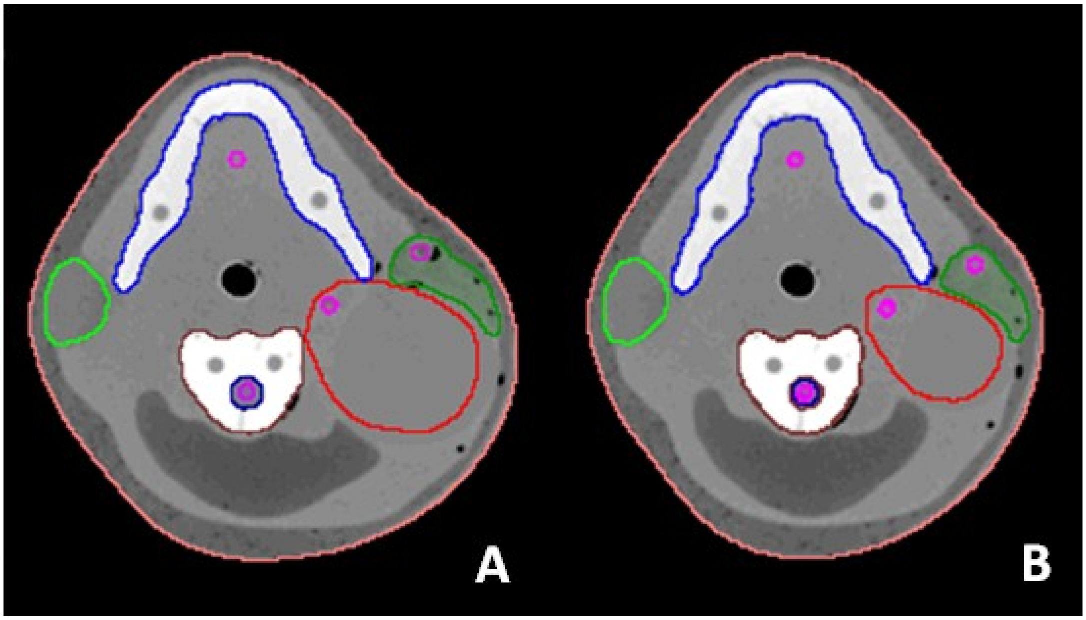

Figure 3.12: PTV and organ contours. (A) On the large tumor geometry. (B) On the small tumor geometry.

3.6.1 Experiment Results

To evaluate the dosimetric influence from the tumor shrinkage, we deliver the initial optimized plan to the large tumor geometry as well as to the small tumor geometry; here we name them as *delivery I* and *delivery II*. After we obtained the re-plan, we deliver the re-plan to the new small tumor geometry to study the dosimetric gain from ART re-planning; here we name it *delivery III*. Table 3.3 summaries the dosimetry results from three radiation deliveries. D_m and D_c present diode measurements and TPS plan calculations. The values are converted into a unit of percentage of the prescribed dose. A good agreement, with a maximum difference of 3.1%, is obtained between the diode measurements and plan calculations. The point dose to the parotid (*diode 4*) is dramatically increased when the original plan is delivered to the new small tumor geometry phantom due to the parotid shift into the high dose area after tumor shrinkage. This dose is greatly decreased when the re-plan is applied, indicating the necessity of ART in this situation. This is consistent with the observations on DVHs shown in Figure 3.13. When the initial plan is applied to the new geometry, increase of doses to organs is observed. With the re-optimized plan for the new geometry, the organ doses are brought back to low levels, particularly for the left parotid. This observation also agrees with the diode measurements and plan calculations for the lower point dose to organs (*diode 1, diode 2 and diode 4*) in *delivery III* compared to *delivery II*. In addition, good matches between the calculated values and the measurements are also obtained in terms of accumulating dose from *delivery I* and *delivery III* to a reference geometry, i.e. the large tumor geometry in our study. The quantitative results are summarized in Table 3.4.

Table 3.3: Plan calculations and diode measurements (and the absolute difference) in percentage of the prescription dose before and after deformation with the original plan and the re-plan irradiated.

Dose	Diode 1 $D_c \mid D_m$	Diode 2 $D_c \mid D_m$	Diode 3 $D_c \mid D_m$	Diode 4 $D_c \mid D_m$
Delivery 1	72.6 | 74.9 (2.3)	42.9 | 46.0 (3.1)	103.0 | 105.1 (2.1)	35.5 | 35.6 (1.0)
Delivery 2	71.6 | 73.8 (2.2)	44.0 | 47.1 (3.1)	106.8 | 108.8 (2.0)	49.5 | 49.5 (0.0)
Delivery 3	57.7 | 59.7 (2.0)	36.6 | 37.6 (1.0)	102.1 | 103.8 (1.7)	29.9 | 32.0 (2.1)

Table 3.4: The plan calculation and diode measurements (and the absolute difference) in percentage of prescription dose for accumulative dose from delivery 1 and delivery 3.

Diode 1 $D_c \mid D_m$	Diode 2 $D_c \mid D_m$	Diode 3 $D_c \mid D_m$	Diode 4 $D_c \mid D_m$
64.8 | 67.3 (2.5)	38.8 | 41.8 (3.0)	102.4 | 104.5 (2.1)	32.2 |33.8 (1.6)

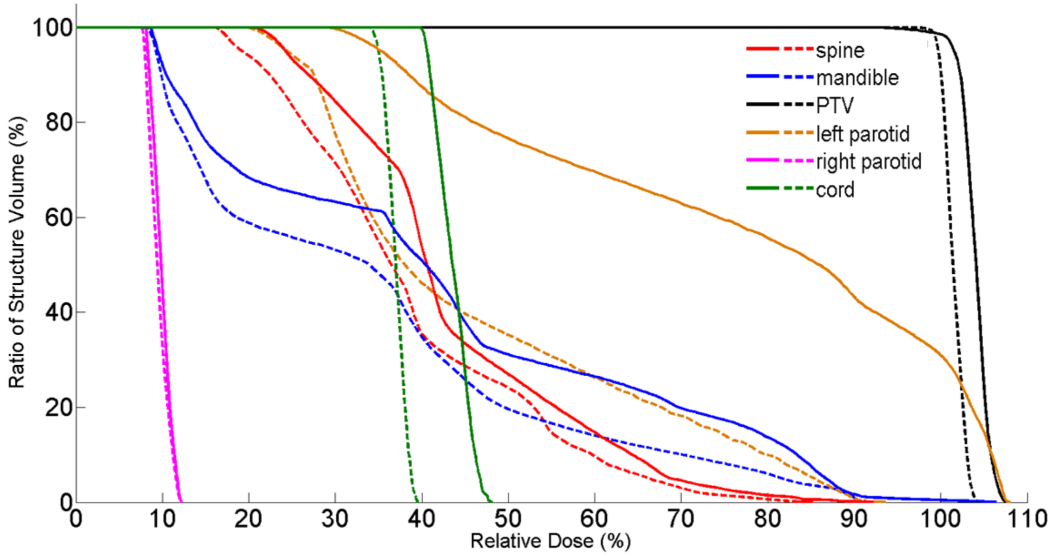

Figure 3.13: DVH plots of initial optimal plan on new small tumor geometry (solid lines) and re-plan on new tumor geometry (dash lines).

3.7 Discussion and Conclusions

In this chapter, we have presented the design and construction of a deformable HN phantom. This phantom consists of six anatomic components that resemble a real HN patient geometry with accurate HU numbers. The nonradiopaque surface markers, which do not influence DIR algorithms, provide the deformation ground truth. A quantitative error analysis is performed to evaluate the DIR accuracy using the physically measured deformation from the surface markers and the calculated deformation fields using the demons algorithm. The homogeneous phantom tissue regions present a challenge to the demons algorithm because this algorithm is an intensity based DIR algorithm, where the registration is more accurate in high contrast regions. However, most of the surface markers lie within the homogeneous tissue region, the obtained average deformation error is 2.1mm. The main focus of this study is not to investigate the DIR algorithm but to utilize the surface markers for the accuracy test, so future study will be carried out to comprehensively compare a set of DIR algorithms' accuracy using this deformable HN phantom.

We also demonstrate the feasibility of using this deformable phantom as an end-to-end ART QA phantom, going through all the ART treatment steps. It is found that the dose to parotid significantly increases when the original plan is delivered to the small tumor geometry phantom, because the parotid shifts into the high dose area due to tumor shrinkage. In contrast, the dose to parotid dramatically decreases, when the re-optimized plan is applied. This indicates the necessity of ART in this situation. The in-vivo diode dosimeters provide point dose measurements and the results match with the calculated dose from the planning system, with a maximum 3.1% absolute difference in the unit of percentage of the plan prescription dose. The biggest point dose difference appears at the high dose gradient region which is always a challenge for any dose measurement and calculation methods. The discrepancy between the accumulative dose calculation and the diode measurements from two radiation deliveries illustrate the combination of error from the dose calculation and the DIR algorithm.

With the advancements and the clinical use of on-board image system, daily CBCT images become available for ART. Several studies demonstrate the use of CBCT for dose reconstruction and ART re-planning (Yong *et al.*, 2007; Fu *et al.*, 2009). This deformable phantom is not limited by image modality and can be a truly end-to-end QA phantom for any new ART technologies before they are implemented in clinics.

Chapter 3 contains material being prepared for submission to Physics in Medicine and Biology. Graves, Yan J.; Smith, A.; Rice, R.; Mell, L.; Jia, X.; Jiang, Steve B.; Cerviño, L. 2013. The dissertation author was the primary investigator and author of this manuscript.

4. Conclusions

The aim of radiation therapy is to deliver a prescribed amount of radiation dose to the cancer target, while maximally sparing dose to surrounding health organs. Although current treatment planning system can effectively design a high quality treatment plan to best meet this goal, a series of quality assurance tests are highly demanded to ensure the plan calculation accuracy, as well as its deliverability.

Currently, QA methods of different types for advanced IMRT and VMAT treatments have been available and are routinely employed in radiotherapy clinics. Yet, they usually suffer from issues such as high cost, intensive labor, and inaccurate calculations. This dissertation is motivated by this fact and hence, its first half is devoted to developing a computational QA tool. In Chapter 2, we have developed a fast and accurate computational tool for patient-specific QA using a GPU based Monte Carlo dose engine. Several modules necessary to the QA process have been built, including a denoising method to post-process the MC calculated doses, a LINAC beam source model with a semi-automatic commissioning process, and a fluence map generation module. A web application has been developed for the QA tool incorporating all modules to facilitate its clinical utilization. This QA tool verifies the plan dose calculation accuracy by comparing the TPS plan dose and the secondary dose calculated by the MC method, as well as checks the machine delivery errors by comparing the MC simulated secondary dose and the delivered dose reconstructed using machine log files. The accumulative error from both error sources can be checked by plan dose and delivered dose comparisons.

Another motivation of the dissertation is to develop a physical phantom for adaptive radiation therapy QA. Holding the promise of always generating the optimal treatment plan corresponding to the patient geometry at each treatment fraction, ART is gaining more and more clinical and research focus. One aspect to facilitate its clinical introduction is comprehensive QA of the ART process. To solve this problem, in Chapter 3, a physical deformable head and neck phantom with in-vivo dosimeter has been designed and fabricated. This phantom resembles HN patient geometry and simulates tumor shrinkage with a great level of realism. Our experiments have demonstrated the feasibility of using this proposed phantom to verify a DIR algorithm's accuracy by comparing the DIR calculated deformation vector field with the physically measured ground truth based on the surface markers on the phantom. This deformable HN phantom can also be utilized as an end-to-end ART QA phantom to check the ART technology accuracy by measuring the point doses to organs and PTV using diode dosimeters.

In conclusion, a computational QA tool and a physical phantom QA tool have been successfully developed in this dissertation. Comprehensive tests regarding the accuracy and feasibility of these tools have been conducted. Being preliminary studies, this dissertation presents initial results in these developments. Ongoing research work will continue improving these tools from many aspects, as well as conducting tests in real clinical contexts. We believe that the ultimate clinical implementations of these tools will greatly facilitate radiation therapy QA process, ensuring effective and safe radiotherapy treatments to every patient.

Reference

Agostinelli S, Allison J, Amako K, Apostolakis J, Araujo H, Arce P, Asai M, Axen D, Banerjee S, Barrand G, Behner F, Bellagamba L, Boudreau J, Broglia L, Brunengo A, Burkhardt H, Chauvie S, Chuma J, Chytracek R, Cooperman G, Cosmo G, Degtyarenko P, Dell'Acqua A, Depaola G, Dietrich D, Enami R, Feliciello A, Ferguson C, Fesefeldt H, Folger G, Foppiano F, Forti A, Garelli S, Giani S, Giannitrapani R, Gibin D, Cadenas J J G, Gonzalez I, Abril G G, Greeniaus G, Greiner W, Grichine V, Grossheim A, Guatelli S, Gumplinger P, Hamatsu R, Hashimoto K, Hasui H, Heikkinen A, Howard A, Ivanchenko V, Johnson A, Jones F W, Kallenbach J, Kanaya N, Kawabata M, Kawabata Y, Kawaguti M, Kelner S, Kent P, Kimura A, Kodama T, Kokoulin R, Kossov M, Kurashige H, Lamanna E, Lampen T, Lara V, Lefebure V, Lei F, Liendl M, Lockman W, Longo F, Magni S, Maire M, Medernach E, Minamimoto K, de Freitas P M, Morita Y, Murakami K, Nagamatu M, Nartallo R, Nieminen P, Nishimura T, Ohtsubo K, Okamura M, O'Neale S, Oohata Y, Paech K, Perl J, Pfeiffer A, Pia M G, Ranjard F, Rybin A, Sadilov S, Di Salvo E, Santin G, Sasaki T, Savvas N, Sawada Y, Scherer S, Seil S, Sirotenko V, Smith D, Starkov N, Stoecker H, Sulkimo J, Takahata M, Tanaka S, Tcherniaev E, Tehrani E S, Tropeano M, Truscott P, Uno H, Urban L, Urban P, Verderi M, Walkden A, Wander W, Weber H, Wellisch J P, Wenaus T, Williams D C, Wright D, Yamada T, Yoshida H and Zschiesche D 2003 GEANT4-a simulation toolkit *Nuclear Instruments & Methods in Physics Research Section a-Accelerators Spectrometers Detectors and Associated Equipment* **506** 250-303

Ahunbay E E, Peng C, Godley A, Schultz C and Li X A 2009 An on-line replanning method for head and neck adaptive radiotherapy *Medical Physics* **36** 4776-90

Antolak J A, Rosen, II, Childress C H, Zagars G K and Pollack A 1998 Prostate target volume variations during a course of radiotherapy *International Journal of Radiation Oncology Biology Physics* **42** 661-72

Armijo L 1966 Minimization of functions having Lipschitz continuous first partial derivatives *Pacific Journal of Mathematics* **16** 1-3

Bakai A, Alber M and Nusslin F 2003 A revision of the gamma-evaluation concept for the comparison of dose distributions *Physics in Medicine and Biology* **48** 3543-53

Barker J L, Garden A S, Ang K K, O'Daniel J C, Wang H, Court L E, Morrison W H, Rosenthal D I, Chao K S C, Tucker S L, Mohan R and Dong L 2004 Quantification of volumetric and geometric changes occurring during fractionated radiotherapy for head-and-neck cancer using an integrated CT/linear accelerator system *International Journal of Radiation Oncology Biology Physics* **59** 960-70

Baro J, Sempau J, Fernandezvarea J M and Salvat F 1995 PENELOPE - an algorithm for monte-carlo simulation of the penetration and energy-loss of electrons and positrons in matter *Nuclear Instruments & Methods in Physics Research Section B-Beam Interactions with Materials and Atoms* **100** 31-46

Barzilai J and Borwein J M 1988 Two-point step size gradient methods *IMA Journal of Numerical Analysis* **8** 141-8

Bazaraa M S, Sherali H D and Shetty C M 2006 Nonlinear Programming: Theory and Algorithms. (Hoboken: A John Wiley & Sons)

Beadle B M, Jhingran A, Salehpour M, Sam M, Iyer R B and Eifel P I 2009 Cervix regression and motion during the course of external beam chemoradiation for cervical cancer *International Journal of Radiation Oncology Biology Physics* **73** 235-41

Bedford J L 2009 Treatment planning for volumetric modulated arc therapy *Med Phys* **36** 5128-38

Bedford J L, Nordmark Hansen V, McNair H A, Aitken A H, Brock J E, Warrington A P and Brada M 2008 Treatment of lung cancer using volumetric modulated arc therapy and image guidance: a case study *Acta Oncol* **47** 1438-43

Berger M J 1963 Monte carlo calculation of the penetration and diffusion of fast charged particles *Methods in Computational Physics*, Volume 1, 135-215

Bielajew A F, Hirayama H, Nelson W R and Rogers D W O 1994 History, overview and recent improvements of EGS4 National Research Council of Canada Report PIRS-0436

Boyer A L and Li S D 1997 Geometric analysis of light-field position of a multileaf collimator with curved ends *Medical Physics* **24** 757-62

Briesmeister J F 1993 MCNP-a general Monte Carlo N-particle transport code Los Alamos National Laboratory Report LA-12625-M

Brock K K, Sharpe M B, Dawson L A, Kim S M and Jaffray D A 2005 Accuracy of finite element model-based multi-organ deformable image registration *Medical Physics* **32** 1647-59

Buffa F M and Nahum A E 2000 Monte Carlo dose calculations and radiobiological modelling: analysis of the effect of the statistical noise of the dose distribution on the probability of tumour control *Physics in Medicine and Biology* **45** 3009-23

Burridge N, Amer A, Marchant T, Sykes J, Stratford J, Henry A, McBain C, Price P and Moore C 2006 Online adaptive radiotherapy of the bladder: Small bowel irradiated-volume reduction *International Journal of Radiation Oncology Biology Physics* **66** 892-7

Calvo O I, Gutierrez A N, Stathakis S, Esquivel C and Papanikolaou N 2012 On the quantification of the dosimetric accuracy of collapsed cone convolution superposition (CCCS) algorithm for small lung volumes using IMRT *Journal of Applied Clinical Medical Physics* **13** 43-59

Castadot P, Lee J A, Parraga A, Geets X, Macq B and Gregoire V 2008 Comparison of 12 deformable registration strategies in adaptive radiation therapy for the treatment of head and neck tumors *Radiotherapy and Oncology* **89** 1-12

Chen M, Lu W, Chen Q, Ruchala K and Olivera G 2009 Efficient gamma index calculation using fast Euclidean distance transform *Physics in Medicine and Biology* **54** 2037-47

Cheng A, Harms W B, Gerber R L, Wong J W and Purdy J A 1996 Systematic verification of a three-dimensional electron beam dose calculation algorithm *Medical Physics* **23** 685-93

Connell P P and Hellman S 2009 Advances in Radiotherapy and Implications for the Next Century: A Historical Perspective *Cancer Research* **69** 383-92

Davidson S, Cui J, Followill D, Ibbott G and Deasy J 2008 A flexible Monte Carlo tool for patient or phantom specific calculations: comparison with preliminary validation measurements *Journal of Physics: Conference Series* **102** (6pp.)

de la Zerda A, Armbruster B and Xing L 2007 Formulating adaptive radiation therapy (ART) treatment planning into a closed-loop control framework *Physics in Medicine and Biology* **52** 4137-53

Deasy J O 2000 Denoising of electron beam Monte Carlo dose distributions using digital filtering techniques *Physics in Medicine and Biology* **45** 1765-79

Deasy J O, Wickerhauser M V and Picard M 2002 Accelerating Monte Carlo simulations of radiation therapy dose distributions using wavelet threshold de-noising *Medical Physics* **29** 2366-73

Deng J, Jiang S B, Kapur A, Li J S, Pawlicki T and Ma C M 2000 Photon beam characterization and modelling for Monte Carlo treatment planning *Physics in Medicine and Biology* **45** 411-27

Deng J, Ma C M, Hai J and Nath R 2003 Commissioning 6 MV photon beams of a stereotactic radiosurgery system for Monte Carlo treatment planning *Medical Physics* **30** 3124-34

Depuydt T, Van Esch A and Huyskens D P 2002 A quantitative evaluation of IMRT dose distributions: refinement and clinical assessment of the gamma evaluation *Radiotherapy and Oncology* **62** 309-19

El Naqa I, Deasy J O and Vicic M 2003 Locally adaptive denoising of Monte Carlo dose distributions via hybrid median filtering *Proc. IEEE Medical Imaging Conf. (19–25 October, Portland, OR)*

Feygelman V, Forster K, Opp D and Nilsson G 2009 Evaluation of a biplanar diode array dosimeter for quality assurance of step-and-shoot IMRT *Journal of Applied Clinical Medical Physics* **10** 64-78

Fippel M, Haryanto F, Dohm O, Nusslin F and Kriesen S 2003 A virtual photon energy fluence model for Monte Carlo dose calculation *Medical Physics* **30** 301-11

Fippel M and Nusslin F 2003 Smoothing Monte Carlo calculated dose distributions by iterative reduction of noise *Physics in Medicine and Biology* **48** 1289-304

Fix M K, Keall P J, Dawson K and Siebers J V 2004 Monte Carlo source model for photon beam radiotherapy: photon source characteristics *Medical Physics* **31** 3106-21

Foroudi F, Wong J, Haworth A, Baille A, McAlpine J, Rolfo A, Kron T, Roxby P, Paneghel A, Williams S, Duchesne G and Tai K H 2009 Offline adaptive radiotherapy for bladder cancer using cone beam computed tomography *Journal of Medical Imaging and Radiation Oncology* **53** 226-33

Foskey M, Davis B, Goyal L, Chang S, Chaney E, Strehl N, Tomei S, Rosenman J and Joshi S 2005 Large deformation three-dimensional image registration in image-guided radiation therapy *Physics in Medicine and Biology* **50** 5869-92

Fu W, Yang Y, Yue N J, Heron D E and Huq M S 2009 A cone beam CT-guided online plan modification technique to correct interfractional anatomic changes for prostate cancer IMRT treatment *Physics in Medicine and Biology* **54** 1691-703

Gardner J K, Siebers J V and Kawrakow I 2007 Dose calculation validation of VMC++ for photon beams *Medical Physics* **34** 1809-18

Gu X, Jelen U, Li J, Jia X and Jiang S B 2011a A GPU-based finite-size pencil beam algorithm with 3D-density correction for radiotherapy dose calculation *Physics in Medicine and Biology* **56** 3337-50

Gu X, Jia X and Jiang S B 2011b GPU-based fast gamma index calculation *Physics in Medicine and Biology* **56** 1431-41

Gu X, Pan H, Liang Y, Castillo R, Yang D, Choi D, Castillo E, Majumdar A, Guerrero T and Jiang S B 2010 Implementation and evaluation of various demons deformable image registration algorithms on a GPU *Physics in Medicine and Biology* **55** 207-19

Hall E J and Giaccia A J 2006 Radiobiology for the radiologist (Philadelphia: Lippincott Williams & Wilkins)

Hardcastle N, Tome W A, Cannon D M, Brouwer C L, Wittendorp P W H, Dogan N, Guckenberger M, Allaire S, Mallya Y, Kumar P, Oechsner M, Richter A, Song S, Myers M, Polat B and Bzdusek K 2012 A multi-institution evaluation of deformable image registration algorithms for automatic organ delineation in adaptive head and neck radiotherapy *Radiation Oncology* **7**

Harms W B, Low D A, Wong J W and Purdy J A 1998 A software toes for the quantitative evaluation of 3D dose calculation algorithms *Medical Physics* **25** 1830-6

Hestenes M R 1969 Multiplier and gradient methods *Journal of optimization theory and applications* **4** 303-20

Hirayama H, Namito Y, Bielajew A F, Wilderman S J and Nelson W R 2010 The EGS5 code system Stanford Linear Accelerator Center Report SLAC-R-730

Hissoiny S, Ozell B, Bouchard H and Despres P 2011 GPUMCD: A new GPU-oriented Monte Carlo dose calculation platform *Medical Physics* **38** 754-64

Holden M 2008 A review of geometric transformations for nonrigid body registration *Ieee Transactions on Medical Imaging* **27** 111-28

Islam K T S, Dempsey J F, Ranade M K, Maryanski M J and Low D A 2003 Initial evaluation of commercial optical CT-based 3D gel dosimeter *Medical Physics* **30** 2159-68

Jacques R, Taylor R, Wong J and McNutt T 2010 Towards real-time radiation therapy: GPU accelerated superposition/convolution *Computer Methods and Programs in Biomedicine* **98** 285-92

Jia X, Gu X, Graves Y J, Folkerts M and Jiang S B 2011a GPU-based fast Monte Carlo simulation for radiotherapy dose calculation *Physics in Medicine and Biology* **56** 7017-31

Jia X, Gu X, Sempau J, Choi D, Majumdar A and Jiang S B 2010 Development of a GPU-based Monte Carlo dose calculation code for coupled electron-photon transport *Physics in Medicine and Biology* **55** 3077-86

Jia X, Lou Y, Lewis J, Li R, Gu X, Men C, Song W Y and Jiang S B 2011b GPU-based fast low-dose cone beam CT reconstruction via total variation *Journal of X-Ray Science and Technology* **19** 139-54

Jiang S B, Boyer A L and Ma C M C 2001 Modeling the extrafocal radiation and monitor chamber backscatter for photon beam dose calculation *Medical Physics* **28** 55-66

Jiang S B, Kapur A and Ma C M 2000 Electron beam modeling and commissioning for Monte Carlo treatment planning *Medical Physics* **27** 180-91

Jiang S B, Sharp G C, Neicu T, Berbeco R I, Flampouri S and Bortfeld T 2006 On dose distribution comparison *Physics in Medicine and Biology* **51** 759-76

Ju T, Simpson T, Deasy J O and Low D A 2008 Geometric interpretation of the gamma dose distribution comparison technique: Interpolation-free calculation *Medical Physics* **35** 879-87

Kak A C, Slaney M and IEEE Engineering in Medicine and Biology Society. 1988 Principles of computerized tomographic imaging (New York: IEEE Press)

Kashani R, Hub M, Kessler M L and Balter J M 2007 Technical note: A physical phantom for assessment of accuracy of deformable alignment algorithms *Medical Physics* **34** 2785-8

Kaus M R, Brock K K, Pekar V, Dawson L A, Nichol A M and Jaffray D A 2007 Assessment of a model-based deformable image registration approach for radiation therapy planning *International Journal of Radiation Oncology Biology Physics* **68** 572-80

Kawrakow I 2000 Accurate condensed history Monte Carlo simulation of electron transport. I. EGSnrc, the new EGS4 version *Medical Physics* **27** 485-98

Kawrakow I 2002 On the de-noising of Monte Carlo calculated dose distributions *Physics in Medicine and Biology* **47** 3087-103

Kawrakow I 2005 On the efficiency of photon beam treatment head simulations *Medical Physics* **32** 2320-6

Kawrakow I and Bielajew A F 1998 On the condensed history technique for electron transport *Nuclear Instruments & Methods in Physics Research Section B-Beam Interactions with Materials and Atoms* **142** 253-80

Kawrakow I, Fippel M and Friedrich K 1996 3D electron dose calculation using a Voxel based Monte Carlo algorithm (VMC) *Medical Physics* **23** 445-57

Kawrakow I, Rogers D W O and Walters B R B 2004 Large efficiency improvements in BEAMnrc using directional bremsstrahlung splitting *Medical Physics* **31** 2883-98

Keall P J, Siebers J V, Jeraj R and Mohan R 2000 The effect of dose calculation uncertainty on the evaluation of radiotherapy plans *Medical Physics* **27** 478-84

Kirby N, Chuang C and Pouliot J 2011 A two-dimensional deformable phantom for quantitatively verifying deformation algorithms *Medical Physics* **38** 4583-6

Kirby N, Chuang C, Ueda U and Pouliot J 2013 The need for application-based adaptation of deformable image registration *Medical Physics* **40,** 011702 (10pp.)

Korreman S, Medin J and Kjaer-Kristoffersen F 2009 Dosimetric verification of RapidArc treatment delivery *Acta Oncologica* **48** 185-91

Larsen E W 1992 A theoretical derivation of the condensed history algorithm *Annals of Nuclear Energy* **19** 701-14

Le T, Chartrand R and Asaki T J 2007 A variational approach to reconstructing images corrupted by poisson noise *Journal of Mathematical Imaging and Vision* **27** 257-63

Lee C, Langen K M, Lu W, Haimerl J, Schnarr E, Ruchala K J, Olivera G H, Meeks S L, Kupelian P A, Shettenberger T D and Manon R R 2008 Evaluation of geometric changes of parotid glands during head and neck cancer radiotherapy using daily MVCT and automatic deformable registration *Radiotherapy and Oncology* **89** 81-8

Lee C M, Shrieve D C and Gaffney D K 2004 Rapid involution and mobility of carcinoma of the cervix *International Journal of Radiation Oncology Biology Physics* **58** 625-30

Letourneau D, Publicover J, Kozelka J, Moseley D J and Jaffray D A 2009 Novel dosimetric phantom for quality assurance of volumetric modulated arc therapy *Medical Physics* **36** 1813-21

Li J G, Dempsey J F, Ding L, Liu C R and Palta J R 2003 Validation of dynamic MLC-controller log files using a two-dimensional diode array *Medical Physics* **30** 799-805

Li J G, Yan G and Liu C 2009 Comparison of two commercial detector arrays for IMRT quality assurance *Journal of Applied Clinical Medical Physics* **10** 62-74

Low D A 2010 Gamma dose Distribution Evaluation Tool *Journal of Physics: Conference Series* **250** 012071 (11 pp.)

Low D A and Dempsey J F 2003 Evaluation of the gamma dose distribution comparison method *Medical Physics* **30** 2455-64

Low D A, Harms W B, Mutic S and Purdy J A 1998 A technique for the quantitative evaluation of dose distributions *Medical Physics* **25** 656-61

Lu W, Chen M, Chen Q, Ruchala K and Olivera G 2008 Adaptive fractionation therapy: I. Basic concept and strategy *Physics in Medicine and Biology* **53** 5495-511

Lu W G, Chen M L, Olivera G H, Ruchala K J and Mackie T R 2004 Fast free-form deformable registration via calculus of variations *Physics in Medicine and Biology* **49** 3067-87

Lu W G, Olivera G H, Chen Q, Ruchala K J, Haimerl J, Meeks S L, Langen K M and Kupelian P A 2006 Deformable registration of the planning image (kVCT) and the daily images (MVCT) for adaptive radiation therapy *Physics in Medicine and Biology* **51** 4357-74

Luo W, Li J, Price R A, Jr., Chen L, Yang J, Fan J, Chen Z, McNeeley S, Xu X and Ma C-M 2006 Monte Carlo based IMRT dose verification using MLC log files and R/V outputs *Medical Physics* **33** 2557-64

Ma C M 1998 Characterization of computer simulated radiotherapy beams for Monte-Carlo treatment planning *Radiation Physics and Chemistry* **53** 329-44

Ma C M, Faddegon B A, Rogers D W O and Mackie T R 1997 Accurate characterization of Monte Carlo calculated electron beams for radiotherapy *Medical Physics* **24** 401-16

Ma C M, Li J S, Pawlicki T, Jiang S B, Deng J, Lee M C, Koumrian T, Luxton M and Brain S 2002 A Monte Carlo dose calculation tool for radiotherapy treatment planning *Physics in Medicine and Biology* **47** 1671-89

Ma C M, Mok E, Kapur A, Pawlicki T, Findley D, Brain S, Forster K and Boyer A L 1999 Clinical implementation of a Monte Carlo treatment planning system *Medical Physics* **26** 2133-43

McDermott L N, Wendling M, Nijkamp J, Mans A, Sonke J-J, Mijnheer B J and van Herk M 2008 3D in vivo dose verification of entire hypo-fractionated IMRT treatments using an EPID and cone-beam CT *Radiotherapy and Oncology* **86** 35-42

Men C, Gu X, Choi D, Majumdar A, Zheng Z, Mueller K and Jiang S B 2009 GPU-based ultrafast IMRT plan optimization *Physics in Medicine and Biology* **54** 6565-73

Men C, Jia X and Jiang S B 2010 GPU-based ultra-fast direct aperture optimization for online adaptive radiation therapy *Physics in Medicine and Biology* **55** 4309-19

Miao B H, Jeraj R, Bao S L and Mackie T R 2003 Adaptive anisotropic diffusion filtering of Monte Carlo dose distributions *Physics in Medicine and Biology* **48** 2767-81

Mohan R, Zhang X D, Wang H, Kang Y X, Wang X C, Liu H, Ang K, Kuban D and Dong L 2005 Use of deformed intensity distributions for on-line modification of image-guided IMRT to account for interfractional anatomic changes *International Journal of Radiation Oncology Biology Physics* **61** 1258-66

Nelson W R, Hirayama H and Rogers D W O 1985 The EGS4 code system Stanford Linear Accelerator Center Report SLAC-265

Nicolini G, Vanetti E, Clivio A, Fogliata A, Korreman S, Bocanek J and Cozzi L 2008 The GLAaS algorithm for portal dosimetry and quality assurance of RapidArc, an intensity modulated rotational therapy *Radiation Oncology* **3** 24

NVIDIA 2013 NVIDIA CUDA C Programming Guide v.5.5.

Otto K 2008 Volumetric modulated arc therapy: IMRT in a single gantry arc *Medical Physics* **35** 310-7

Popescu C C, Olivotto I A, Beckham W A, Ansbacher W, Zavgorodni S, Shaffer R, Wai E S and Otto K 2009 Volumetric Modulated Arc Therapy Improves Dosimetry and Reduces Treatment Time Compared To Conventional Intensity-Modulated Radiotherapy for Locoregional Radiotherapy of Left-Sided Breast Cancer and Internal Mammary Nodes *Int J Radiat Oncol Biol Phys* **76** 287-295

Powell M J D 1969 A method for non-linear constraints in minimization problems In Optimization (Academic Press)

Richardson S L, Tome W A, Orton N P, McNutt T R and Paliwal B R 2003 IMRT delivery verification using a spiral phantom *Medical Physics* **30** 2553-8

Salvat F, Fernandez-Varea J M and Sempau J 2009 PENELOPE-2008: A Code System for Monte Carlo Simulation of Electron and Photon Transport. (Issy-les-Moulineaux: OECD-NEA

Samant S S, Xia J, Muyan-Oezcelilk P and Owens J D 2008 High performance computing for deformable image registration: Towards a new paradigm in adaptive radiotherapy *Medical Physics* **35** 3546-53

Schreibmann E, Dhabaan A, Elder E and Fox T 2009 Patient-specific quality assurance method for VMAT treatment delivery *Medical Physics* **36** 4530-5

Schulze D, Liang J, Yana D and Zhang T 2009 Comparison of various online IGRT strategies: The benefits of online treatment plan re-optimization *Radiotherapy and Oncology* **90** 367-76

Sempau J, Acosta E, Baro J, FernandezVarea J M and Salvat F 1997 An algorithm for Monte Carlo simulation of coupled electron-photon transport

Nuclear Instruments & Methods in Physics Research Section B-Beam Interactions with Materials and Atoms **132** 377-90

Sempau J and Bielajew A F 2000 Towards the elimination of Monte Carlo statistical fluctuation from dose volume histograms for radiotherapy treatment planning *Physics in Medicine and Biology* **45** 131-57

Sempau J, Wilderman S J and Bielajew A F 2000 DPM, a fast, accurate Monte Carlo code optimized for photon and electron radiotherapy treatment planning dose calculations *Physics in Medicine and Biology* **45** 2263-91

Serban M, Heath E, Stroian G, Collins D L and Seuntjens J 2008 A deformable phantom for 4D radiotherapy verification: Design and image registration evaluation *Medical Physics* **35** 1094-102

Sharp G C, Kandasamy N, Singh H and Folkert M 2007 GPU-based streaming architectures for fast cone-beam CT image reconstruction and demons deformable registration *Physics in Medicine and Biology* **52** 5771-83

Shiu A S, Tung S, Hogstrom K R, Wong J W, Gerber R L, Harms W B, Purdy J A, Haken R K T, McShan D L and Fraass B A 1992 Verification data for electron-beam dose algorithms *Medical Physics* **19** 623-36

Siebers J V, Keall P J, Libby B and Mohan R 1999 Comparison of EGS4 and MCNP4b Monte Carlo codes for generation of photon phase space distributions for a Varian 2100C *Physics in Medicine and Biology* **44** 3009-26

Stock M, Kroupa B and Georg D 2005 Interpretation and evaluation of the gamma index and the gamma index angle for the verification of IMRT hybrid plans *Physics in Medicine and Biology* **50** 399-411

Teke T, Bergman A M, Kwa W, Gill B, Duzenli C and Popescu I A 2010 Monte Carlo based, patient-specific RapidArc QA using LINAC log files *Medical Physics* **37** 116-23

Thirion J 1998 Image matching as a diffusion process: an analogy with Maxwell's demons *Medical Image Analysis* **2** 243–60

Townson R W, Jia X, Tian Z, Graves Y J, Zavgorodni S and Jiang S B 2013 GPU-based Monte Carlo radiotherapy dose calculation using phase-space sources *Physics in Medicine and Biology* **58** 4341-56

Tyagi N, Bose A and Chetty I J 2004 Implementation of the DPM Monte Carlo code on a parallel architecture for treatment planning applications *Medical Physics* **31** 2721-5

Tyagi N, Lewis J H, Yashar C M, Vo D, Jiang S B, Mundt A J and Mell L K 2011 Daily online cone beam computed tomography to assess interfractional motion in patients with intact cervical cancer *International Journal of Radiation Oncology Biology Physics* **80** 273-80

van de Bunt L, van der Heide U A, Ketelaars M, de Kort G A P and Jurgenliemk-Schulz I M 2006 Conventional, conformal, and intensity-modulated radiation therapy treatment planning of external beam radiotherapy for cervical cancer: The impact of tumor regression *International Journal of Radiation Oncology Biology Physics* **64** 189-96

van Elmpt W J C, Nijsten S M J J G, Dekker A L A J, Mijnheer B J and Lambin P 2007 Treatment verification in the presence of inhomogeneities using EPID-based three-dimensional dose reconstruction *Medical Physics* **34** 2816-26

van Etmpt W, Nijsten S, Mijnheer B, Dekker A and Lambin P 2008 The next step in patient-specific QA: 3D dose verification of conformal and intensity-modulated RT based on EPID dosimetry and Monte Carlo dose calculations *Radiotherapy and Oncology* **86** 86-92

Vandyk J, Barnett R B, Cygler J E and Shragge P C 1993 Commissioning and quality assurance of treatment planning computers *International Journal of Radiation Oncology Biology Physics* **26** 261-73

Varian Medical System 2010 TrueBeam Trajectory Log File Specification.

Verhaegen F and Seuntjens J 2003 Monte Carlo modelling of external radiotherapy photon beams *Physics in Medicine and Biology* **48** R107-R64

von Wittenau A E S, Cox L J, Bergstrom P M, Chandler W P, Siantar C L H and Mohan R 1999 Correlated histogram representation of Monte Carlo derived medical accelerator photon-output phase space *Medical Physics* **26** 1196-211

Walters B, Kawrakow I and Rogers D W O NRCC Report PIRS-794revB, (NRC Canada, 2005)

Wang H, Dong L, O'Daniel J, Mohan R, Garden A S, Ang K K, Kuban D A, Bonnen M, Chang J Y and Cheung R 2005 Validation of an accelerated 'demons' algorithm for deformable image registration in radiation therapy *Physics in Medicine and Biology* **50** 2887-905

Wendling M, Zijp L J, McDermott L N, Smit E J, Sonke J-J, Mijnheer B J and van Herk M 2007 A fast algorithm for gamma evaluation in 3D *Medical Physics* **34** 1647-54

Wu C, Jeraj R, Olivera G H and Mackie T R 2002 Re-optimization in adaptive radiotherapy *Physics in Medicine and Biology* **47** 3181-95

Wu Q J, Thongphiew D, Wang Z, Mathayomchan B, Chankong V, Yoo S, Lee W R and Yin F-F 2008 On-line re-optimization of prostate IMRT plans for adaptive radiation therapy *Physics in Medicine and Biology* **53** 673-91

Xu F and Mueller K 2005 Accelerating popular tomographic reconstruction algorithms on commodity PC graphics hardware *LEEE Transactions on Nuclear Science* **52** 654-63

Yan D 2008 Developing quality assurance processes for image-guided adaptive radiation therapy *International Journal of Radiation Oncology Biology Physics* **71** S28-S32

Yan D, Lockman D, Martinez A, Wong J, Brabbins D, Vicini F, Liang J and Kestin L 2005 Computed tomography guided management of interfractional patient variation *Seminars in Radiation Oncology* **15** 168-79

Yan D, Vicini F, Wong J and Martinez A 1997 Adaptive radiation therapy *Physics in Medicine and Biology* **42** 123-32

Yan G, Tian J, Zhu S, Dai Y and Qin C 2008 Fast cone-beam CT image reconstruction using GPU hardware *Journal of X-Ray Science and Technology* **16** 225-34

Yang D, Li H, Low D A, Deasy J O and El Naqa I 2008 A fast inverse consistent deformable image registration method based on symmetric optical flow computation *Physics in Medicine and Biology* **53** 6143-65

Yang J, Li J, Chen L, Price R, McNeeley S, Qin L, Wang L, Xiong W and Ma C M 2005 Dosimetric verification of IMRT treatment planning using Monte Carlo simulations for prostate cancer *Physics in Medicine and Biology* **50** 869-78

Yong Y, Schreibmann E, Tianfang L, Chuang W and Lei X 2007 Evaluation of on-board kV cone beam CT (CBCT)-based dose calculation *Physics in Medicine and Biology* **52** 685-705

Yuan J and Chen W 2010 A gamma dose distribution evaluation technique using the k-d tree for nearest neighbor searching *Medical Physics* **37** 4868-73

Zeidan O A, Li J G, Ranade M, Stell A M and Dempsey J F 2004 Verification of step-and-shoot IMRT delivery using a fast video-based electronic portal imaging device *Medical Physics* **31** 463-76

Zelefsky M J, Fuks Z, Happersett L, Lee H J, Ling C C, Burman C M, Hunt M, Wolfe T, Venkatraman E, Jackson A, Skwarchuk M and Leibel S A 2000 Clinical experience with intensity modulated radiation therapy (IMRT) in prostate cancer *Radiotherapy and Oncology* **55** 241-9

Zhang T Z, Chi Y W, Meldolesi E and Yan D 2007 Automatic delineation of on-line head-and-neck computed tomography images: Toward on-line adaptive radiotherapy *International Journal of Radiation Oncology Biology Physics* **68** 522-30

Zhen X, Yan H, Gu X, Zhou L, Jia X and Jiang S 2012 CT to Cone-Beam CT Deformable Registration With Simultaneous Intensity Correction *Physics in Medicine and Biology* **57** 6807-26

Zitova B and Flusser J 2003 Image registration methods: a survey *Image and Vision Computing* **21** 977-1000

Zygmanski P, Kung J H, Jiang S B and Chin L 2003 Dependence of fluence errors in dynamic IMRT on leaf-positional errors varying with time and leaf number *Medical Physics* **30** 2736-49

Appendix

Appendix A. A Sample Quality Assurance Report Using the GPU based Monte Carlo Quality Assurance Tool

Name: Nobody
Gender: Unknown
Plan/Site: prostate
PatientID: xxxxxxxx
DOB: xx/xx/xxxx
Date: Wed Nov 27 11:42:50 2013
Physicist: michael

Plan Dose (PD) vs. Monte Carlo Calculated Secondary Dose (SD)

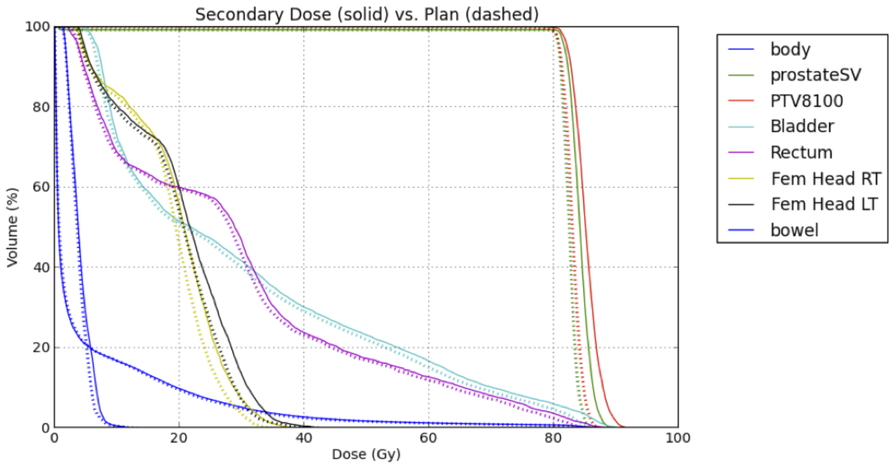

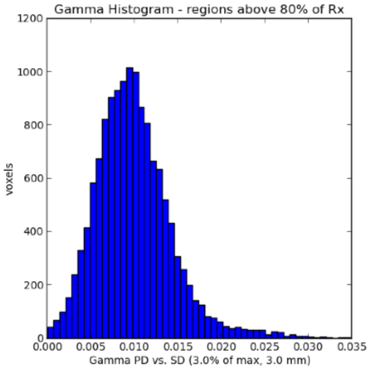

Volume Label	**Pass Rate (%)**
above 10% max dose	100.00
above 50% max dose	100.00

Volume Label	**Dose Criteria**	**PD**	**MC**
PTV8100	Max Dose < 107% Rx (86.7 Gy)	88.7 Gy	93.3 Gy
Bladder	V65 Gy < 20.0 %	11.6 %	13.0 %
Bladder	V40 Gy < 40.0 %	29.0 %	30.1 %
Rectum	Max Dose < 100% Rx (81.0 Gy)	86.7 Gy	90.3 Gy
Rectum	V65 Gy < 17.0 %	9.4 %	10.4 %
Rectum	V40 Gy < 35.0 %	23.1 %	23.7 %
Fem Head RT	Max Dose < 50 Gy	36.3 Gy	40.9 Gy
Fem Head LT	Max Dose < 50 Gy	42.5 Gy	45.2 Gy

Dosimetric Information (Gy)

Volume Label	**PD Max**	**PD Ave**	**PD Std**	**SD Max**	**SD Ave**	**SD Std**
body	88.68	5.58	12.36	93.30	5.67	12.75
prostateSV	87.72	81.90	7.15	92.37	83.63	7.38
PTV8100	88.68	83.01	1.41	93.30	85.22	2.01
Bladder	87.08	29.57	23.73	92.45	30.74	24.53
Rectum	86.72	28.42	21.93	90.32	29.26	22.56
Fem Head RT	36.26	18.19	7.33	40.86	19.49	7.94
Fem Head LT	42.48	19.15	8.40	45.23	20.42	8.96
bowel	13.63	3.78	1.60	13.89	4.07	1.82

Plan Dose (PD) vs. Monte Carlo Calculated Secondary Dose (SD)

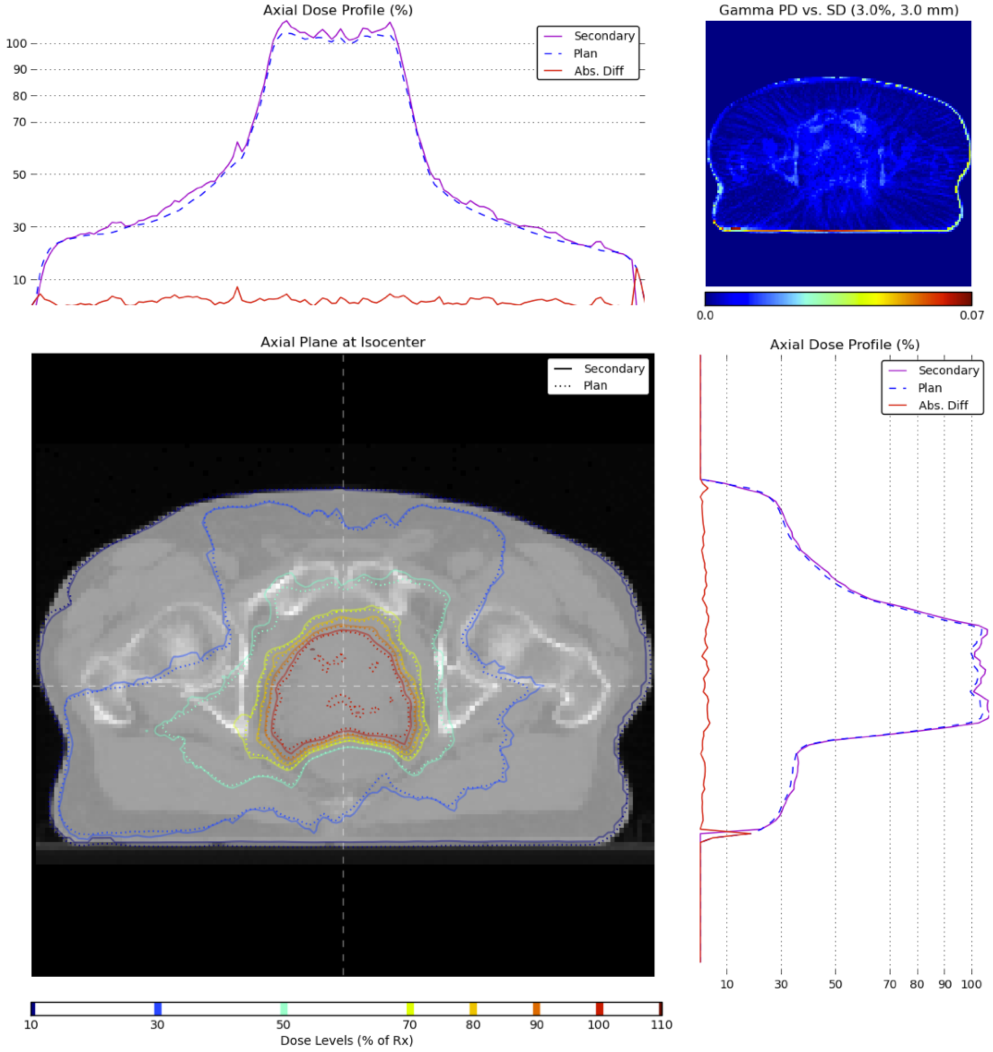

Plan Dose (PD) vs. Monte Carlo Calculated Secondary Dose (SD)

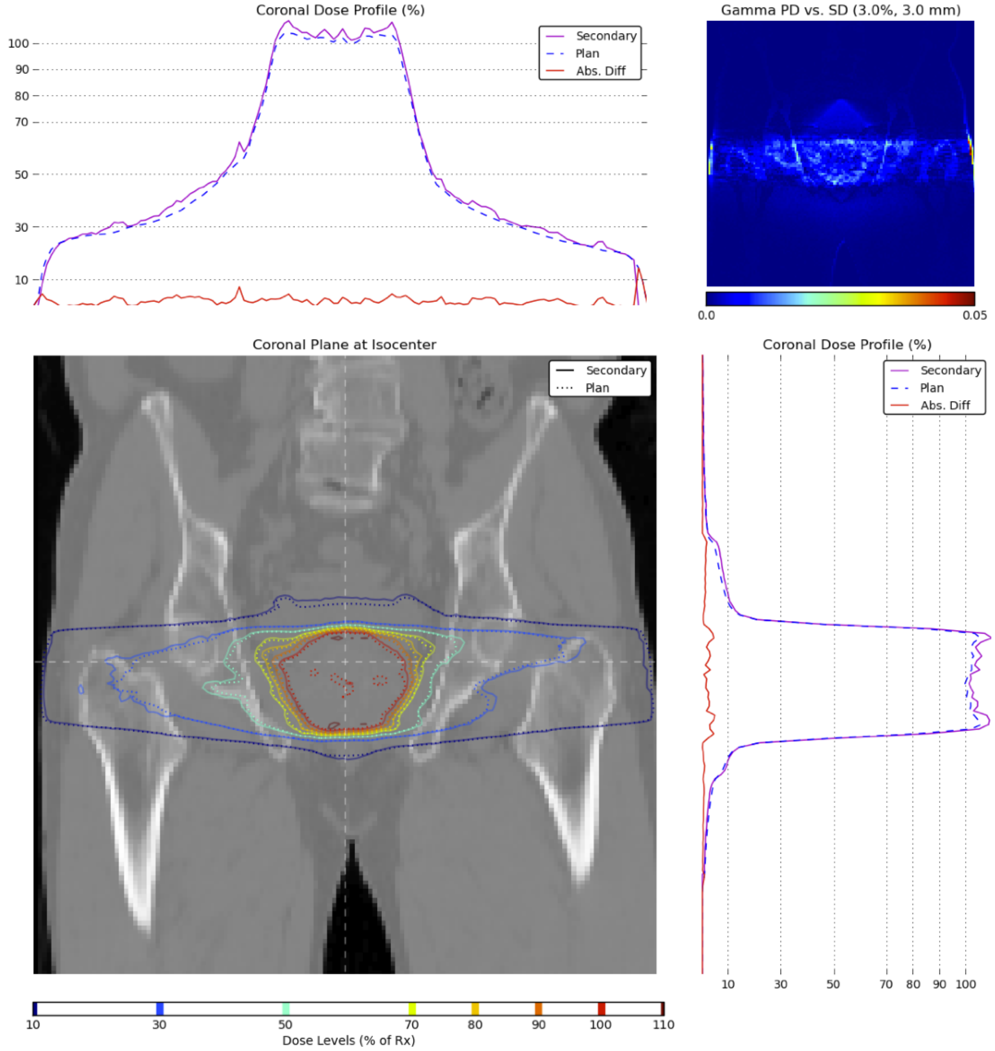

Plan Dose (PD) vs. Monte Carlo Calculated Secondary Dose (SD)

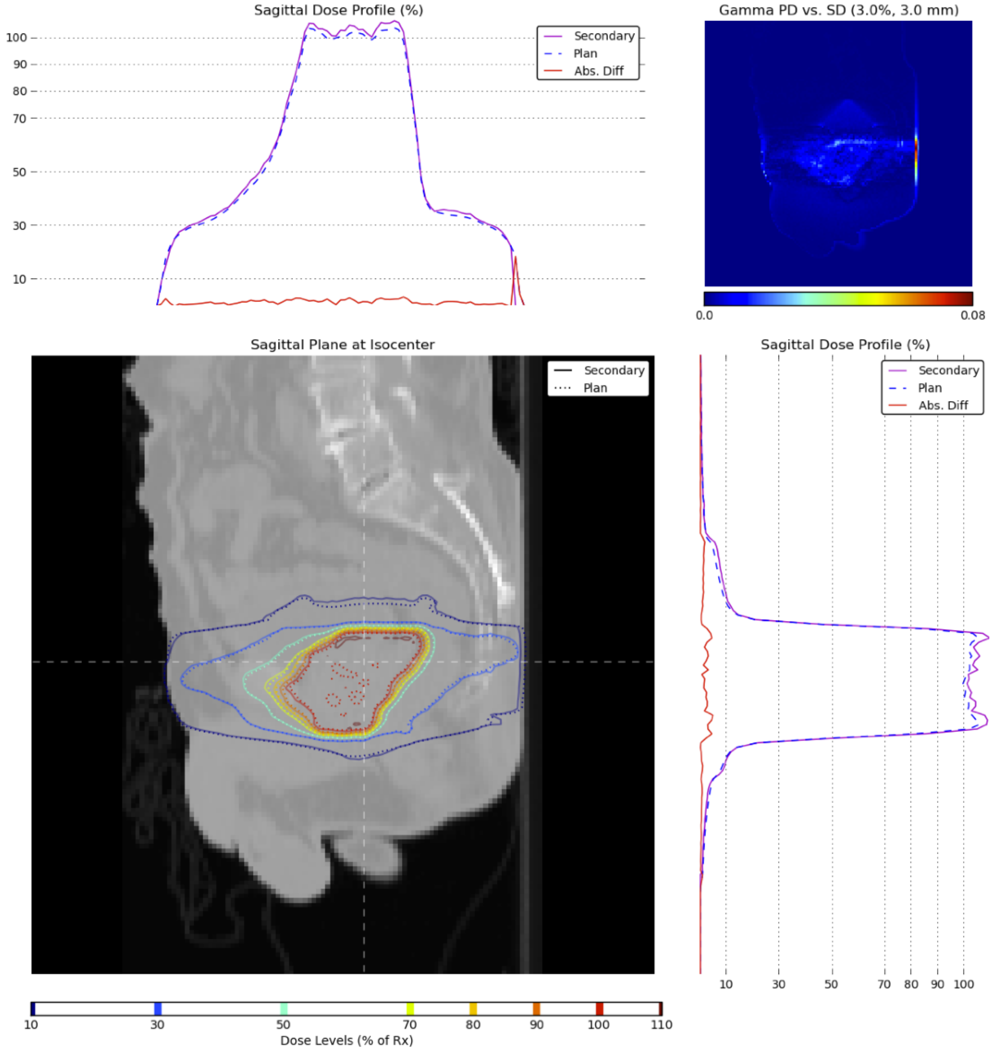

Plan Dose (PD) vs. Monte Carlo Calculated Delivered Dose (DD)

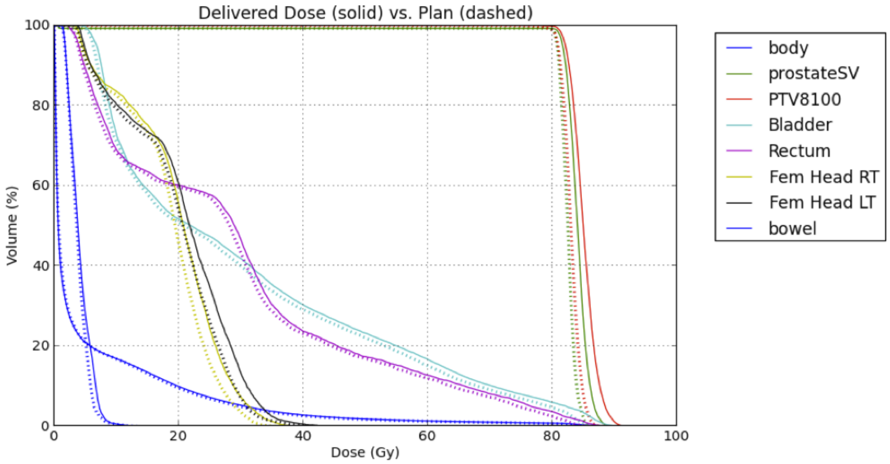

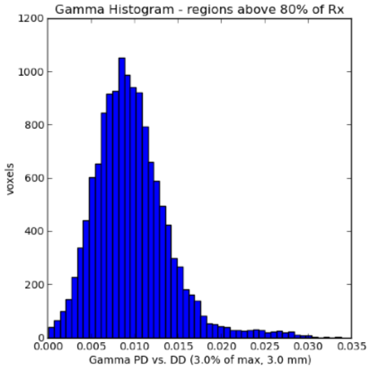

Volume Label	Pass Rate (%)
above 10% max dose	100.00
above 50% max dose	100.00

Volume Label	Dose Criteria	PD	MC
PTV8100	Max Dose < 107% Rx (86.7 Gy)	88.7 Gy	92.7 Gy
Bladder	V65 Gy < 20.0 %	11.6 %	12.9 %
Bladder	V40 Gy < 40.0 %	29.0 %	30.2 %
Rectum	Max Dose < 100% Rx (81.0 Gy)	86.7 Gy	90.0 Gy
Rectum	V65 Gy < 17.0 %	9.4 %	10.5 %
Rectum	V40 Gy < 35.0 %	23.1 %	23.6 %
Fem Head RT	Max Dose < 50 Gy	36.3 Gy	39.9 Gy
Fem Head LT	Max Dose < 50 Gy	42.5 Gy	45.1 Gy

Dosimetric Information (Gy)

Volume Label	PD Max	PD Ave	PD Std	DD Max	DD Ave	DD Std
body	88.68	5.58	12.36	92.66	5.70	12.77
prostateSV	87.72	81.90	7.15	91.67	83.48	7.36
PTV8100	88.68	83.01	1.41	92.66	85.08	1.94
Bladder	87.08	29.57	23.73	91.66	30.77	24.49
Rectum	86.72	28.42	21.93	90.05	29.33	22.51
Fem Head RT	36.26	18.19	7.33	39.91	19.53	7.94
Fem Head LT	42.48	19.15	8.40	45.06	20.47	8.96
bowel	13.63	3.78	1.60	13.95	4.07	1.83

Plan Dose (PD) vs. Monte Carlo Calculated Delivered Dose (DD)

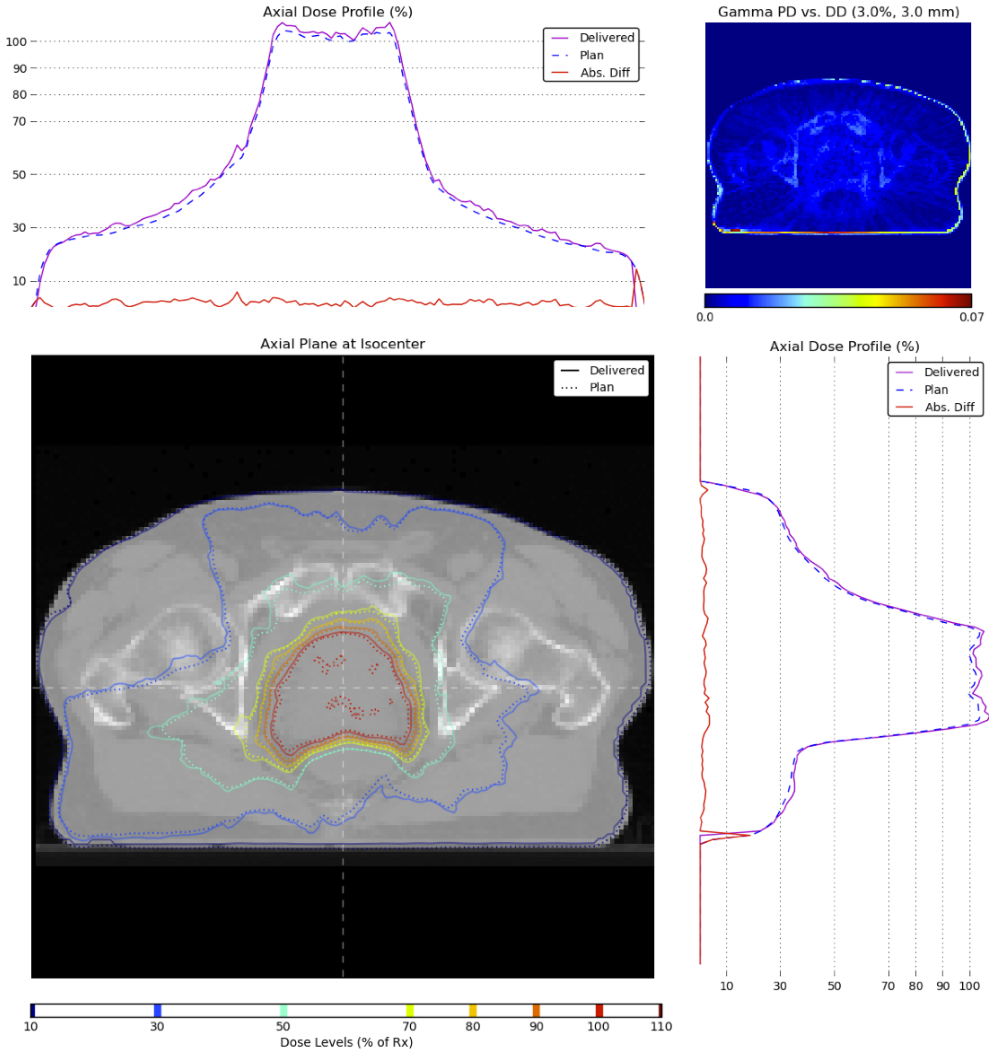

Plan Dose (PD) vs. Monte Carlo Calculated Delivered Dose (DD)

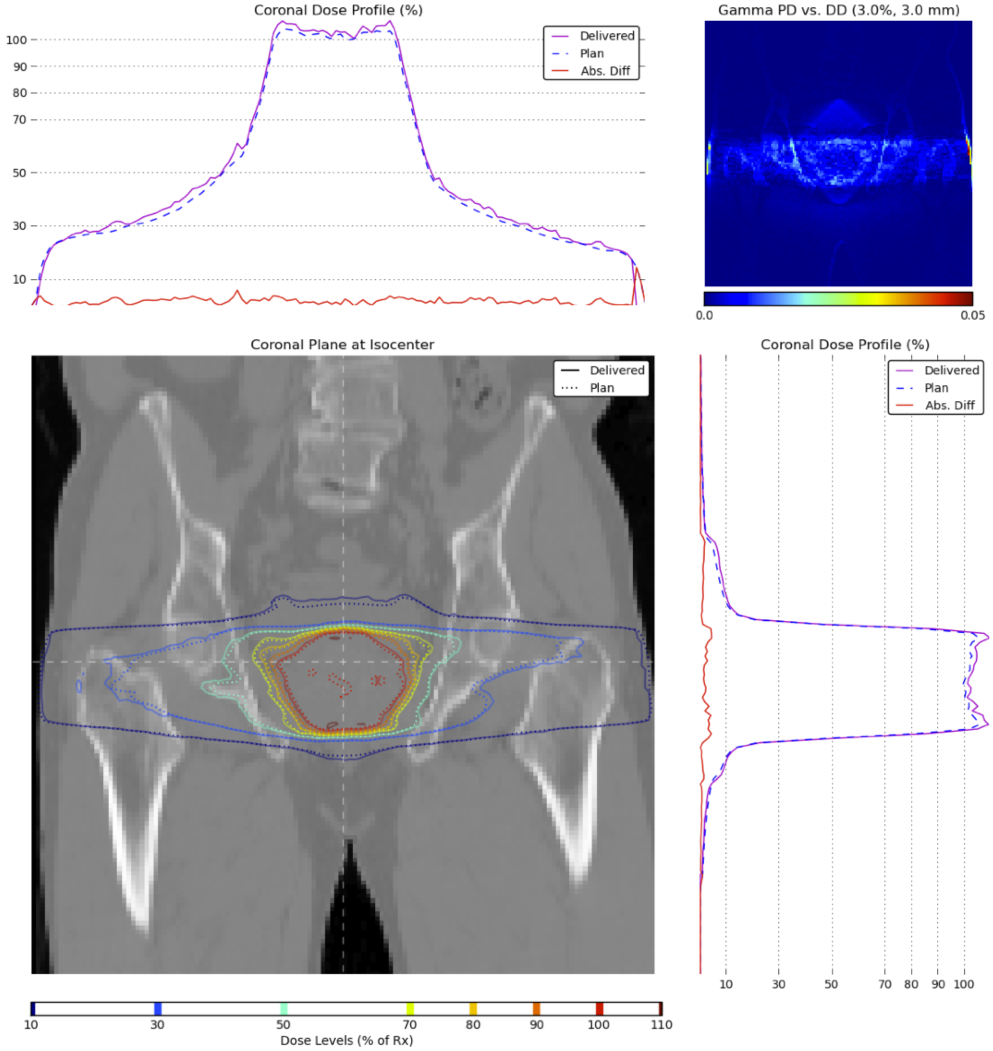

Plan Dose (PD) vs. Monte Carlo Calculated Delivered Dose (DD)

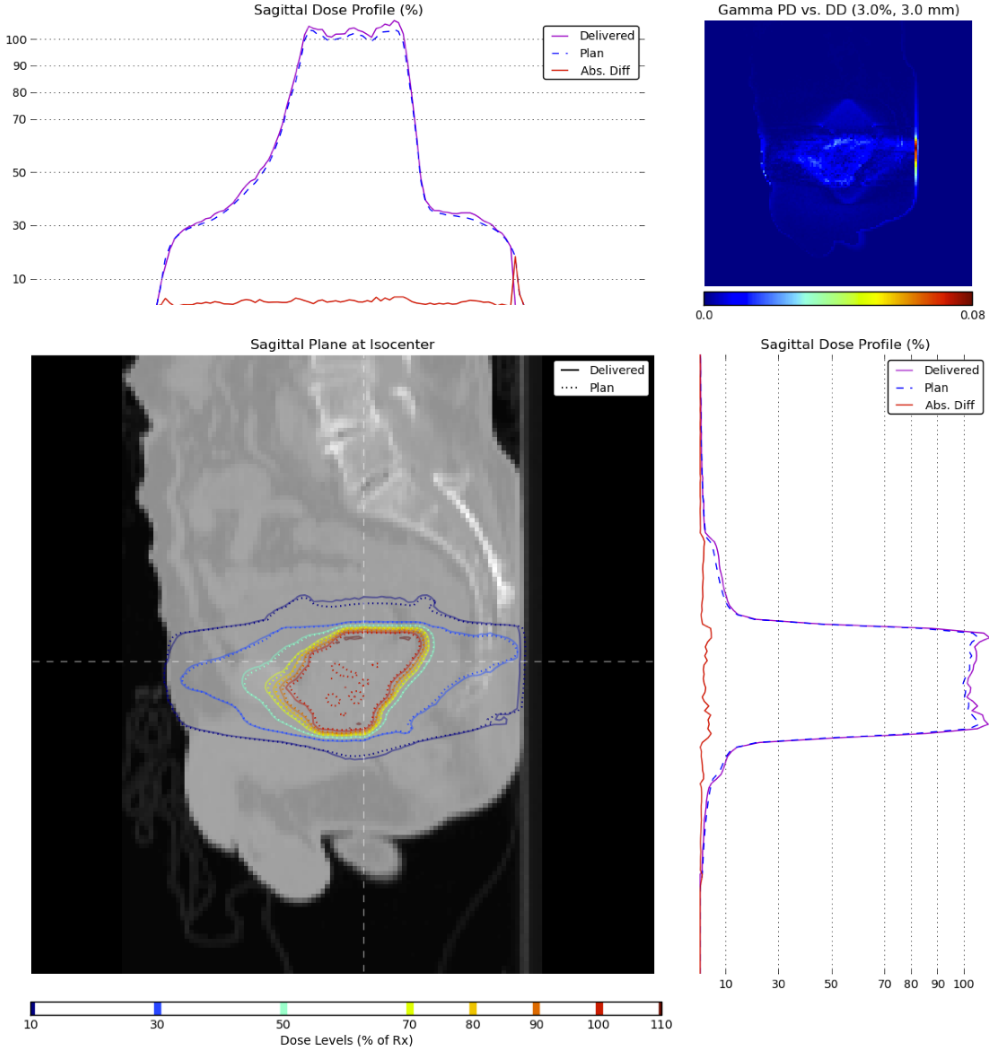

Secondary Dose (SD) vs. Delivered Dose (DD)

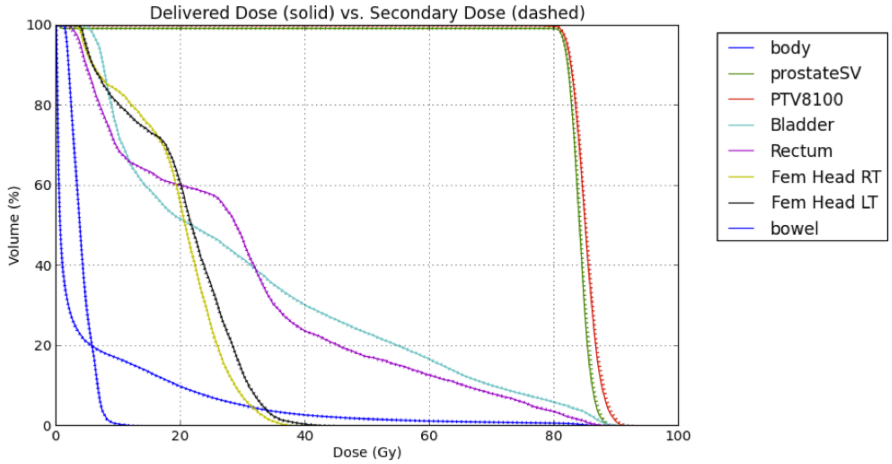

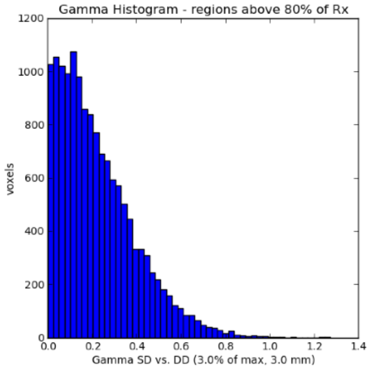

Volume Label	Dose Criteria	SD	MC
PTV8100	Max Dose < 107% Rx (86.7 Gy)	93.3 Gy	92.7 Gy
Bladder	V65 Gy < 20.0 %	13.0 %	12.9 %
Bladder	V40 Gy < 40.0 %	30.1 %	30.2 %
Rectum	Max Dose < 100% Rx (81.0 Gy)	90.3 Gy	90.0 Gy
Rectum	V65 Gy < 17.0 %	10.4 %	10.5 %
Rectum	V40 Gy < 35.0 %	23.7 %	23.6 %
Fem Head RT	Max Dose < 50 Gy	40.9 Gy	39.9 Gy
Fem Head LT	Max Dose < 50 Gy	45.2 Gy	45.1 Gy

Dosimetric Information (Gy)

Volume Label	SD Max	SD Ave	SD Std	DD Max	DD Ave	DD Std
body	93.30	5.67	12.75	92.66	5.70	12.77
prostateSV	92.37	83.63	7.38	91.67	83.48	7.36
PTV8100	93.30	85.22	2.01	92.66	85.08	1.94
Bladder	92.45	30.74	24.53	91.66	30.77	24.49
Rectum	90.32	29.26	22.56	90.05	29.33	22.51
Fem Head RT	40.86	19.49	7.94	39.91	19.53	7.94
Fem Head LT	45.23	20.42	8.96	45.06	20.47	8.96
bowel	13.89	4.07	1.82	13.95	4.07	1.83

Volume Label	Pass Rate (%)
above 10% max dose	100.00
above 50% max dose	100.00

Secondary Dose (SD) vs. Delivered Dose (DD)

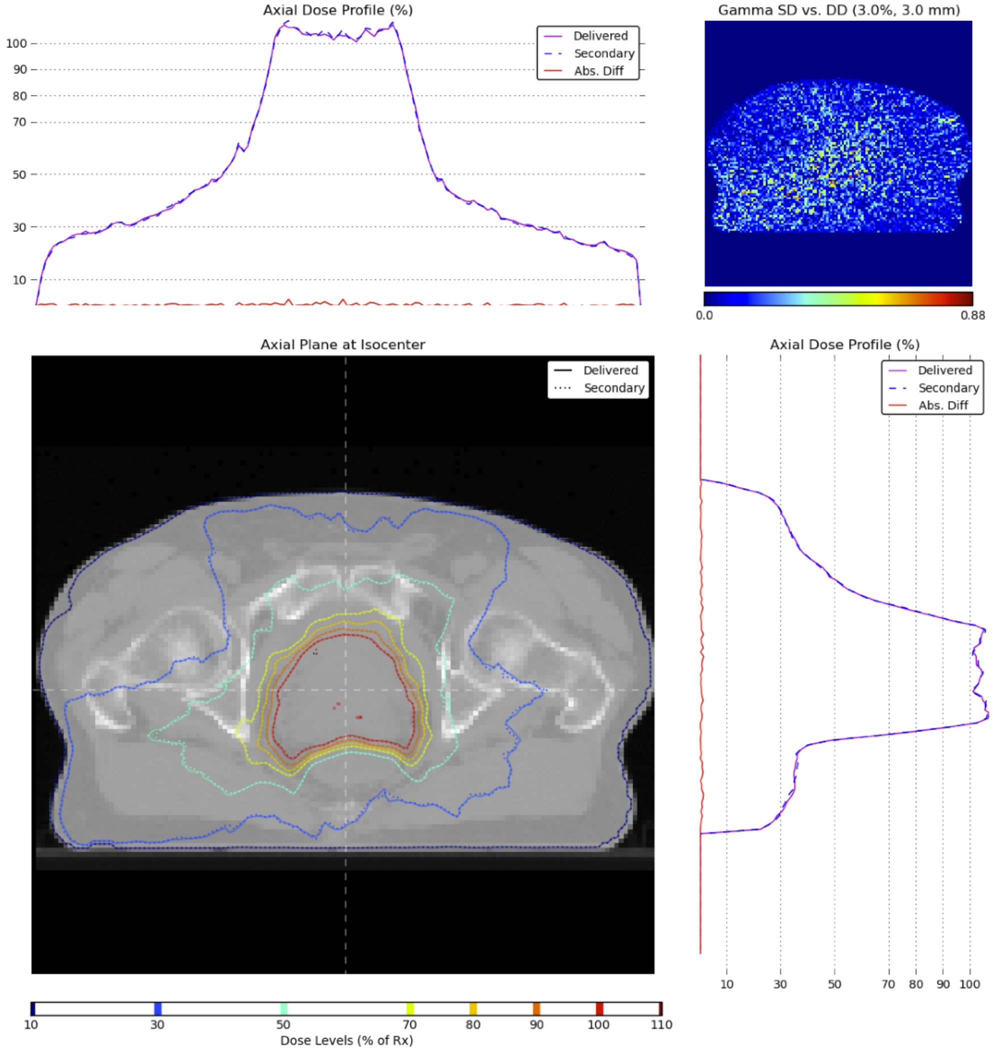

Secondary Dose (SD) vs. Delivered Dose (DD)

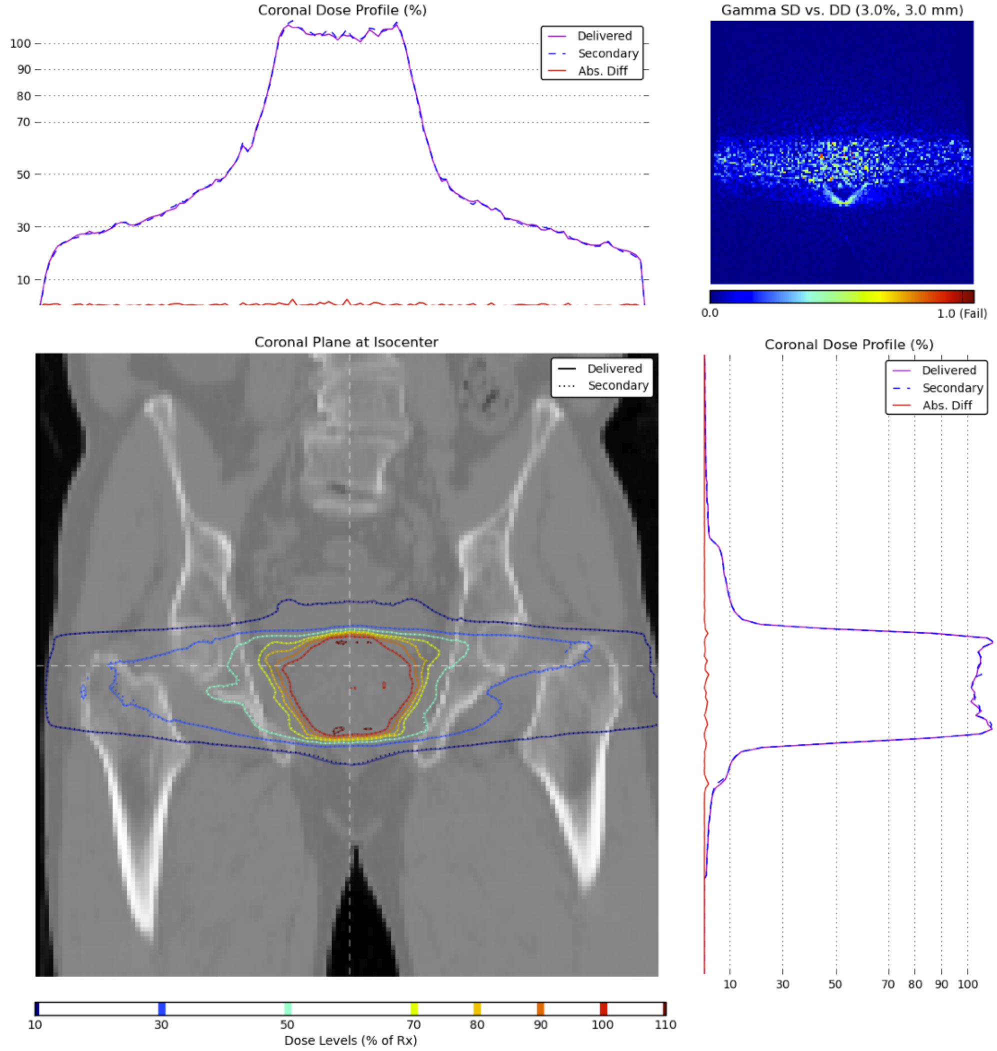

Secondary Dose (SD) vs. Delivered Dose (DD)